Gas Holdup in Bubble Column Reactors: Influence of Fermentation-Relevant compounds and Advances in X-ray Tomographic Measurements

A Study on the Impact of Alcohols and Acids on Gas Holdup and Beam Hardening Correction in XRT

Sam Jesse den Hartog
May 2025

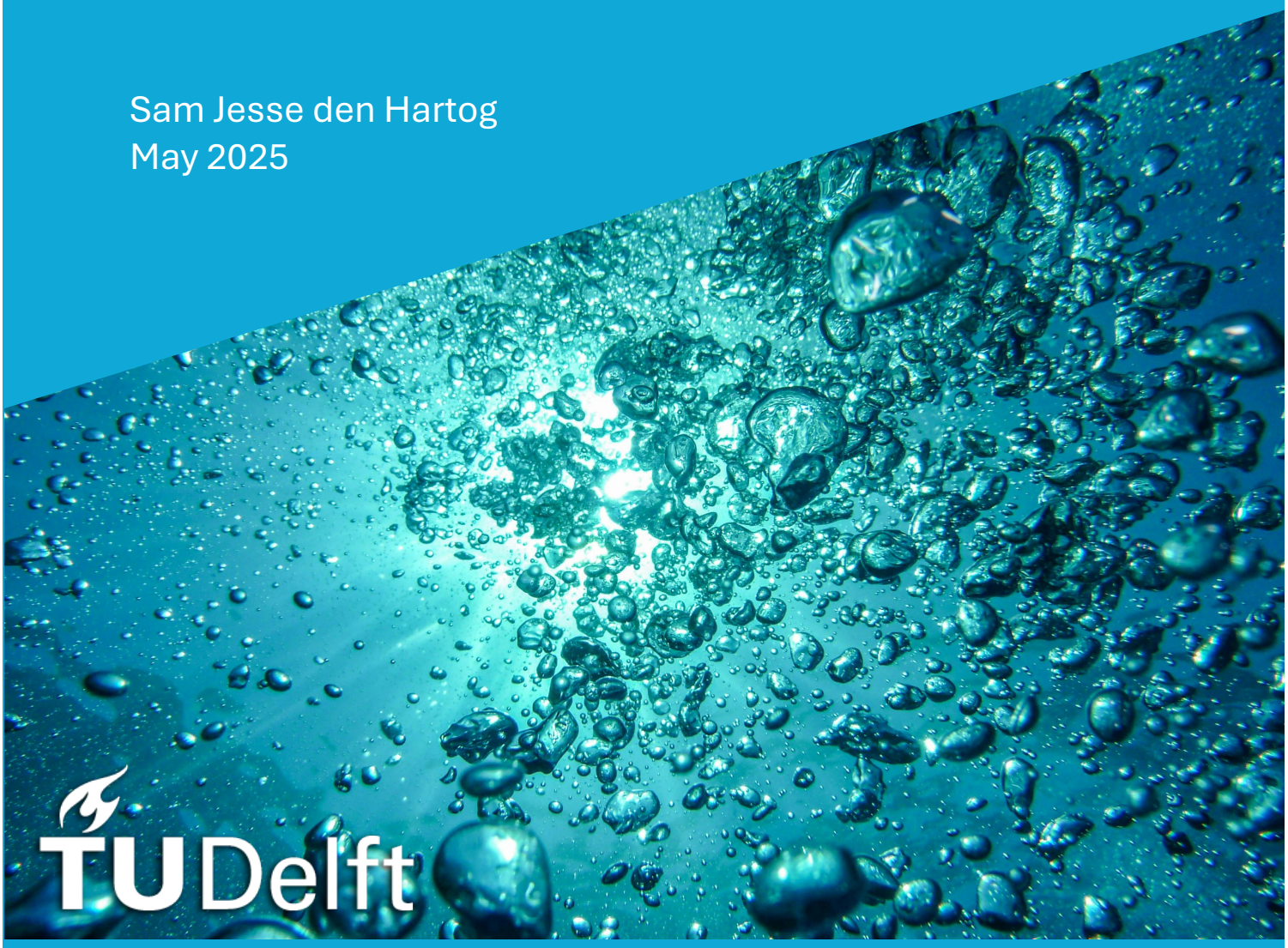

TU Delft

MSc Thesis in Life Science & Technology

Gas Holdup in Bubble Column Reactors: Influence of Fermentation-Relevant compounds and Advances in X-ray Tomographic Measurements

A Study on the Impact of Alcohols and Acids on Gas Holdup and Beam Hardening Correction in XRT

Sam Jesse den Hartog
May 2025

A thesis submitted to Delft University of Technology in partial fulfilment of the requirements for the degree of Master of Science in Life Science & Technology

Supervisors: Ir. Rik Volger
Prof. Cees Haringa

Committee: Dr. Cees Haringa
Dr. Pouyan Boukany
Prof. Dr. Merle de Kreuk

Bioprocess Engineering
Delft University of Technology

Abstract

Bubble column reactors (BCRs) are valuable in the biochemical industry for their efficient gas-liquid mass transfer and mixing capabilities. A key performance parameter in BCRs is gas holdup, which can be significantly influenced by components present in fermentation broths. This study investigated the effect of the important fermentation products ethanol, *n*-propanol, *iso*-propanol, *n*-butanol, acetic acid, and lactic acid on gas holdup. These components impact bubble coalescence via the so-called Marangoni effect. This study correlates gas holdup with the dimensionless Marangoni number (Ma) in BCRs. The model proposed by Wang et al. [1] successfully predicts 87% of the measured holdup values within a 10% error margin. Additionally, correlations for gas holdup distribution are compared, with Schweitzer et al. [2] providing the most accurate local predictions (70% within 10% error). This study provides a comparative overview of gas holdup correlations relevant to BCRs and demonstrates the significance of incorporating the Marangoni effect in predictive models.

Research on local gas holdup in BCRs often requires invasive measurement techniques. X-ray tomography (XRT) enables measurements of gas without disruption of the flow associated with traditional methods such as optical fiber probes. However, noise from X-ray scattering and artifacts from beam hardening still hinder accurate quantification of gas holdup. This study presents a methodology for processing X-ray data to overcome these challenges. X-ray data corrected for scatter and beam hardening results in tomographic reconstructions with a gas holdup profile similar to what was found with an optical fiber probe. This correction methodology can assist other researchers using similar X-ray setups by improving the accuracy of gas holdup measurements in multiphase systems.

Acknowledgments

I have been working on this thesis for the past 9 months, but this was of course not without the help of others.

First of all, I would like to thank my daily supervisor Rik Volger for his great help throughout my project. Your enthusiastic and patient way of explaining made the whole experience a lot better. I also look back on a great few weeks in the X-ray basement of the Reactor Institute Delft. this work would not have been possible without your help.

I would also like to thank two other "Bubbly Flow Followers" (former: Bubble Buddies"). First, my supervisor Cees Haringa for the sharp comments and good ideas during our biweekly meetings and for reviewing my work. I would like to thank Pieter van der Wilt for his explanations on complex topics and his good ideas during the weekly meetings.

Furthermore, I would like to express my gratitude to Prof. Merle de Kreuk and to Prof. Pouyan Boukany for participating in my thesis committee. I hope you will enjoy reading my work.

Moreover, I would like to thank the Bioprocess Engineering section and especially the CASE group for the good atmosphere and all the cake.

Lastly, I would like to thank my family, friends and housemates for the fun times outside office hours. You helped me to step away from my work to relax, laugh, and recharge.

Contents

Nomenclature

Abbreviations

BCR	Bubble Column Reactor
BHC	Beam Hardening Corrected
BSD	Bubble Size Distribution
CFD	Computational Fluid Dynamics
HPLC	High Performance Liquid Chromatography
ILAR	Internal-Loop Airlift Reactor
MAPE	Mean Absolute Percentage Error
MEA	Mean Absolute Error
RMSE	Root Mean Squared Error
SC	Scatter-Corrected
SIRT	Simultaneous Iterative Reconstruction Technique
XRT	X-Ray Tomography

Symbols

A	Area	m^2
a	Interfacial area	m^2
C_V	Volumetric solid concentration	m^3/m^3
c	Concentration	mol/l
D	Diameter	m
d	Diameter	
d_{32}	Ratio of the sum of volumes to the power of 3 over the sum of areas squared of all bubble	
D_l	Diffusion coefficient	
D_X, D_Y, D_Z	x, y and z coordinates of the detector	
H	Height	m
g	Gravitation constant	m/s^2
I	Intensity of pixel	
k_L	Liquid-side mass transfer coefficient	m/s
K_d	Distributor coefficient	
μ	Attenuation coefficient	$1/m$
n_c	Number of carbon atoms in a molecule	
N_c	Number of pixel columns on the detector	
N_o	Number of orifices	

N_r	Number of pixel rows on the detector	
P	Pressure	Pa
P_S	Vapor pressure	Pa
P_T	Total pressure	Pa
ρ	Density	kg/m^3
r	Radius	m
$S_x,\ S_y,\ S_z$	x, y, and z coordinates of an X-ray source	
σ	Surface tension	Pa s
U_g	Superficial gas velocity	m/s
u	Horizontal unit vector	
v	Vertical unit vector	
V	Diameter	m
V	Approach velocity	m/s
V	Volume	m^3
X_W	Weight fraction of the primary liquid in the mixture	
Z	Distance from sparger plate	m
ξ	Non-dimensional radius, r/R	
η	Dynamic viscosity	Pa s
ϵ	Holdup	
$\overline{\epsilon}$	Mean holdup	
$\tilde{\epsilon}$	Radial chordal average holdup	
Γ	Surface excess	mol/m^2

Subscripts

0	Before aeration
b	Bubble
c	Column
eq	Equilibrium
g	Gas
l	Liquid
o	Orifice
t	Transition
corr	Corrected
empty	Empty column

Dimensionless Numbers

Ar	Archimedes number
Bo	Bond number
Ca	Dimensionless capillary number
D_H	Dimensionless diameter
Eö	Eötvos number
Fr	Froude number
Ga	Galileo number
Ma	Marangoni number
Pe	Peclet number
Re	Reynolds number

1 Introduction

Bubble columns reactors (BCRs) are a widely used multiphase reactor type. Bubble columns have applications in chemical, biochemical, petroleum and, metallurgical industries in processes like hydrogenation, oxidation, chlorination, hydroformylation, cell growth, bioremediation, etc. [3, 4]. In these reactors, gas is introduced into a continuous liquid phase through a sparger at the bottom of a vertical column, creating buoyancy-driven flow and inducing liquid circulation [4]. The basic design is relatively simple (typically a cylindrical vessel without internals) but the resulting flow is characterized by complex hydrodynamic interactions. The liquid phase can operate in batch, co-current, or counter-current mode, depending on the process requirements [5].

In the context of climate change, reducing greenhouse gas emissions from the extraction and combustion of fossil fuels is increasingly important [6]. Bubble columns are valuable in the biochemical industry for their efficient gas-liquid mass transfer and mixing capabilities. An important application is the fermentation of sugars to produce bioethanol [7]. Furthermore, converting gaseous substrates such as O_2, CO_2, CO, H_2, and CH_4 into liquid products is a promising technology for sustainable production. These gas fermentation processes utilize low-value carbon feedstocks from industrial waste gases, syngas from gasified municipal solid waste or biomass, and CO_2 sources like industrial processes or direct air capture, often combined with green hydrogen.

Gas fermentation processes are currently capable of producing a variety of compounds, including acids, alcohols, diols, aromatics, and ketones [8]. To optimize and commercialize these processes, a better understanding of gas-liquid interactions within reactors like bubble columns is essential. While most research to date focuses on oxygen or air in water, similar mass transfer behavior is expected for other sparingly soluble gases [9]. As such, air is often used as a model for gases like syngas in fermentation studies [8].

A crucial parameter in the performance of BCRs is gas holdup. The term gas hold-up refers to the proportion of the reactor volume that is occupied by gas. Models for making predictions on BCRs are often zero-dimensional (0-D), considering only the global hold-up of the reactor, or one-dimensional (1-D), accounting solely for holdup variations along the axial direction. More advanced models, such as computational fluid dynamics (CFD), have very high uncertainties because the physical models used are often based on relations from water-air systems [10]. However, components in fermentation broth can drastically influence the gas holdup. So, two major assumptions are often made: gas fermentation only includes air and water (1) and gas holdup is 0-D or 1-D (2). These two assumptions have major implications for modeling BCRs.

Firstly, in fermentation processes, medium components and products (e.g. anti-foam, biomass, surfactants, alcohols, acids and salts) can strongly affect parameters like gas holdup and k_La. The most significant difference is that in an aqueous solution the coalescence rate is lower than in water [11]. Even though the effect of a wide variety of medium components on gas-liquid interactions is important for optimizing and commercializing gas fermentation processes, this research only focuses on the effect of ethanol, 1-propanol, *iso*-propanol, 1-butanol, acetic acid and lactic acid. Those compounds are already considered to be interesting products to scale-up production or for commercialize production [8]

Secondly, spatial variations in gas concentration, directly affect mass transfer rates and the microenvironment experienced by cells. Without accounting for these local differences, reactor performance predictions can be inaccurate, potentially leading to suboptimal process conditions and reduced yields [12]. Therefore, this study will focus on the gas holdup distribution.

The hydrodynamic behavior of bubble column reactors (BCRs) is strongly influenced by the presence of organic solutes, with numerous studies exploring their effects on phenomena such as bubble coalescence and gas hold-up. Organic compounds, such as alcohols, can reduce bubble coalescence by adsorbing at the gas–liquid interface and modifying surface properties (see Chapter 2.3). A critical mechanism underlying this behavior is the Marangoni effect, which arises from surface tension gradients caused by variations in surfactant concentration at the bubble interface. These gradients induce fluid motion that stabilizes the bubble surfaces and inhibits coalescence, leading to increased gas hold-up and interfacial area for mass transfer [13, 14, 1]. Correlating dimensionless numbers relevant to bubble coalescence to gas holdup is promising. Therefore, this study will validate existing experimental work for a water-ethanol system by Wang et al. [1] and extend that work for other relevant alcohols and acids.

The current study will also discuss existing correlations for the radial gas holdup distribution. Different measuring techniques exist for measuring the local gas holdup. This study will use an optical fiber probe (see Chapter 2.5). The technique's affordability and portability make it ideal for industrial applications [15]. Moreover, an optical fiber probe is used in this study to validate a non-invasive method to measure local gas holdup, based on X-ray tomography. The invasive nature of optical fiber probes impacts the hydrodynamic behavior of the BCR. Therefore, non-invasive measurement techniques are more favorable for correlating fluid properties with local gas holdup.

The second part of this thesis is focused on the method development of X-ray tomography for multiphase reactors. X-ray tomography is a powerful, non-invasive imaging technique that has been applied in the study of bubble columns to investigate their complex internal hydrodynamics. In bubble columns, gas is dispersed through a liquid phase, leading to dynamic, three-dimensional distributions of bubbles that are difficult to characterize using traditional optical methods. In this technique, an X-ray beam is passed through the column, and the attenuation (see Chapter 2.6.3) of the X-rays is measured as they pass through different materials in this case liquid and gas. Since gas and liquid have different X-ray attenuation coefficients, it becomes possible to reconstruct three-dimensional images of the gas holdup distribution.

The current challenges for this measurement technique include X-ray scattering and beam hardening (see Chapter 2.6.3).Campton scattering is the most dominant form of attenuation in the system used in this study. Compton scattering occurs when an incoming X-ray photon collides with an electron, causing the electron to be ejected from its orbit. As a result of this interaction, the X-ray photon loses energy and changes direction, continuing to travel through the material along a new path. Instead of traveling straight through the object to the detector as expected, the scattered photon may hit a different location on the detector (forward scatter) or reach an entirely different detector (cross-scatter). Photons detected at random places due to scattering add noise to the data [16]. Forward and cross-scatter result in different types of noise.

Beam hardening results in a reduction of image intensity in the central region of the BCR. This occurs because lower-energy photons (soft X-ray) are preferentially attenuated (see Chapter 2.6.3) over longer path lengths. As the beam hardens and the mean photon energy increases, the corresponding attenuation coefficients decreases along longer paths [17]. The developed set-up has been used for multiple applications including fluidized beds and bubble columns. An earlier study showed there is no significant effect of beam-hardening for measurements on fluidized beds [18]. However, the current work shows the effect of beam hardening for measurements on BCRs. This work also explains a method to correct X-ray images for beam hardening to reduce artifacts in reconstructions.

2 Theoretical Background

2.1 Gas Holdup

Gas hold-up can be determined by measuring the increase in liquid height in the column. In this case, ϵ_G is calculated according to Eq. 1. Where H_l is the liquid height after aeration and H_0 is the liquid height before aeration [19]. This measurement technique has a high uncertainty because of the high variability of the liquid height after aeration (e.g., because of foam formation). Measurement of pressure difference is a more reliable measurement technique and less dependent on human interpretation. Pressure difference measurements also enable the possibility to measure gas holdup in a specific region of the reactor. The liquid holdup is calculated by measuring the pressure difference between two heights of the reactor and divide that by the hydrostatic pressure of that part of the reactor. The gas holdup is then calculated by subtracting the liquid holdup from 1 (see Eq. 2).

$$\epsilon_G = \frac{H_l - H_0}{H_l} \tag{1}$$

$$\epsilon_G = 1 - \frac{1}{\rho_l g}\left(\frac{\Delta P}{\Delta Z}\right) \tag{2}$$

2.2 Flow Regimes

In a bubble column, fluid dynamics phenomena happen on different scales: molecular-scale, bubble-scale and reactor scale. The molecular-scale is important to study interfacial phenomena, catalysts and gas conversion processes, and to formulate mass transfer models. The bubble-scale is important to understand bubble size distributions (BSDs), bubble shapes, single bubble dynamics, "non-coalescence-induced" bubble dynamics (e.g. bouncing, sliding, deformation, or wake interactions between bubbles) and coalescence-induced behavior. At reactor scale (e.g. laboratory-scale), the medium and large-scale circulations are studied. Scale-up methods applied on experimental, reactor-scale facilities, can estimate the fluid-dynamics on an industrial-scale [20].

2.2.1 Homogeneous Flow Regime

The interactions between the gas and liquid phase can be classified into flow regimes. The boundaries between the regimes change when the system design parameters or the phase properties are changed. However, the properties and main characteristics of the flow regimes stay the same. Three main flow regimes can be defined: homogeneous (bubbly), heterogeneous (turbulent) and slug flow. The mono-dispersed homogeneous flow regime is characterized by mono-dispersed BSD. An increased U_G results in more bigger bubbles with a negative lift force coefficient [21]. These larger bubbles tend to migrate laterally inward toward the center of the column, destabilizing the flow and promoting the transition to a heterogeneous regime. This results in coalescence induced bubbles [22].

2.2.2 Heterogeneous Flow Regime

The heterogeneous flow regime, also known as the churn-turbulent regime, happens in bubble columns when the superficial gas velocity is relatively high. This is the flow regime most often seen in industrial bubble columns [23]. It is characterized by strong mixing and turbulence, which cause bubbles to collide and combine frequently. As a result, the column contains many large bubbles, leading to a wide range of bubble sizes, unlike the more uniform and smaller bubbles seen in the homogeneous regime [23, 10]. In this regime, the gas holdup still increases with gas velocity, but not as quickly as in the homogeneous flow. The transition from homogeneous flow to heterogeneous flow can be detected by looking at things like gas holdup, mass transfer rates, and pressure signals [23].

In the heterogeneous flow regime of bubble columns, bubbles are unevenly spread out, and gravity helps create circulating flow patterns and vortices of different sizes [24]. These swirling structures are part of the turbulent motion in the column and play a big role in how energy is spread and used. As turbulence breaks down into smaller and smaller motions, energy is lost through dissipation, especially near the bubble surfaces

[25]. This process causes the liquid to move and fluctuate, which helps renew the liquid at the bubble surface and improves how gas is transferred into the liquid [26]. Because of this, the energy dissipation rate (EDR) is often used in formulas to describe how turbulence affects the mass transfer rate (k_La) [27]. The higher rise velocity and bigger bubbles have a negative effect on the interfacial area (a), but heterogeneous flow strongly enhances liquid mixing [10].

2.2.3 Slug Flow Regime

At industrial scale, the slug flow does not occur due to large diameter effects. As the column diameter increases, Rayleigh–Taylor (RT) instabilities become increasingly dominant. Rayleigh–Taylor instability is a type of interfacial instability that occurs when a lighter fluid is accelerated into a heavier fluid. In the context of bubble columns, this instability occurs at the gas–liquid interface when buoyant gas regions (bubbles or clusters) rise through a denser liquid medium. At large diameters, these instabilities disrupt the formation and maintenance of coherent cap bubbles that are necessary for slug flow. Instead of forming stable gas slugs, the interface between the phases becomes unstable, leading to the breakup of large bubbles and the formation of irregular bubble swarms or clusters [20]. Rayleigh-Taylor instabilities are quantified by the dimensionless diameter, D_H (Eq. 3) [21].

$$D_H^* = \frac{D_H}{\sqrt{\frac{\sigma}{g(\rho_L - \rho_G)}}} \tag{3}$$

In Eq. 3, D_H is the hydraulic diameter, D_c is the inner diameter of the bubble column, σ is the surface tension, g is the acceleration due to gravity and $\rho_L - \rho_G$ is the density difference between the two phases. When the hydraulic diameter is larger than the critical value ($D^*_{H,cr} = 52$ [28]), coalescence-induced bubbles appear instead of the slug flow regime. A column diameter (d_c) of 13-15 cm (for circular columns at ambient pressure and temperature) is already considered as large scale column, since these columns have a critical hydraulic diameter above 52 [20]. Thus, the slug flow does not appear in industry. The annular flow regime is also not observed at industrial scale since the gas velocity needed is too high to achieve at this scale [20]. Hydrodynamic observations in air-water systems are translatable between scales for column diameters (D_C) of 15 cm or higher, and a liquid height (H_L) column diameter (D_C) ratio greater than 5 according to several studies [29, 30, 31]. The aspect ratio of height to diameter does not influence gas holdup for column with a diameter more than 20 cm and a height of 2.2 m [32].

2.2.4 More Flow Regimes

More recently, some researchers claim there are six flow regimes: (1) the mono-dispersed homogeneous flow regimes; (2) the pseudo-homogeneous flow regime; (3) the transition flow regimes without coalescence-induced structures; (4) the transition flow regimes with coalescence-induced structures; (pseudo-heterogeneous flow regimes; and (6) the pure-heterogeneous flow regime. The different flow regimes can be observed by increasing the superficial gas velocity (U_G) [33].

2.3 Impact of Alcohols and Acids on BCR Hydrodynamics

Bubble coalescence plays a crucial role in determining the overall performance of bubble column reactors. When two bubbles approach each other in pure water, the liquid film between them typically drains rapidly, leading to coalescence. However, organic molecules dramatically alter this process through several mechanisms. The inhibition of bubble coalescence by organic molecules directly impacts the overall performance of bubble column reactors, particularly through their effects on gas holdup and flow regime transitions.

2.3.1 Mechanisms That Inhibit Coalescence

Protective Layer

Alcohols and other organic compounds inhibit bubble coalescence primarily by forming a protective layer at the gas-liquid interface. These molecules behave like hydrophobic materials and are rejected from the bulk solution, causing them to adsorb strongly at bubble surfaces [34]. This adsorption creates a physical barrier

that prevents bubbles from merging when they come into contact. The effectiveness of this protective layer increases with the carbon chain length of the alcohol, as longer-chain alcohols demonstrate stronger surface activity [35, 36]. This explains why higher alcohols like pentanol, hexanol, and octanol show more pronounced coalescence inhibition effects than methanol or ethanol at equivalent concentrations [35].

The Marangoni Effect

Surface-active substances decrease the mobility of the gas–liquid interface and suppress bubble coalescence, leading to an increase in gas holdup and interfacial area for mass transfer. This effect is known as the Marangoni effect [13, 14]. The Marangoni number (Ma) is a dimensionless number that represents the relative importance of surface tension gradients to viscous forces in a fluid. It is used to quantify the Marangoni effect, which arises from surface tension gradients caused by variations in surfactant concentration at the gas-liquid interface. Wang et al. defines the Marangoni number (Ma) according to Eq. 4.

$$Ma = \frac{(\frac{\partial \sigma}{\partial \Gamma})\Gamma_{eq}}{C_a^{2/3}\sigma} \tag{4}$$

- $\frac{\partial \sigma}{\partial \Gamma}$ represents the surface tension gradient with respect to the surface concentration of the surfactant.
- Γ_{eq} is the surface concentration of the surfactant at adsorption equilibrium.
- C_a is the dimensionless capillary number, defined as $C_a = \frac{\mu_b V}{\sigma}$, where μ_b is the dynamic viscosity of the gas, V is the approach velocity of bubbles in the bubble coalescence model, and σ is the surface tension.

When two bubbles meet each other, a dimple starts to form [37]. That is the liquid pocket between two bubbles. Surfactant-like molecules (e.g. ethanol molecules) trapped in the dimple, migrate towards the gas-liquid interface. As a result, the dimple is depleted from surfactant molecules. The surface tension of water is higher than the surface tension of organic compounds. Thus, the depletion of surfactant molecules in the dimple results in a surface tension gradient with a relatively high surface tension in the dimple and a low surface tension in the bulk liquid. The surface tension gradient is the driving force for liquid to move from the bulk towards the dimple. This prevents bubbles to coalesce [38, 1]. When the concentration exceeds a certain threshold, the difference between the bulk and dimple concentrations disappears, diminishing the surface tension gradient. As a result, pressure gradients and capillary forces drive bubble coalescence [1].

Wang et al. [1] described the effect of increased ethanol concentration on various characteristics that influence the hydrodynamics of a system, including bubble coalescence time, $k_L a$ and ϵ_g in an internal loop airlift reactor (ILAR) with elevated pressure. It was found that these increased for an increased mol fraction of ethanol up to a mol fraction of 0.012. Then the values decreased dramatically for an increasing mol fraction up to 0.03. Addition of more ethanol resulted in a less dramatic linear decrease of bubble coalescence time, $k_L a$ and ϵ_g. Wang et al. [1] describes that the Marangoni effect is responsible for the effects of ethanol on bubble coalescence time, $k_L a$ and ϵ_g. Their model accounts for both the velocity of film drainage and the mass transfer occurring between the interface and the surrounding liquid film [1].

In the semi-empirical correlations proposed in the study [1], a modified Marangoni effect number for gas holdup $(1 + 3000Ma^{2.0}Pe^{-4.2})^{4.6})$ and for the mass transfer coefficient $(1 + 3000Ma^{2.0}Pe^{-4.2})^{3.1})$ is used, where Pe is the film Peclét number. The exponents of Ma and Pe were adjusted to obtain a number that exhibits a similar trend to the variation of bubble coalescence time with ethanol mole fraction. The film Peclét number (Pe) is defined as $Pe = \frac{R_{eq}V}{D_l}$, where R_{eq} is the radius of the bubble in the bubble coalescence model and D_l is the bulk diffusion coefficient.

Critical Transition Concentration

The mechanisms discussed above—surface adsorption and the Marangoni effect—are highly dependent on the concentration of organic additives. A particularly interesting concept is the existence of a critical transition concentration (c_t) at which coalescence behavior changes dramatically. Zahradník et al. [39] found that coalescence is reduced from 100% of bubble pairs coalescing to less than 10% of bubble pairs coalescing in a very narrow alcohol concentration range. The concentration at which this sharp change of coalescence behavior appears is called the transition concentration (c_t). The transition concentration is correlated as function of number of carbon atoms in the alcohol molecule (n_c) in $c_t = a n_c^b$ [39]. With

fitting parameters $a = 31$ and $b = -7.2$ for aqueous solutions of alcohols. This correlation is based on alcohols with 1 alcohol group on the first carbon atom [39]. It remains uncertain if this relation is valid for alcohols that do not have these characteristics (e.g. *iso*-propanol). Such correlations improve the prediction of coalescence in BCR, but lack information about the effect of complex fermentation broths including alcohols. Some understanding of the coalescence inhibiting mechanism is required.

2.3.2 Effects on Reactor Hydrodynamics

Enhanced Gas Holdup

The addition of alcohols and organic acids to water significantly increases gas holdup in bubble columns by reducing bubble coalescence and decreasing bubble size [40, 11]. This effect is especially noticeable in the heterogeneous flow regime at higher gas velocities, as shown by Krishna et al. [41] in their studies with ethanol. They investigated the influence of elevated pressure and alcohol addition on gas holdup and found that gas holdup increased significantly at higher ethanol concentrations, particularly under high U_g where flow is heterogeneous [41]. Alcohols prevent coalescence by adsorbing at the gas–liquid interface, forming a protective monolayer around the bubbles [41, 34]. Because these molecules are hydrophobic, they are rejected from the bulk liquid and accumulate at the bubble surface, especially on the lower side as the bubble rises. This creates a surface barrier that resists merging with other bubbles and also increases drag, reducing the bubble rise velocity [41]. These effects help maintain smaller bubbles and contribute to stabilizing the bubbly flow regime, which in turn increases gas holdup. The observed increase in gas holdup can be explained by a shift in the regime transition point caused by reduced coalescence. For concentrations relevant to gas fermentation, the effect of alcohols on gas solubility is considered negligible [42]. However, the relationship between ethanol concentration and gas holdup is not linear. Wang et al. found that gas holdup increases with ethanol concentration up to a mole fraction of about 0.012, after which it decreases with further addition.

Flow Regime Transition

Organic molecules significantly affect the transition between flow regimes in bubble columns. In pure water systems, bubble columns typically transition from a homogeneous (bubbly) flow regime to a heterogeneous (churn-turbulent) regime as gas velocity increases [40, 23]. The addition of alcohols and other surface-active compounds delays this transition, extending the homogeneous flow regime to higher gas velocities [3]. This delay in regime transition occurs because surface-active compounds stabilize smaller bubbles and prevent their coalescence into larger bubbles that would drive the shift to heterogeneous flow [10, 3].

A recent study shows quantitative correlations that predict the transitional superficial gas velocity ($U_{g,t}$) and gas holdup at the transition ($\epsilon_{g,t}$, and these correlations incorporate the liquid properties that are affected by the addition of surface-active compounds (Eq. 5 and Eq. 6), thereby attempting to quantify the delay or shift in the transition point caused by these additives [23]. Other researchers also discuss the factors influencing the transition, such as liquid viscosity and the addition of alcohols, and note that they affect the transition velocity and flow regime stability [43]. Nedeltchev et al. [44] discusses identifying transition velocities using a new parameter (NHI) and compares its findings to existing empirical correlations from other researchers, but notes these existing correlations are not always effective.

$$U_{g,t} = 1.803\rho_g^{0.155}\rho_l^{-0.628}\eta^{-0.216}\sigma^{-0.306} \tag{5}$$

$$\epsilon_{g,t} = 1.452\rho_g^{0.273}\rho_l^{-0.536}\eta^{-0.184}\sigma^{-0.0181} \tag{6}$$

Differential Effects of Alcohols and Organic Acids

While both alcohols and organic acids inhibit bubble coalescence, their effects on bubble size and gas holdup differ in magnitude. Carboxylic acids produce more pronounced decreases in bubble diameter than alcohols [45, 34]. This difference is attributed to the stronger surface activity of organic acids compared to alcohols with similar carbon chain lengths. The differential effects extend to gas holdup as well. Short-chain organic acids like acetic and propionic acids generate stronger increases in gas holdup compared to alcohols with similar molecular weights [11].

2.4 Mass Transfer

Research in the field of gas fermentation focuses on improving the transfer of mass from the gas phase to the liquid phase, since gas-to-liquid mass transfer and low concentrations of dissolved gas are considered limiting factors [9]. The speed with which a gas can dissolve into a liquid per unit of volume in a system is given by the volumetric mass transfer coefficient (k_La). This parameter consists of two parts: k_L and a. k_L is the mass transfer coefficient for the gas-liquid interface. The rate at which a gas dissolves in the liquid is the unit area of the gas-liquid interface. The higher k_L, the faster the gas can transfer to the liquid. a is the specific interfacial area. The gas-liquid interface area is the area available for mass transfer per unit volume of the liquid. The value of k_La is influenced by many factors. Important factors are the d_{32} and gas holdup (ϵ_G). The d_{32} is calculated using Eq. 7, where $V_{b,i}$ is the volume of the bubble i, $A_{b,i}$ is the surface area of the bubble and $d_{b,i}$ is its chord length. The d_{32} provides a meaningful average diameter that accounts for both the surface area and volume of bubbles.

$$d_{32} = 6\frac{\sum_i V_{b,i}}{\sum_i A_{b,i}} = 6\frac{\frac{4}{3}\pi\sum_i(\frac{1}{2}d_{b,i})^3}{4\pi\sum_i(\frac{1}{2}d_{b,i})^2} \tag{7}$$

The specific area is strongly affected by organic compounds because they affect both gas holdup and bubble diameter. Experimental research found that addition of organic solutes increases the surface area and decreases the average bubble diameter [38]. For a wide variety of alcohols, it is possible to increase the k_La five times within a small range of concentrations. This phenomenon is explained by a two-fold increased ϵ_G [34] and a decreased d_{32} (from 4 mm to 1 mm) [46] according to the relation of the specific area in Eq. 8 [34].

$$a = \frac{6\epsilon}{d_{32}} \tag{8}$$

2.5 Fiber Probe

In the present study, fiber probe is used to determine local gas holdup and bubble size distribution in a BCR. The fiber optic Doppler probe is a sensor designed for investigating gas-liquid flows at the microscale. The probe operates on two fundamental principles: phase detection and Doppler-based velocity measurement [47].

In phase detection mode, coherent light is injected into the fiber, and part of it is reflected at the tip. The intensity of the reflected signal is strongly influenced by the refractive index of the surrounding medium, resulting in high signal levels in gas (in this study air) and significantly reduced signal levels in liquids (e.g., water). This contrast allows for accurate detection of whether the fiber tip is in a gas or liquid phase. By applying signal amplitude thresholds, bubble entry and exit events can be detected, enabling the calculation of gas residence time at the probe tip [47].

Simultaneously, the probe utilizes the Doppler effect to measure the velocity of moving gas-liquid interfaces. When a bubble or interface approaches the tip, light reflected from the moving surface experiences a Doppler shift. This shifted light interferes with the light statically reflected at the fiber tip, producing a modulated signal whose frequency (Doppler frequency) is proportional to the interface velocity along the probe's optical axis. The probe is sensitive only to bubbles that travel straight toward the conical tip [47].

2.6 X-Ray Tomography

2.6.1 X-Ray as Measurement Technique

Process tomography, including X-ray and gamma tomography, is described as a non-intrusive technique capable of measuring phase distribution inside multiphase equipment without disturbing normal operations [48, 49], unlike some other measurement techniques for bubbly flows, which can be intrusive, like fiber probe measurements. Additionally, X-ray measurements enable to quantify opaque multiphase flow fields [48]. X-ray tomography, often referred to as Computed Tomography (CT) is an imaging method used to infer the interior of an object from a series of X-ray radiographic projection measurements, taken from different angles. Essentially, it aims to reconstruct an object from its projections [50].

To understand what's inside an object, CT systems take many X-ray measurements from different angles. The goal of X-ray computed tomography (CT) is to reconstruct the internal structure of an object using a series of X-ray images taken from different angles [51]. Mathematically, this is known as an inverse problem, because we're working backwards from the measurements to figure out the internal structure [50].

When an X-ray beam is sent through the object, some of its energy is absorbed or scattered by the material. This energy loss is described by attenuation, which depends on the properties of the material the beam passes through. The total attenuation along a beam's path is the sum (or integral) of all the small attenuations it experiences inside the object [50].

Detectors on the other side measure how much the X-ray beam has been weakened after passing through the object. At each projection angle, this gives us a one-dimensional profile (like a shadow) showing how much X-ray energy was absorbed across the detector. This profile is called $p_\gamma(\xi)$, where γ is the projection angle and ξ is the position along the detector [50].

However, one projection is not enough to reveal what's inside. It only shows a flattened view. To get a complete picture, the system rotates the object (or the source-detector setup) and collects these shadow-like profiles from many different angles, usually covering at least 180 degrees. When we plot all these 1D profiles side by side, with angle on one axis and detector position on the other, we get a pattern called a sinogram. This sinogram is the raw data from which the internal structure can be mathematically reconstructed [50].

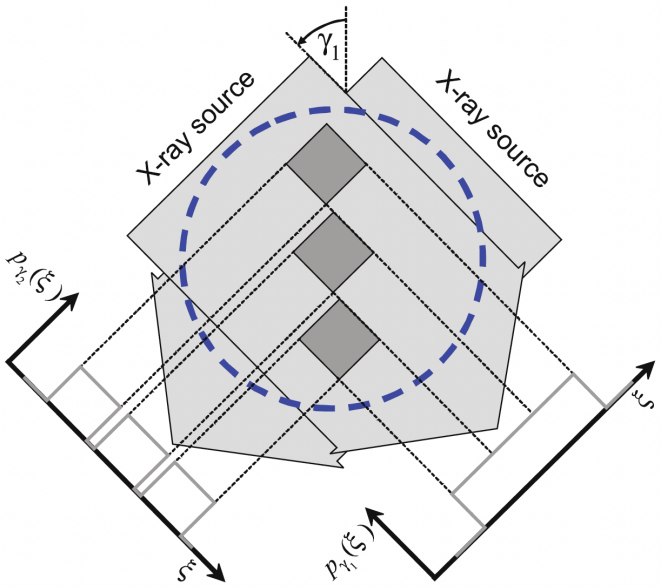

Figure 1: *Illustration of X-ray projections through three homogeneous objects with quadratic intersection areas. The objects are exposed to X-rays at two projection angles, γ_1 and γ_2. Each projection results in a specific attenuation profile $p_\gamma(\xi)$, corresponding to the integral of attenuation along each ray in the detector array. Dashed lines indicate the geometric boundaries of the resulting shadows. The profile at angle γ_1 alone does not provide sufficient information to determine the number or arrangement of distinct objects, highlighting the need for multiple projections in CT imaging. This figure was adopted from Buzug [50]*

2.6.2 SIRT

There are different reconstruction methods to solve the inverse problem. The current study makes use of Simultaneous Iterative Reconstruction Technique (SIRT). SIRT is an algebraic technique useful in situations with a low number of projection angles [52]. In the X-ray setup used in this study only has 3 angles are used, which is fewer than normally used in CT. This makes the reconstruction challenging, and traditional methods like filtered back projection (FBP) do not give good results [53].

The mathematical model that connects the measured X-ray data to the unknown 3D image is shown in Eq. 9[53].

$$A \cdot x = y \tag{9}$$

Where A is a linear operator (matrix) that models the line integrals. It encodes the geometry of the setup. x is a vector denoting the reconstruction. It is the image we are trying to reconstruct. y is a vector containing the measured data. So, all pixels from the three detectors.

The equation (Eq. 9) means that for a known image x with known geometry A, it is possible to predict measurements y. In the case of CT, we have the measurements y and the system A and we want to find the image x. SIRT solves this inverse problem iteratively. It starts with a rough guess for the image and then keeps adjusting it to better match the actual measurements [53, 54]. So, from the image guess $x^{(k)}$ (at iteration k), it predicts projections ($Ax^{(k)}$). Then it compares the projections from the measurements (y) with the predicted measurements by subtracting the prediction from the real projection ($y - Ax^{(k)}$). Then the image guess is updated based on the difference between the guess and the measurement. Too many iterations can result in overfitting to the noise of the measurements. Mathematically the update steps are defined as in Eq. 10 [54].

$$x^{(k+1)} = \Pi_\Lambda \left(x^{(k)} + CA^T R \left(y - Ax^{(k)} \right) \right) \tag{10}$$

Where Π_Λ includes the constraint set, forcing $x^{(k+1)}$ between 0 and 1, and sets $x^{(k+1)}$ to zero outside the column (also referred to as the masked area). R is a diagonal matrix containing reciprocals of row sums of A. So, R acts like a weight. C is a diagonal matrix of column sums, which preconditions the gradient descent solver. The solver optimizes a constraint weighted least-squares minimization problem (Eq. 11) [53].

$$x^\star = \arg\min_{x \in \Lambda} \|Ax - y\|_R^2 \tag{11}$$

Where $x^\star$ is the least-squares solution, and Λ enforces x between 0 and 1 inside the column and x=0 outside the column (in the masked area).

The result SIRT is a sequence of 3D volumes that approximate the internal structure of the object, enabling the visualization and analysis of dynamic phenomena such as bubble formation and movement in fluidized beds. In the current study SIRT is used to make time-averaged reconstructions of a BCR.

2.6.3 X-ray attenuation

When X-ray travels through a material, it attenuates, meaning it loses intensity. There are different mechanisms resulting in X-ray attenuation. Three main mechanisms causing attenuation are Rayleigh scattering, Compton scattering and photoelectric absorption. Pair production and photodisintegration are other processes causing attenuation. However, due to the high energies involved, these mechanisms can be neglected in radiography [55].

The mechanism that most prominently contributes to attenuation depends on the incident energy of the X-ray [56]. Compton scattering is most prominent for photon energies beyond 100 keV (see Fig. 2).

Compton scattering occurs when an incoming X-ray photon collides with an electron, causing the electron to be ejected from its orbit. As a result of this interaction, the X-ray photon loses energy and changes direction, continuing to travel through the material along a new path. Throughout this process, both energy and momentum are conserved. The amount of energy lost by the photon depends on the angle at which it is scattered, rather than the type of material it interacts with. Because the scattered photon has lower energy, it has a longer wavelength and reduced penetrating power compared to the original incident photon [55].

The change in direction has implications for X-ray measurements. Instead of traveling straight through the object to the detector as expected, the scattered photon may hit a different location on the detector (forward scatter) or even reach an entirely different detector (cross-scatter). Photons detected in unexpected places due to scattering add noise to the data [16]. The direction of the scattered beam is not completely random but depends on the energy of the source [57]. Forward and cross-scatter result in different types of noise.

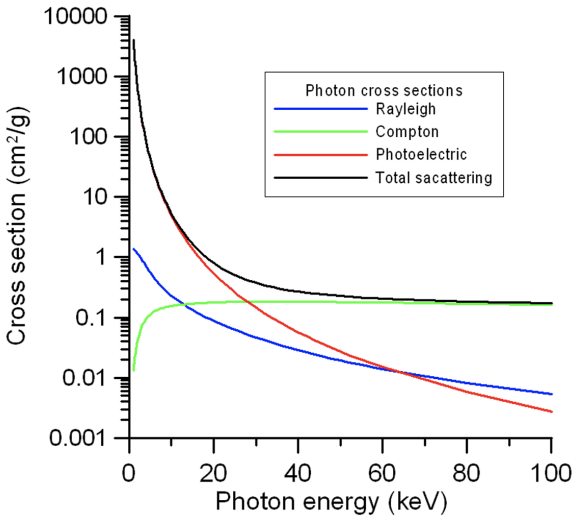

Figure 2: *Attenuation as a result of scattering. This figure was adopted from Fuss et al. [56].*

2.6.4 Beam Hardening Theory

Beam hardening is a phenomenon that occurs in X-ray imaging systems, particularly in Computed Tomography (CT), when a polychromatic (broad energy spectrum) X-ray beam passes through an object [17]. Classical X-ray tubes and linear accelerators typically emit X-rays with a range of energies due to bremsstrahlung radiation, where electrons are decelerated and emit radiation. The degree to which materials attenuate X-rays is energy-dependent, with higher energy photons being attenuated less than lower energy photons. As the X-ray beam travels through a material, the lower energy photons are absorbed more readily than the higher energy photons, resulting in a shift of the beam's energy spectrum [17, 58]. This selective absorption increases the relative proportion of higher energy photons as the beam passes through thicker material, causing the X-ray beam to become "harder," or shifted toward higher energies. This change in the energy spectrum within the material is the core effect of beam hardening [17].

The impact of beam hardening on X-ray imaging is significant, especially when it comes to using the Beer-Lambert law, which assumes a constant attenuation coefficient. For a polychromatic beam, however, the attenuation coefficient varies with the energy of the photons, and the standard law becomes invalid. The total attenuation in such cases must be calculated by integrating over the energy spectrum, considering energy-dependent attenuation coefficients and the initial spectrum of the X-ray beam. To address this, an effective attenuation coefficient (μ_{eff}) is used, which takes into account the material, its thickness, and other factors such as the X-ray setup and detector sensitivity. This coefficient is not a constant material property, but rather a function of the beam energy spectrum and the experimental conditions [17].

Beam hardening also leads to projection errors and artifacts in CT images. The reduced attenuation of higher-energy photons means that the total attenuation is underestimated, especially in dense materials. This discrepancy results in beam hardening artifacts, such as cupping (a decrease in measured density toward the center of a homogeneous object) and streak artifacts (dark or bright bands between dense structures), which reduce the quality of reconstructed images [59].

Implications for BCR Studies

In a water-filled column imaged using a polychromatic X-ray source, beam hardening leads to a characteristic artifact where the reconstructed image appears brighter at the edges and darker in the center as found by multiple studies [60]. This occurs because lower-energy X-ray photons are attenuated more strongly than higher-energy photons as they pass through the material. Near the edges of the column, where the path length through water is short, the beam undergoes minimal spectral shift, and attenuation appears relatively high. However, toward the center, where the beam traverses a longer path, more low-energy photons are absorbed, and the beam becomes more "hardened" with higher-energy photons that are attenuated less. As a result, the reconstructed center appears darker than the periphery, even though the material is

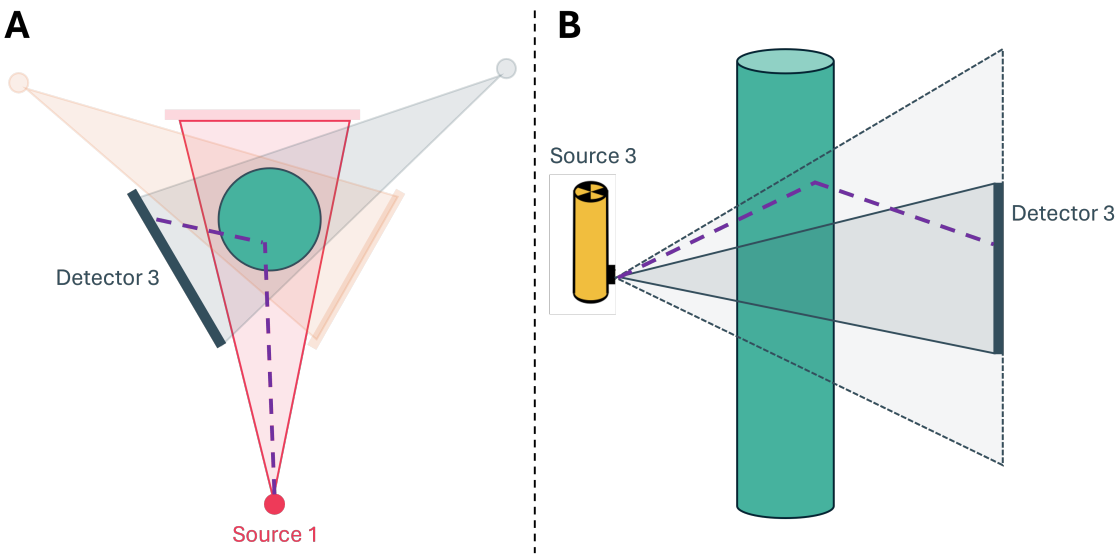

Figure 3: *Examples of cross scattering (A) and forward scattering (B). Figure A shows a schematic top view of the X-ray setup and B shows a schematic side view of the setup. In A, an X-ray (purple line) from source 1 hits detector 3. In figure B, an X-ray from source 3 outside the measurement range of detector 3 hits detector 3. These are two examples of noise caused by scattering for detector 3.*

homogeneous. This cupping artifact, a direct consequence of beam hardening, visually manifests as a radial gradient in grayscale intensity, misrepresenting the true uniformity of the water-filled column [60].

Beam Hardening Corrections

To mitigate beam hardening, several correction techniques are employed. Hardware methods include pre-filtration, which involves placing a thin sheet of metal between the X-ray tube and the object to absorb low-energy photons, and dual-energy X-ray sources, which use two different X-ray energies to compute monochromatic attenuation values. Monoenergetic sources, such as synchrotron beamlines or γ-ray sources, provide a single energy beam that eliminates beam hardening by definition, though they have limitations in terms of sample size and contrast for certain materials [58].

Software methods for beam hardening correction include linearization, where projection data is transformed to a linear relationship using polynomial fitting [58, 61]. Another correction method is iterative reconstruction, which incorporates beam hardening models into the reconstruction algorithm to correct artifacts. Other techniques, such as using consistency conditions or Monte Carlo simulations, are also used to model and correct beam hardening, though they can be computationally intensive [58].

3 Materials and Methods

3.1 Experimental Setup

3.1.1 Bubble Column Setup

The bubble column used in this research was made of polycarbonate and has an inner diameter (D_c) of 19 cm. The column consists of four different parts (see Fig. 4, A, B, C and D). The bottom compartment (A) is the wind-box, where air enters the BCR. The tubing from the mass flow controller was split. Two 12 mm Festo tubes were connected to the splitter and to two openings in the wind-box. The wind-box was connected to the second compartment (Fig. 4, B) of the bubble column. The two parts were separated by a stainless steel sparger plate (Fig. 5, H_0).

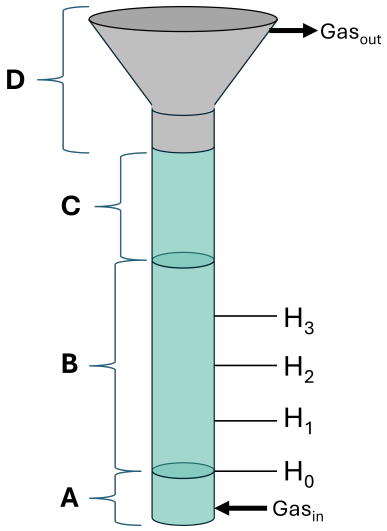

Figure 4: *Schematic overview of the bubble column setup. The BCR consists out of four parts: the wind-box (A) where gas enters the BCR, the main part (A) where different probes and tubing is connected, the top part (C) to extend the height of the bubble column and the cap (D) to risk of overflowing liquid or foam. The sparger plate is located between A and B at H_0. Pressure probes are placed at H_1 (37.5 cm from sparger plate) and H_2 (57.5 cm from sparger plate). An optical fiber probe is placed at H_2. Compounds are added via a syringe atached to the BCR at H_3 (75 cm above sparer plate).*

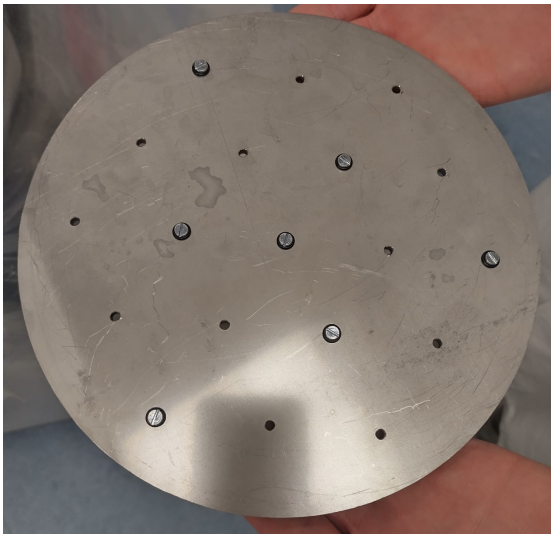

Figure 5: *Image of the sparger plate. The sparger plate has 12 open orifices with a diameter (d_o) of 3 mm. The distance between the orifices (pitch) is 40 mm.*

The main compartment of the BCR (Fig. 4, B) has nine ports to connect tubing or probes to the column. Three ports are located 37.5 cm above the sparger plate (Fig. 4, H_1), three ports are located 57.5 cm above the sparger plate (Fig. 4, H_2) and the upper most ports are located 75 cm above the sparger plate (Fig. 4, H_3). The lower ports are used for a pressure probe and a 12 mm Festo tube with a valve to empty the column. The middle ports are used for a pressure probe and fiber probe. One of the top ports is used to connect a polytetrafluoroethylene (PTFE) tube to a syringe. The column was placed on a rotation table for calibration purposes. The tilt of the column was adjusted to less than 4 mm per meter with 3 stabilizing arms. The offgas was vented through a PVC pipe to a fume hood (see Fig. 4, Gas$_{out}$). The top part of the column (Fig. 4, C) was connected to the main part (Fig. 4, B). This part has a wide metal cap (Fig. 4, D) to reduce the risk of overflowing liquid or foam.

3.1.2 Fiber Probe

A Doppler optical fiber probe was utilized to measure the void fraction and bubble size distribution (BSD) (see Chapter 2.5). The void fraction was measured through continuous measurements at 31250 kHz over a period of 45 seconds. The second type of measurement is the BSD measurement. For BSD measurements, at least 1000 bubble chord lengths were measured

The fiber probe was connected to the column via one of the middle ports (see Fig. 4, H_2). Nine positions from the column wall to the tip of the probe were determined (see Table 1).

Table 1: *Positions of the fiber probe*

Position	Distance from one side (mm)	Distance from column center (mm)	Dimensionless radius (r/R)
1	22	73	0.77
2	42	53	0.56
3	59	36	0.38
4	77	18	0.19
5	96	1	0.01
6	115	20	0.21
7	135	40	0.42
8	153	58	0.61
9	174	79	0.83

3.1.3 Pressure Probes

The pressure probes (Fig. 4, H_1 and H_2) were calibrated with static liquid height (see Eq. 12).

$$P = \rho g h \tag{12}$$

where P is the pressure exerted by the fluid, ρ is the density of the fluid (in this case, water), g is the acceleration due to gravity, and h is the height of the water column above the probe. By systematically varying the height of the water column and recording the corresponding voltage output from the probe, a calibration curve was established. This curve was later used to convert voltage readings into pressure values during the experiments. The pressure measurements were used to determine gas holdup between the the two pressure probes according to Eq. 2.

The pressure probes were not well grounded for the experiments conducted for a system with ... . Therefore, the pressure probe data from does experiments required some extra data analysis. It was found that the pressure fluctuations followed a Gaussian distribution. Before the pressure probes were correctly rounded, there were low voltage signals (noise) influencing the mean holdup measurements. The real data was overlapping with the noise data. Splitting the data into 3 distinct Gaussian distributions resulted in a clean dataset with the noise removed.

3.1.4 X-ray setup

The bubble column was placed in the middle of three continuous X-ray sources and three CMOS detectors arranged in an equilateral triangle (see Fig. 6). The current was determined iteratively by changing the current and comparing the intensity detected on each detector. The voltage and currents used in the experiments are shown in Table 2. The frame-rate of the detector was set to 22 Hz (see Table 2).

Holdup was determined by comparing X-ray images of the operating bubble column with reference images of the empty and water-filled column (no gas). To reduce the impact of random noise in X-ray detection, the empty and full column measurements were averaged over 10 seconds. The dynamic bubble column was imaged over a period of 2 minutes to account for hydrodynamic fluctuations, enabling a more representative time-averaged reconstruction of the flow field. The static system does not have any hydrodynamic fluctuations. Therefore, the measurements time was set to 10 seconds.

	Specification	Notes
X-ray source		
Model	Yxlon Y.TU 160-D06	
Voltage	120 kVp	Maximum source voltage is 150 kVp
Current	0.65, 0.68, 0.75 mA	For source 1, 2 and 3
Detector		
Model	Teledyne Dalsa Xineos 3131	
Resolution	1548x1524 pixels	0.2 mm/pixel
Surface area	307x302 mm	
Framerate	22 Hz	Options between 22 to 200 Hz
Bubble column		
Material	Polycarbonate	
Inner diameter	19 cm	
Outer diameter	20 cm	
Height wind-box	14.8 cm	Including 2.3 cm of bottom part
Height main part	120 cm	
Height top part	50 cm	Excluding metal cap
Sparger plate		
Geometry	Circular with holes in hexagonal grid pattern	12 open holes, 7 closed hole
Thickness	5 mm	
Type	Stainless steel sieve plate	
Nuts	Praxis, Sencys RVS INOX M3x16mm	With rubber seal
Fiber probe		
Brand	A2 Photonic Sensors	
Model	M2 Bubbly Flow Analyzer	
Size range	From 100 µm (no upper limit)	
Velocity range	0.01 to 80 m/s	
Pressure probes		
Model	TDX 716-900	From TC Direct
Accuracy	0.5% F.S	
Range	0-1 bar	
Output	0-10 V	
Distance to sparger plate		
Mass flow controller		
Brand	Bronkhorst	
Capacity	250 ln/min	

Table 2: *Specifications of the equipment and instrumentation used in the experimental setup for gas holdup distribution measurements in a bubble column.*

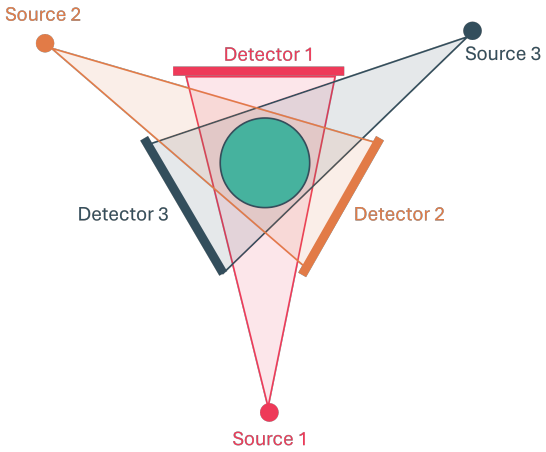

Figure 6: *X-ray setup used in experiments.*

3.1.5 Liquid Compositions

Hydrodynamic effects of the addition of the following compounds to a tap water-filled BCR were tested in the lab: ethanol, 1-propanol, *iso*-propanol, 1-butanol, acetic acid, and lactic acid. To capture the same range of effects for the different compounds of interest, the concentrations were scaled. Keitel and Onken [34] found relations for different molecule types between the number of carbon atoms (n_c) and the limiting concentration (c_t). The limiting concentration is the concentration above which the coalescence becomes significant. The ideal maximum concentration found after scaling the concentrations with the relation by Keitel and Onken [34] can be found in Appendix B, Table 8. Ideally, the concentration is increased exponentially since the most dramatic effects are of concentration on the hydrodynamics is expected for relative low concentrations [1]. Therefore, more data-points are preferred for low concentrations.

Even though the ideal maximum concentration would possibly reveal the most important hydrodynamic changes, it was not possible to test in our set-up due to formation of foam. To test in heterogeneous bubble regime, the superficial gas velocity must be at least 0.05 m/s. The ideal maximum concentration of 1-propanol in water has the lowest surface tension [62, 63]. Therefore, it was expected that this compound would create the most foam in our system. It was found that the maximum reachable concentration at a superficial gas velocity of 0.05 m/s was 0.36 mol/l. Therefore, the maximum concentrations were scaled again to accommodate for foaming (Appendix B, Table 8). The actual maximum target concentrations were different due to evaporation and drainage via the sparger plate during the experiments.

Based on the target concentration an added amount of compound per concentration was calculated. The concentrations at which the experiments were conducted are shown in Appendix C. The concentrations were determined with high-performance liquid chromatography (HPLC).

3.1.6 Properties

The cocentration of the samples was determined using a Vanquish Core HPLC [64]. The surface tension was dynamically determined using a bubble pressure tensiometer from Krüss [65]. The density and viscosity were determined using a Rolling-ball viscometer: Lovis 2000 M/ME from Anton Paar. The properties of the chemical compositions studied in this research are tabulated in Appendix C.

3.2 Experimental Procedure

3.2.1 Scatter Characterization

To characterize X-ray scatter for each detector, each individual detector signal was quantified over 30 seconds, with the X-ray source inactive, and the other two sources active (see Fig. 6).

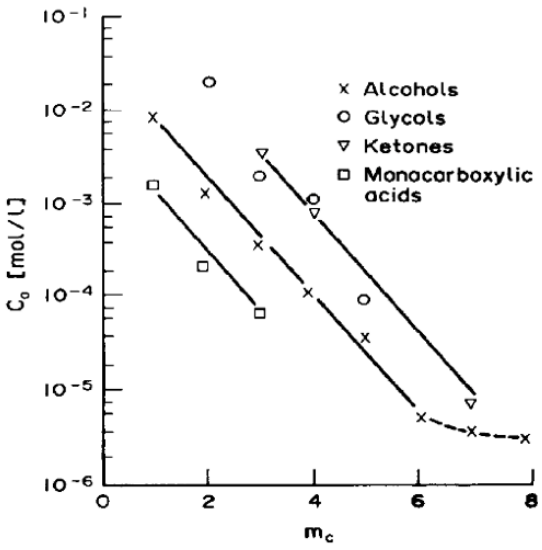

Figure 7: *Relations between the number of carbon atoms (m_c) per molecule type and coalescence limiting concentration (c_0). This figure was adopted from Keitel and Onken [34].*

Scatter characterization is performed for water and for 1-propanol at a concentration of approximately 20 g/l. The holdup was increased by increasing the volumetric gas-flow. The measurements were set to 30 seconds (662 frames). This measurement time is shorter than for the actual measurements of the dynamic system. The scattering is determined for all three detectors for a wide range of hold-ups.

The scattering was also determined for the other compounds. Since it was found that holdup did not significantly influence scattering, the scattering was only determined for a static system for every concentration. The measurement time was set to 10 seconds to determine an acceptable mean intensity for every pixel (see Appendix D.2).

3.2.2 Measurements Concentration Series

Each experimental day was dedicated to testing a single compound. The liquid height was set to 100 cm above the sparger plate. This results in a H/D ratio of more than 5. Literature found that hydrodynamic parameters are translatable between scales for systems with an H/D ratio>5 and D>15 cm [31, 66, 67]. A sample was taken to quantify contamination from previous experiments. The compounds were added to the BCR via a syringe. After addition, the liquid level was adjusted back to 100 cm with tap water. The compound was mixed for at least one minute at a superficial gas velocity of 0.05 m/s.

X-ray and pressure measurements were first conducted without gas flow, including scatter characterization. During all X-ray measurements, pressure probe signals were recorded simultaneously. Subsequently, gas was introduced at 80 L/min. Once foam stabilized, X-ray and pressure data were collected for 2 minutes. This averaging time provides a reliable mean pressure (see Appendix D.1). Void fraction was then measured at positions 1, 3, 5, 7, and 9 (1), and BSD was measured at these positions for the highest concentration of each compound. At the highest concentration, void fraction was also recorded at all nine positions. After fiber probe measurements, liquid height was noted and a sample was taken. The concentration was then increased for the next measurement cycle. An overview of the workflow is shown in Fig. 8.

3.3 Correlations

3.3.1 Correlations Global Gas Holdup

Many correlations for gas holdup in bubble columns exist. The current study investigates the correlations for global gas holdup from Hughmark [68] (see Eq. 13), Kumar et al. [69] (see Eq. 14), Hikita and Kikukawa [70] (see Eq. 15), Hikita et al. [71] (see Eq. 16), Reilly et al. [72] (see Eq. 17), Bekish et al. [73] (see

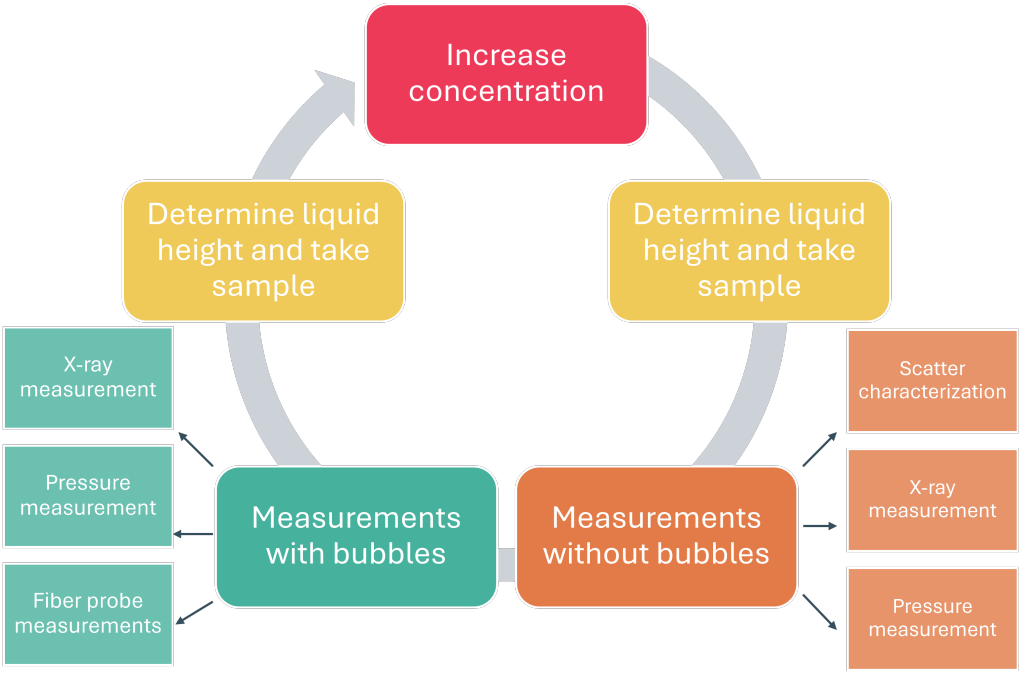

Figure 8: *Workflow of measurements for the concentration series. This workflow was used for ethanol, 1-propanol, iso-propanol, butanol, acetic acid and lactic acid. The measurements with bubbles were conducted at a volumetric gasflow of 80 l/min which corresponds in this setup to a superficial gas velocity of 0.05 m/s.*

Eq. 18), Anastasiou et al. [74] (see Eq. 19) and Azizi et al. [75] (see Eq. 23). Many of the correlations are of the general form aU_g^n. Moshtari et al. [76] states that the fitting parameter n tells us something about the flow regime for which the correlation is applicable. Generally $0.7 < n < 1.$ is used for the homogeneous regime and $0.4 < n < 0.7$ is used for the heterogeneous regime [76].

Hughmark (1967)

The correlation from Hughmark [68] is an empirical formulation developed from a wide experimental database covering various gas–liquid systems and column diameters. The correlation is stated to be a function of the superficial gas velocity and is primarily applicable to the bubbling regime in co-current systems.

$$\bar{\epsilon} = U_g \cdot \mathbf{0.3038} \left(\frac{62.4}{\rho_l \cdot \mathbf{16.0185}} \frac{72}{\sigma \cdot \mathbf{0.001}} \right)^{1/3} \tag{13}$$

The numbers in bold in Eq. 13 are added to the equation to convert to the metric system.

Kumar et al. 1976

Kumar at al. [77] published a correlation suitable for a wide variety of systems (Eq. 14), including the dispersed (homogeneous) flow regime and heterogeneous flow regime. They used data from different process conditions with superficial gas velocities up to 15 cm/s. They found an average deviation of ±8.34% [77].

$$\bar{\epsilon}_g = 0.728U - 00.485U^2 + 0.0975U^3 \tag{14}$$

with

$$U = U_g \left(\frac{\rho_l^2}{\sigma} \left(\rho_l - \rho_g \right) g \right)^{1/4}$$

Hikita and Kikukawa (1974)
The correlation from Hikita and Kikuwaka (Eq. 15) [70] was validated in heterogeneous flow regime. Their correlation includes some physical properties of the system.

$$\bar{\epsilon} = 0.505 U_g^{0.47} \left(\frac{0.072}{\sigma}\right)^{2/3} \left(\frac{0.001}{\eta_l}\right)^{0.05} \tag{15}$$

Hikita et al. (1980)
Hikita et al. [71] published a correlation applicable for turbulent systems (Eq. 16) with superficial gas velocities ranging from 0.042 to 0.38 m/s [72]. The correlation is for pure liquids or non-electrolyte solutions.

$$\bar{\epsilon} = 0.672 U_g^{0.574} \rho_l^{0.069} \rho_g^{0.062} \sigma^{-0.185} \eta_l^{-0.053} \eta_g^{0.107} g^{-0.131} \tag{16}$$

Reilly et al. (1986)
The correlation presented by Reilly et al. [72] was correlated statistically for the transition and the turbulent region. The authors aimed to obtain a generalized correlation for the heterogeneous flow region (Eq. 17).

$$\bar{\epsilon}_g = 296 U_g^{0.44} \rho_l^{-0.98} \sigma^{-0.16} \rho_g^{0.19} + 0.009 \tag{17}$$

Behkish et al. (2006)
Behkish et al. [73] proposed a generalized correlation for total gas holdup (Eq. 18) derived from an extensive data set including various gas–liquid and gas–liquid–solid systems. This model incorporates multiple operating and design parameters including pressure, temperature, superficial gas velocity, column diameter, solid loading, and sparger type.

$$\overline{\epsilon_g} = 4.94{\times}10^{-3} \left(\frac{\rho_l^{0.415} \rho_g^{0.177}}{\eta_l^{0.174} \sigma^{0.27}}\right) U_g^{0.553} \left(\frac{P_T}{P_T - P_S}\right) \left(\frac{D}{D+1}\right)^{-0.117} \Gamma^{0.053} \exp[-2.231 C_V - 0.157(\rho_P d_P) - 0.242 X_W] \tag{18}$$

with

$$\Gamma = (K_d N_o d_o^{\epsilon}),$$
$$\xi = \frac{100 N d_o^2}{D^2}$$

Γ represents the effect of the sparger plate. K_d is the distributor coefficient, N_o is the number of orifices in the sparger, and d_o is the diameter of the orifice. For the perforated plate in the current study, K_d is 1.364 and α is 0.303. The last term in Eq. 18 represent the effect of biomass. The volumetric solid concentration (C_V) is 0, since there are no solids. In the case of bubble column reactors ρ_P, and d_P are also zero. The weight fraction of the primary liquid in the mixture (X_W) was set to 1, since the BCR is almost entirely filled with water. An estimation of the vapor pressure (P_S), and total pressure (P_T) are $2 \cdot 10^{-3}$ MPa and 0.103 MPa, respectively.

Anastasiou et al. (2010)
Anastasiou et al. [74] developed a set of gas holdup correlations focused on systems employing porous spargers and surfactants. For non-ionic surfactant systems, they provided a specific correlation in dimensionless form (Eq. 19). It was derived from experimental data in the pseudo-homogeneous regime and accounts for the effects of surfactant type and concentration. Constants for this equation are system-dependent, and the reported version applies to non-ionic surfactant systems, showing deviations below 20% from experimental data.

$$\bar{\epsilon} = 0.0034 \left(Fr^{0.6} Ar^{0.15} \text{Eö}^{1.85} \left(\frac{d_s}{d_c} \right)^{0.2} \left(\frac{d_p}{d_s} \right)^{-0.3} \right)^{0.52} \tag{19}$$

This correlation uses the Froude number (Fr) (Eq. 20, similar to Eq. 35), the Eötvos (Bond) number (Eö) (Eq. 21), the Archimedes (Galileo) number (Ar) (Eq. 22), the ratio of the sparger diameter over the column diameter $\frac{d_s}{d_c}$ and the ratio of the mean pore diameter over the diameter of the sparger $\frac{d_p}{d_s}$.

$$Fr = \frac{U_g^2}{d_c g} \tag{20}$$

$$\text{Eö} = \frac{d_c^2 \rho_l g}{\sigma} \tag{21}$$

$$Ar = \frac{d_c^3 \rho_l g}{\eta_l^2} \tag{22}$$

Azizi et al. (2019) Azizi et al. [75] proposed a coupled model for total gas holdup in which the mean bubble diameter serves as the characteristic length scale in the dimensionless formulation:

$$\epsilon_g = 1.1 \cdot 10^{-3} Re_{d_m}^{1.12} Eo_{d_m}^{-0.89} \tag{23}$$

The mean bubble diameter is predicted through a separate correlation that incorporates sparger type and operating conditions. The correlation shows good agreement with experimental data in both the homogeneous and heterogeneous regime but its accuracy is dependent on the quality of bubble size estimation.

3.3.2 Correlations Holdup Distribution

The number of correlations for gas holdup distribution are limited in literature [75]. Due to the absence of universally applicable fundamental equations for predicting radial holdup profiles, empirical models remain essential. In this work, four different radial gas holdup correlations were selected. These correlations were implemented and evaluated against experimental data obtained in a lab-scale air–water bubble column to assess their accuracy and applicability.

Ueyama and Miyauchi (1979)
The correlation from Ueyama and Miyauchi [78] is an early empirical formulation based on extensive experimental observations. The radial profile was assumed to follow Eq. 24.

$$\epsilon_g(\xi) = \tilde{\epsilon_g} \left(\frac{n+2}{n} \right) (1 - \xi^n) \tag{24}$$

$$\text{with } n \approx 2$$

This model was used qualitatively, as no explicit correlation for c or n based on operating conditions was provided. Several values of n (typically between 2 and 8) were tested based on literature ranges. In the current study n was chosen to be 2.5 to better fit the results. $\tilde{\epsilon}_g$ is the radial chordal average gas holdup.

Wu et al. (2001)
This model (Eq. 25) introduced a normalized formulation that accounts for variations in the holdup profile shape through correlations of n and c with standard dimensionless groups.

$$\epsilon_g(\xi) = \bar{\epsilon} \left(\frac{n+2}{n+2-2c} \right) (1 - c\xi^n) \tag{25}$$

with

$$n = 2.180 \cdot 10^3 \left(\frac{D_c U_g(\rho_l - \rho_g)}{\eta_l}\right)^{-0.598} \left(\frac{U_g^2}{gD_c}\right)^{0.146} \left(\frac{g\eta_l^4}{(\rho_l - \rho_g)\sigma^3}\right),$$

$$c = 4.32 \cdot 10^{-2} \left(\frac{D_c U_g(\rho_l - \rho_g)}{\eta_l}\right)^{0.2492}.$$

Where ξ is the non-dimensional radius, D_c is the diameter of the BCR, g is the gravitational constant.

Schweitzer et al. (2001)

This model from Schweitzer et al. [2] is the simplest model tested in the current study (Eq. 26).

$$\epsilon(\xi) = \overline{\epsilon}\left(-1.638\left(\xi^6 - 1\right) + 1.228\left(\xi^4 - 1\right) - 0.939\left(\xi^2 - 1\right)\right) \tag{26}$$

The fixed coefficients (from literature) define a universal profile shape. This model assumes that the normalized radial profile is independent of operating conditions and is intended to reflect typical distributions observed in both gas-liquid and slurry bubble columns [2].

Azizi et al. (2019)

The correlation from Azizi et al. [75] follows a "coupled" approach where the shape parameters are linked to the mean bubble diameter and associated dimensionless groups (Eq. 27).

$$\epsilon_g(\xi) = \epsilon_{g,max}(1 - c_\epsilon \xi^{n_\epsilon}) \tag{27}$$

The maximum gas holdup is defines as (28)

$$\epsilon_{g,max} = \frac{(n_\epsilon + 2)\,\overline{\epsilon_g}}{(n_\epsilon + 2 - c_\epsilon)} \tag{29}$$

with

$$c_\epsilon = 0.65 Re_{\overline{d}_m}^{-0.30} \text{Eö}_{\overline{d}_m}^{0.68},$$

$$n_\epsilon = 0.23 Re_{\overline{d}_m}^{-0.39} \text{Eö}_{\overline{d}_m}^{-0.18}$$

Where $Re_{\overline{d}_m}$ and $\text{Eö}_{\overline{d}_m}$ are the Reynolds and Eötvös numbers based on the mean bubble diameter (see Eq. 30 and Eq. 31).

$$Re_{\overline{d}_m} = \frac{\rho_l U_g \overline{d}_m}{\eta_l} \tag{30}$$

$$\text{Eö}_{\overline{d}_m} = \frac{\rho_l g \overline{d}_m^2}{\sigma} \tag{31}$$

The mean bubble diameter ($\overline{d}_m$) was determined using BSD measurements with the optical fiber probe. The Sauter diameter (see Eq. 7) was chosen as approximation.

3.3.3 Correlation Marangoni number and Global Gas Holdup

The correlation proposed by Wang et al. (see Eq. 33) incorporates several dimensionless numbers that characterize hydrodynamic phenomena [1]. These include the Froude number (Fr), Bond number (Bo), Galilei number (Ga), Marangoni number (Ma), and Péclet number (Pe). Additionally, the dimensionless capillary number (Ca) is used in the calculation of Ma (see Eq. 4).

Wang et al. did not document all values of the dimensional numbers. Therefore, validating their work is challenging. To validate validate and extend their work, correlating the Ma number with $\overline{\epsilon}$, three methods were applied :

- Method 1 implements calculations of the dimensionless numbers, differing from the original methodology used by Wang et al (Table 3). These computed values are then used to fit the parameters in Eq. 32.
- Method 2 adopts the same computational approach for the dimensionless numbers as Method 1 (Table 3, "This Study"), but applies the original fitting parameters reported by Wang et al. Eq. 33 in the correlation.
- Method 3 attempts to replicate the calculation methods of Wang et al. for the dimensionless numbers and uses their full correlation as published (see Eq. 33).

Concretely, method 1 and 2 applies equations for Ca (Eq. 36), Ga (Eq. 37) and Bo (Eq. 38) that are different than the equations used by Wang et al. [1]. The differences are summarized in Table 3.

$$\bar{\epsilon} = aFr^b Bo^c Ga^d (\frac{\rho_g}{\rho_l})^e (1 + 3000 Ma^f Pe^{g)})^h \tag{32}$$

$$\bar{\epsilon} = 1.97 Fr^{0.78} Bo^{0.013} Ga^{0.010} (\frac{\rho_g}{\rho_l})^{0.21} (1 + 3000 Ma^{2.0} Pe^{-4.2)})^{4.6} \tag{33}$$

$$Pe = \frac{R_{eq} V}{D_l} \tag{34}$$

$$Fr = \frac{U_g}{\sqrt{g D_b}} \tag{35}$$

$$Ca = \frac{\eta_l u_l}{\sigma} \tag{36}$$

$$Ga = \frac{\rho_l \sqrt{g D_b} D_b}{\eta_l} \tag{37}$$

$$Bo = \frac{\Delta \rho g D_b^2}{\sigma} \tag{38}$$

Table 3: *Dimensionless numbers used in this study compared to dimensionless numbers used by Wang et al. [1]*

Abbrev.	Wang et al.	This Study	Eq.
Ca	$\frac{\eta_b V}{g}$	$\frac{\eta_l u}{\sigma}$	Eq. 36
Ga	$\frac{\rho_l^2 g D_b^3}{\eta_l^2}$	$\frac{\rho_l \sqrt{g D_b} D_b}{\eta_l}$	Eq. 37
Bo	$\frac{\rho_l g D_b^2}{\sigma}$	$\frac{\Delta \rho g D_b^2}{\sigma}$	Eq. 38

Wang et al. [1] used the superficial gas velocity of the riser (U_{gr}) in their methodology for an ILAR. The current study used U_g instead. Calculating U_g from U_{gr} is possible using Eq. 39. Where A_r is the area of the riser and A_d is the ares of the downcomer. However, the ratio between A_r and A_d is not known for the BCR in the current study and the ratio used by Wang et al. [1] is not applicable due to the difference in reactor type.

$$U_g = \frac{U_{gr} A_r}{A_r A_d} \tag{39}$$

3.4 X-ray Tomography

X-ray tomography was used to investigate local gas holdup in the BCR. SIRT was used to make reconstructions from the 2D projections (see Chapter 2.6.2). First, the geometry of the system was determined by applying a calibration as developed by Graas et al. [53].

The beam hardening (see Chapter 2.6.4) correction required information about the distance an X-ray traveled through the BCR. Based on the geometry found by the calibration this path length was calculated. The methods to correct the X-ray images for scattering and beam hardening are explained in the result section (see Chapter 5), since the goal of this thesis is to improve the methodology of X-ray tomography for BCR.

3.4.1 Calibration

Accurate tomographic reconstruction requires a precise geometric model of the X-ray imaging system, including the 3D positions of the X-ray sources and detectors, as well as the orientation of each detector plane. To achieve this, a calibration method from Graas et al. [53] was applied.

The bubble column was placed at the center of the setup and imaged at multiple angles using a motorized rotation table. Projection images were captured from all three detectors for each rotation angle. The outside of the column walls were marked with needles and pins. These features were manually annotated across several projection angles to establish 2D projection coordinates corresponding to known geometric elements of the column. These marks were used as reference points for calibration.

A mathematical model was then used to match the 2D positions of these features in the images to their 3D positions in space, based on how X-rays travel through the setup. This was done using a least-squares optimization, which automatically adjusted the estimated positions of the X-ray sources and detectors to best fit the marked image points. This optimization also included the orientation of the detector planes. A method called the Levenberg–Marquardt algorithm was used, which is commonly used for this type of problem.

Since the system does not know real-world distances yet, the result of the calibration is only correct up to a scaling factor. To fix the scale, the known diameter of the bubble column was used. A reconstruction of the column after a full rotation resulted in a high-resolution reconstruction.

This calibration approach is efficient and accurate. It avoids the need for precise physical measurements of the detector and source positions and significantly improves the quality of the final 3D reconstructions.

3.4.2 X-ray Path-length Through Column

Beam hardening causes the attenuation of X-rays to become non-linear when plotting the logarithm of intensity versus the distance traveled through the material. This occurs because lower-energy photons are absorbed more readily than higher-energy ones, leading to a deviation from the ideal exponential attenuation expected under the Beer-Lambert law (see Chapter 2.6.4). So, the quantification and correction of beam hardening requires to distance of an X-ray through the BCR. The calculation for the distance an X-ray beam travels through the column is explained in this section.

The calibration of the X-ray set-up, developed by Graas et al. [53], results in the coordinates of the source (S_X, S_Y, S_Z) and the middle of the detector (D_X, D_Y, D_Z). Besides it results in two vectors for every detector: u is the vector from detector pixel (0,0) to (0,1). v is the vector from detector pixel (0,0) to (1,0). The height and width of the pixels are 0.0198 cm. The detector height and width are 30.2 and 30.7 cm, respectively.

The pixels of the detector are indexed in a two-dimensional arranged in 1524 (N_r) rows and 1548 (N_c) columns. The center of the detector is positioned at known coordinates: $(D_X,\ D_Y,\ D_Z)$

Each pixel is indexed by two integers. i is the row index, which describes the vertical position of the pixel and j is the column index, which describes the horizontal position of the pixel.

Since the middle of the detector is set as the reference point $(i, j) = (0, 0)$, the row and column indices range symmetrically around zero:

$$i \in \left[-\frac{N_r}{2}, \frac{N_r}{2}\right], \quad j \in \left[-\frac{N_c}{2}, \frac{N_c}{2}\right]$$

where:

- $i = -\frac{N_r}{2}$ corresponds to the topmost row, and $i = \frac{N_r}{2}$ corresponds to the bottommost row.
- $j = -\frac{N_c}{2}$ corresponds to the leftmost column, and $j = \frac{N_c}{2}$ corresponds to the rightmost column.

The detector's pixel arrangement is defined by two unit vectors:

- The horizontal unit vector $\mathbf{u}$ describes the direction and spacing between adjacent pixels along a single row:
$$\mathbf{u} = (u_X, u_Y, u_Z)$$
- The vertical unit vector $\mathbf{v}$ describes the direction and spacing between adjacent pixels along a single column:
$$\mathbf{v} = (v_X, v_Y, v_Z)$$

These vectors account for the detector's orientation in 3D space and define the distance between adjacent pixels. The vectors allow to determine the 3D coordinates of the pixels from the pixel indices (i, j). Using the detector center as the reference point, the 3D coordinates (x, y, z) of a pixel at position (i, j) are computed as:

$$x(i,j) = D_X + j \cdot u_X + i \cdot v_X$$

$$y(i,j) = D_Y + j \cdot u_Y + i \cdot v_Y$$

$$z(i,j) = D_Z + j \cdot u_Z + i \cdot v_Z$$

This formulation results in a complete 3D representation in Cartesian coordinates for the whole system.

To calculate the distance that an X-ray beam travels through the BCR, we model the beam as a straight line from the source to a pixel on the detector. It is assumed that the BC is aligned along the z-axis and centered at the origin, with radius r.

Since the coordinates of the detector pixels and the coordinates of the source are known, we are able to define the direction vector $\mathbf{d} = (a, b, c)$, where:

$$a = x - S_x, \quad b = y - S_y, \quad c = z - S_z$$

The parametric form of the X-ray beam is then given by:

$$\mathbf{r}(t) = \mathbf{S} + t\mathbf{d} = (S_x + at,\ S_y + bt,\ S_z + ct)$$

So, the X-ray beam can be expressed as three linear equation for x, y, z:

$$x(t) = S_x + at$$
$$y(t) = S_y + bt$$
$$z(t) = S_z + ct$$

The BCR is modeled as an infinite circular cylinder centered on the z-axis with radius r. The equation of the cylinder is:

$$x^2 + y^2 = r^2$$

To find the intersection points of the X-ray with the BC, we substitute the parametric equations for $x(t)$ and $y(t)$ into the cylinder equation:

$$(S_x + at)^2 + (S_y + bt)^2 = r^2$$

Expanding and simplifying gives a quadratic equation in t:

$$At^2 + Bt + C = 0$$

where

$$A = a^2 + b^2$$

$$B = 2(aS_x + bS_y)$$

$$C = S_x^2 + S_y^2 - r^2$$

The solutions to the quadratic equation are given by the formula:

$$t_{1,2} = \frac{-B \pm \sqrt{B^2 - 4AC}}{2A}$$

The values t_1 and t_2 correspond to the entry and exit points of the X-ray beam through the cylinder. These are substituted back into the parametric equation to obtain the coordinates of the two intersection points $\mathbf{A}$ and $\mathbf{B}$:

$$\mathbf{A} = \mathbf{r}(t_1), \quad \mathbf{B} = \mathbf{r}(t_2)$$

The path length d of the X-ray through the cylinder is the Euclidean distance between points $\mathbf{A}$ and $\mathbf{B}$:

$$d = \|\mathbf{B} - \mathbf{A}\| = \sqrt{(x_B - x_A)^2 + (y_B - y_A)^2 + (z_B - z_A)^2}$$

If the discriminant $\Delta = B^2 - 4AC$ is negative, then the ray does not intersect the cylinder and $d = 0$ for that beam.

4 Results: Assessment of Gas Holdup Correlations in Bubble Column Reactors

4.1 Correlating Marangoni Effect with Holdup

Wang et al. [1] showed the correlation between the Marangoni effect and gas holdup in an internal-loop airlift reactor (ILAR) (Eq. 33). Even though the given correlation is very useful for the system they studied, it does not apply for all other gas-liquid systems. They measured the gas holdup in a system with water and ethanol in an ILAR. They measured the holdup at a superficial gas velocity similar to the system in the current study (5 cm/s). The pressure in the system of tested by Wang et al. was higher (1.5 bar) compared to the system tested in this study (1 bar). Their gas holdup results are different compared to the system investigated in the current study (see Fig. 9). As expected, the gas holdup is lower in the ILAR than in the BCR results, even though the system in [1] operates at higher pressure, which could also contribute to reduced holdup due to increased gas density. However, the dominant factor appears to be the ILAR design, which includes internal structures that promote faster bubble rise and more frequent coalescence, resulting in less gas retention within the liquid [79].

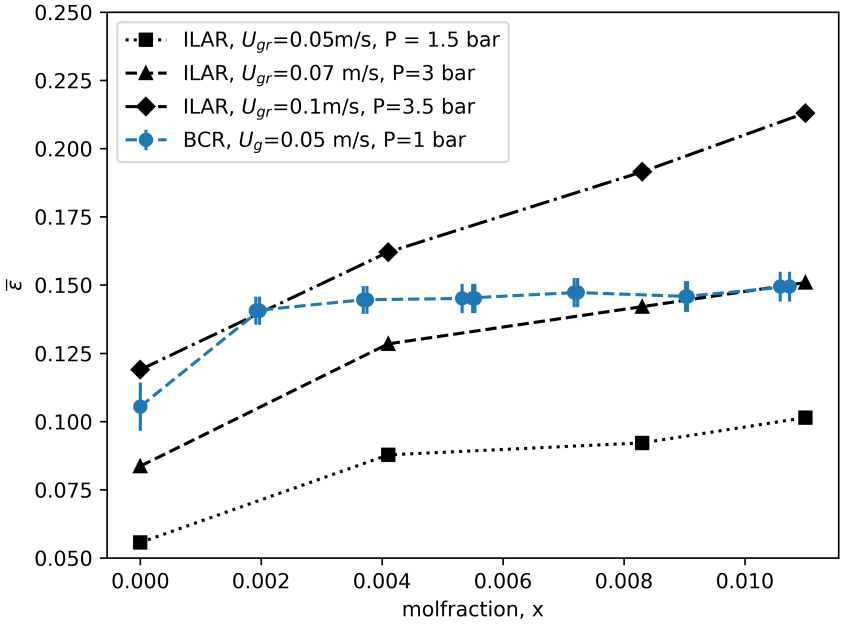

Figure 9: *Comparison of the global gas holdup of a water-ethanol system between Wang et al. (2023) [1] and this study. The data from Wang et al. comes from experiments in an ILAR at a pressure of 1.5 bar. This study focused on a BCR at 1 bar.*

The Marangoni effect number for gas holdup $(1+3000Ma^{2.0}Pe^{-4.2})^{4.6})$ was calculated to validate the correlation by Wang et al. [1] for BCRs. This is a combination of the Ma en Pe number that correlates with bubble coalescence time [1]. With the given documentation of their study, the Marangoni effect number was calculated for the current study. The Pe number (Eq. 34) is calculated with the radius of the bubbles (R_{eq}), the approach velocity (V) and the diffusion coefficient (D_l). In this study, approach velocities of around 20 cm/s were observed (see Appendix E). However, only gentle collisions of bubbles with an approach velocity of 1 mm/s were considered [1]. The bubble radius used by Wang et al. is about 0.5 mm. However, this study found a d_{32} of around 4 mm, equal to an R_{eq} of around 2 mm. Although the bubble radius likely varies between experiments, BSD was not measured for all samples. As a result, a constant radius of 2 mm was assumed. Consequently, the Pe number is treated as constant for all experiments involving the same compound. For the ethanol experiments, $1/Pe$ is calculated and compared with the $1/Pe$ number

reported by Wang et al. (see Appendix F Fig. 27). The impact of using a different bubble radius is also shown in Appendix F Fig. 27. The different Pe numbers also result in different Marangoni effect numbers (see Fig. 10).

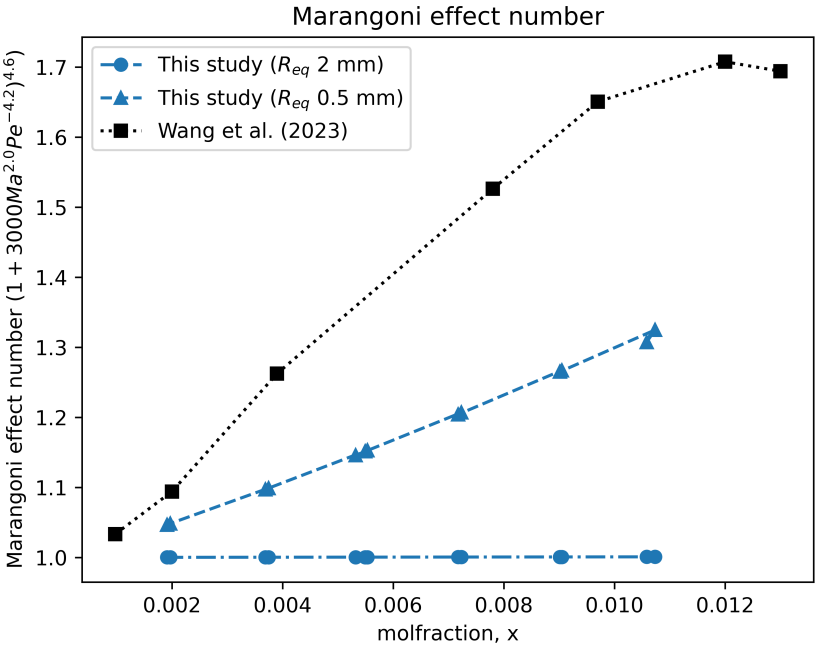

Figure 10: *The Marangoni effect number for a water-ethanol system. The results of this study for bubbles with a radius of 2 mm and 0.5 mm are compared to literature data by Wang et al. [1].*

The dimensionless capillary number (Ca) is the ratio between viscous and interfacial stress (see Eq. 36). Wang et al. used the viscosity of the bubble (μ_b) and the approach velocity (V) (see Table 3). However, the viscosity and velocity of the liquid is more common to use (see Eq. 36) [80, 81]. The surface tension (σ) was measured for all the samples and plotted against the natural logarithm of the concentration (see Appendix G, Fig. 28). The measured surface tension of ethanol was compared with literature (see Appendix G, Fig. 29). The gradient ($\frac{d\sigma}{dln(x)}$) at the different data points were used to calculate the surface excess (Γ_{eq}). The surface excess was calculated using Gibbs isotherm (see Eq. 40). This methodology was verified by comparing the surface excess with literature data for the ethanol-water mixture. It was found that the surface excess is in line with literature data (see Appendix H, Fig. 30).

$$\Gamma_{eq} = -\frac{1}{RT}\frac{d\sigma}{dln(x)} \tag{40}$$

The surface tension (σ) and surface excess (Γ) are plotted (see Fig. 11) to determine the gradient ($\frac{d\sigma}{d\Gamma}$) required to calculate the Ma number (see Eq. 4).

The Marangoni numbers calculated for ethanol and water samples in this study show some discrepancies compared to those reported by Wang et al. [1] (see Fig. 12). These differences are primarily attributed to variations in the input parameters and calculation methods used. The Ma number calculated in this study used the equations described in Chapter 3.3.3, Method 1. While the same general formula was used to compute the Marangoni number (see Eq. 4), Wang et al. applied different approaches for determining the Ca, Ga and Bo numbers (Chapter 3.3.3, Method 3). Moreover, the lack of detailed documentation in their methodology further limits the ability to perform a direct comparison.

The dependence of the Ma number on the global gas holdup is shown in Fig. 13. The figure shows that an increased Ma number results in a higher global gas holdup. The correlation of Wang et al. (see Eq. 32) is fitted though this data to find new fitting parameters (see Section 3.3.3, Method 1). The correlation

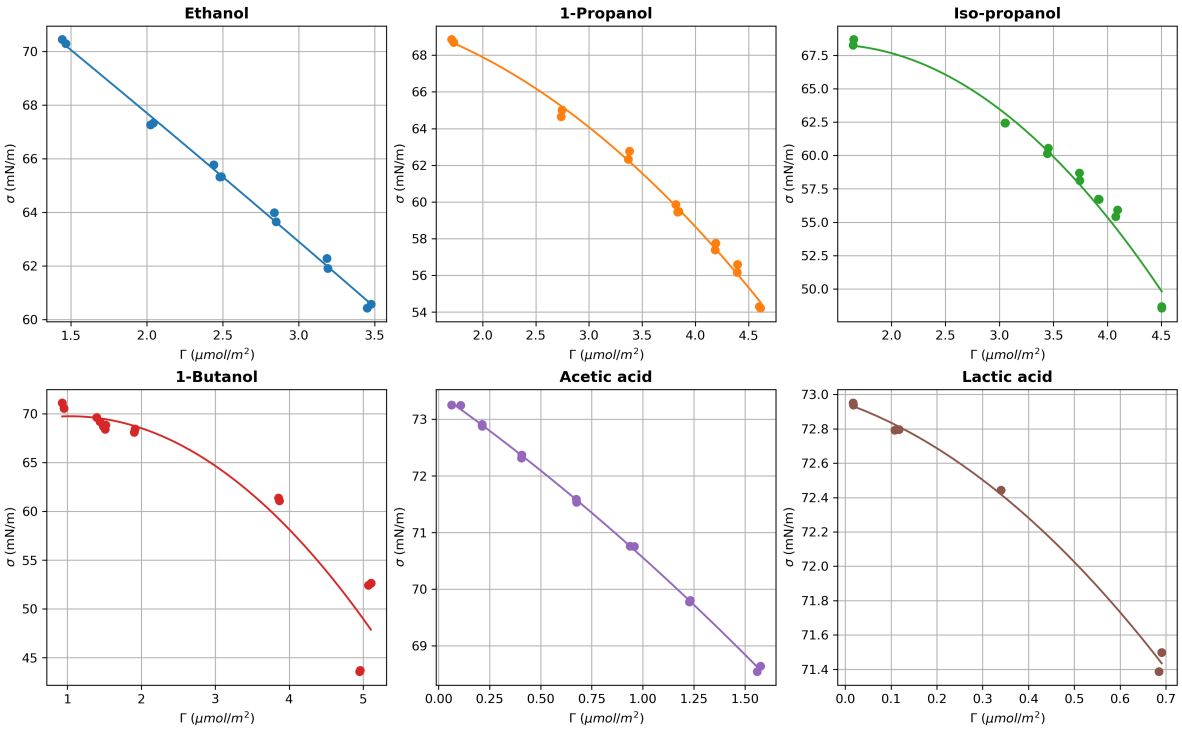

Figure 11: *Surface tension measurements for different values of surface excess. A parabolic equation is fitted through the data. The measurements are done for ethanol, n-propanol, iso-proanol, n-butanol, acetic acid and lactic acid.*

that fits the data from this study is given in Eq. 41. The predicted global holdup by Eq. 41 is for 90% of the samples within the 10% error range from the measured global gas holdup (see Fig. 14 and Table 4).

Surprisingly, Method 2 (see Section 3.3.3) also results in a good prediction of the global gas holdup. The methodology of calculating the dimensionless numbers in the holdup correlation are different than done by Wang et al. Still, the correlation from Wang et al. predicts 92% of the holdup values within a 10% error margin from the experimental data. Method 3 (see Section 3.3.3) results in an under-prediction of the gas holdup compared to the measured holdup. This is explained by the different process investigated. The method from Wang et al. was developed for an ILAR which results in a lower gas holdup compared to BCRs (see Fig. 9).

$$\bar{\epsilon} = 1.97 Fr^{0.77} Bo^{0.232} Ga^{-0.095} \left(\frac{\rho_g}{\rho_l}\right)^{0.17} \left(1 + 3000 Ma^{2.04} Pe^{-4.17)}\right)^{4.60} \tag{41}$$

Table 4: *Statistical comparison between the methods shown in Fig. 14. The table shows the mean absolute error (MAE), the root mean squared error (RMSE), the mean absolute percentage error (MAPE), and the percentage of data points within a 10% and 20% error margin from the experimental data.*

Model	MAE	RMSE	MAPE (%)	% within ±10%	% within ±20%
Method 1	0.006	0.008	4.124	92	100
Method 2	0.007	0.009	4.953	87	100
Method 3	0.054	0.055	37.357	0	0

With different methodology of calculating the dimensionless numbers, the correlation of Wang et al. (Eq. 33) predicts the global gas holdup accurate for the system studied in this research. Ideally, the calculation of dimensionless numbers are the same for different systems. The difference in process conditions

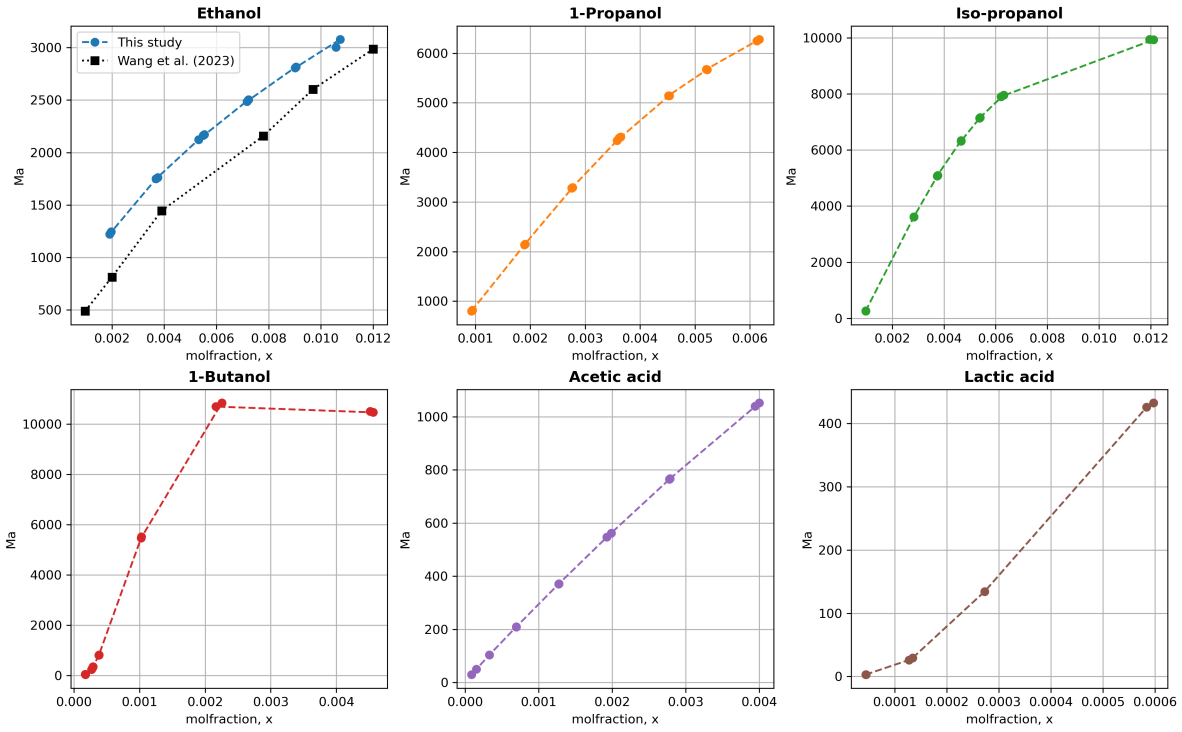

Figure 12: *The influence of alcohols and acids on the Marangoni number. The measurements are done for ethanol, n-propanol, iso-proanol, n-butanol, acetic acid, and lactic acid.*

should be embedded in the correlation or separate correlation should be used. So, one clear method to calculate input values for a certain correlation is favored.

4.2 Comparison of Global Gas Holdup Correlation

Different correlations predicting the global gas holdup in multiphase reactors (see Chapter 3.3.1) like BCR other than the correlation from Wang et al. [1] are compared to experimental work from this study (Fig. 15).

Table 5: *Statistical comparison between the methods shown in Fig. 15. The table shows the mean absolute error (MAE), the root mean squared error (RMSE), the mean absolute percentage error (MAPE), and the percentage of data points within a 10% and 20% error margin from the experimental data.*

Model	MAE	RMSE	MAPE (%)	% within ±10%	% within ±20%
Hughmark et al. (1967)	0.108	0.109	78	0	0
Hikita and Kikukawa (1974)	0.011	0.013	8	70	100
Kumar et al. (1976)	0.043	0.045	32	0	17
Hikita et al. (1980)	0.034	0.037	23	8	27
Reilly et al. (1986)	0.071	0.073	50	0	0
Behkish et al. (2006)	0.02	0.022	13	30	86
Anastasiou et al. (2010)	0.089	0.091	63	0	0
Azizi et al. (2019)	0.036	0.043	27	21	46
Method 2	0.007	0.009	5	87	100

Most of the correlations do not predict the mean gas holdup for the experimental conditions from the current study. The correlations from Hughmark Eq. 13 [68] and Anastasiou et al. Eq. 19 [74] are only applicable in the homogeneous regime according to their publications. Compared to the measurements

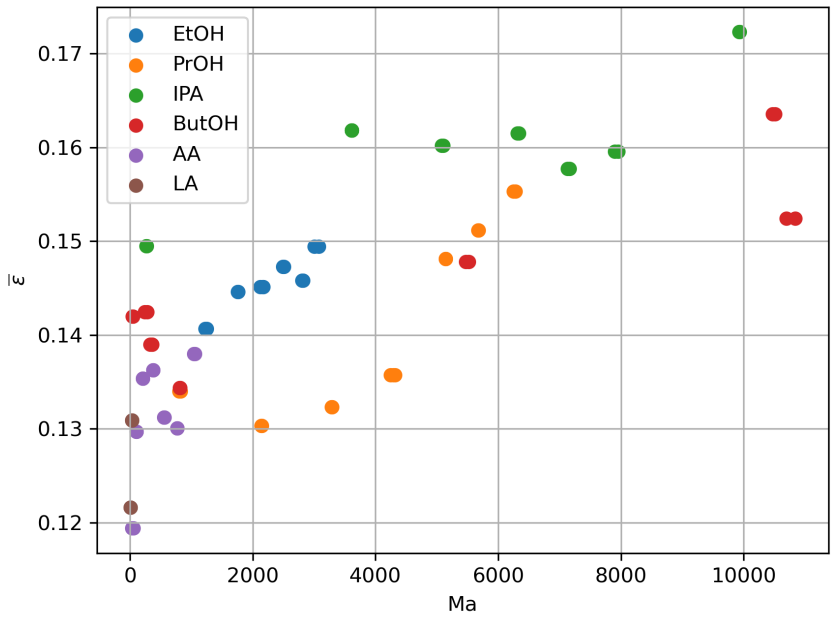

Figure 13: *The dependence of the Ma number on the global gas holdup. Here, the global gas holdup was determined using pressure probes and Eq. 2.*

from this study, they predict values for gas holdup well above the measured holdup. However, the trend of increased gas holdup for mixtures with a larger Ma number is visible. The correlation of Reilly et al. Eq. 17 [72] on the other hand does not predict many variations between the different conditions.

The most recent correlation examined is from Azizi et al. (Eq. 23) [75]. Their correlation predicts lower holdup values for mixtures with a higher Ma number. The reason for the disagreement between their correlation and the current study comes from the difference in experimental conditions. In their study they only used deionized water and air. The addition of surfactant molecules like acids and alcohols has a great effect on holdup which is not well captured in this correlation. Moreover, the correlation relies on a model predicting the mean bubble diameter. In their correlation for a system similar to the system used in the current study they use a mean bubble diameter of over 10 mm [75]. The mean diameter of the current study varies between the experiments due to addition of organic compounds. The d_{32} represents a good normalized mean diameter of the bubbles. In this study, however, the d_{32} was found to be around 4 mm (Appendix I).

The correlation proposed by Hikita and Kikukawa (Eq. 15) [70] aligns most closely with the results of the present study, predicting 70% of values within a 10% error margin and 100% of the values in a 20% margin of error relative to the experimental data (Table 5). It is surprising that the correlation proposed by Hikita and Kikukawa [70] (Eq. 15) provides more accurate predictions than the later correlation by Hikita et al. [71] (Eq. 16), especially given that the latter study noted their earlier model tends to overestimate the influence of surface tension. The negative exponent for σ indicates that lower surface tension leads to increased holdup. However, contrary to the claim by Hikita et al. [71], the earlier correlation does not appear to significantly overestimate this effect. The main reason for the disagreement of the relation from Hikita et al. (Eq. 16) is because they use a column with a diameter of 10 cm. The holdup of columns with a diameter lower than 10-15 cm are very dependent on the column diameter [72]. The correlation form Hikita and Kikukawa (Eq. 15) is based on experiments with a 19 cm diameter column.

The correlation from Behkish et al. (Eq. 18) [73] underestimates the holdup more than the correlation from Hikita and Kikukawa [70]. Behkish at al. [73] validated their correlation in a large scale slurry BCR with syngas making it most applicable for biotechnological processes like gas fermentation.

Despite some of the inaccuracies of the correlations shown in Fig. 15, the predicted holdup values by

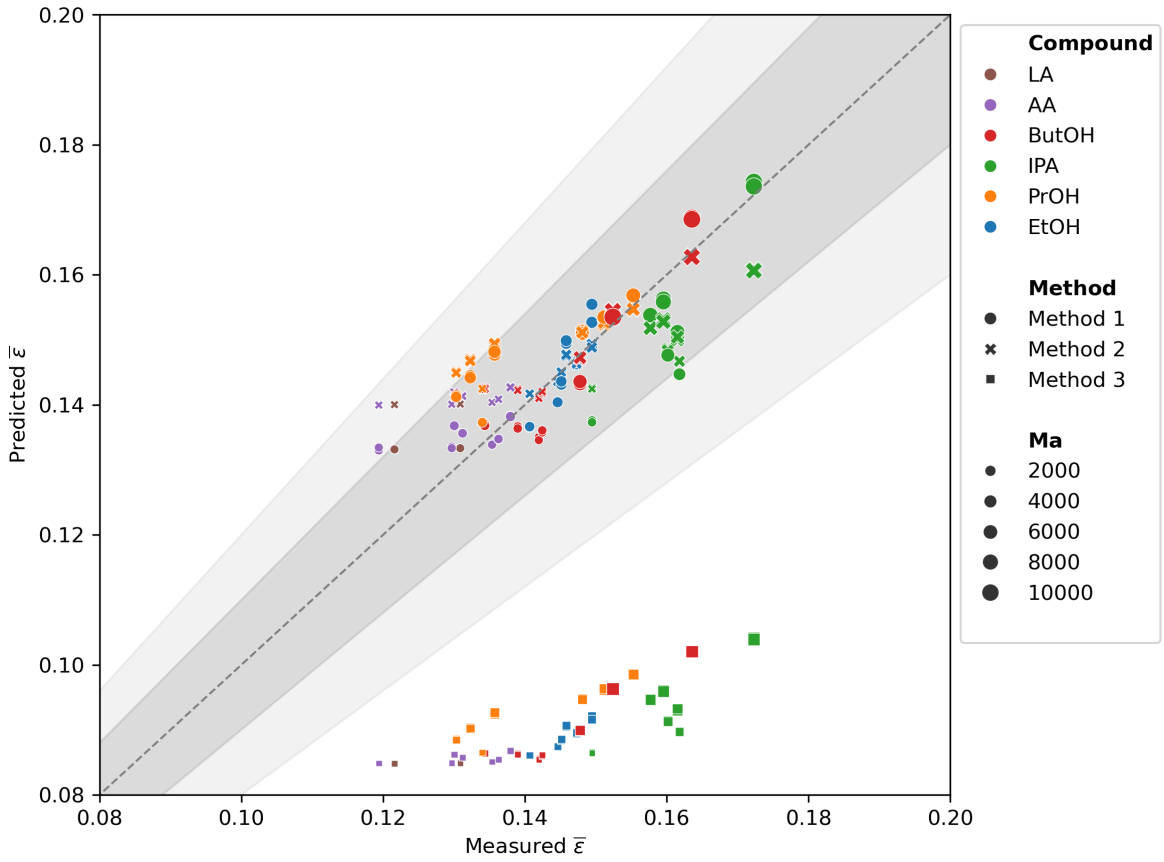

Figure 14: *Parity plot for comparison between the method and correlation of Wang et al. [1] and the current study. Error margins of 20% and 10% are indicated in gray.*

the correlation from Behkish et al. are for 86% within a 20% error margin. It is advisable to incorporate the Ma number in the correlation as done by Wang et al. Their correlation Eq. 33 interpreted using method 2 (see Chapter 3.3.3) shows best agreement with the experimental work from the current study,for 100%) within a 20% error margin (Table 4).

4.3 Local Holdup Correlations

Local holdup measurements were conducted using an optical fiber probe (see Fig. 16). Addition of organic compound results in an upward shift of the holdup distribution. However, further addition of organic compound results in a different change in distribution. For example, it is found that alcohols and acids increase gas holdup[10], but the distribution of the holdup becomes flatter as found by Veera et al. [82] in an experiment with *n*-butanol. The correlations from Wu et al. [83] (see Eq. 25), Schweitzer et al. [2] (see Eq. 26), Ueyama and Miyauchi [78] (see Eq. 24), and Azizi et al. [75] (see Eq. 27) predict these changes. Fig. 17 shows how well the correlations predict local gas holdup for conditions tested in the current study. The correlations are compared to the data for water and for the solution with the highest Ma number, in this case 1.2 g/l 1-butanol in water, in Fig. 18.

All correlations predict a lower holdup close to the wall than in the middle of the column. From Fig. 17 it is concluded that the correlation from Ueyama and Miyauchi (Eq. 24) overestimates the holdup across most of the column. The shape of the distribution is very flat from the middle of the column to around r/R=0.7 (Fig. 18). Then, the curve dramatically moves towards a holdup of 0 at the walls of the column. This shape results in an overestimation of the holdup for many locations between r/R=0 and r/R=1 (Fig. 18). The correlation from Ueyama and Miyauchi uses a parameter n to determine the shape of the distribution.

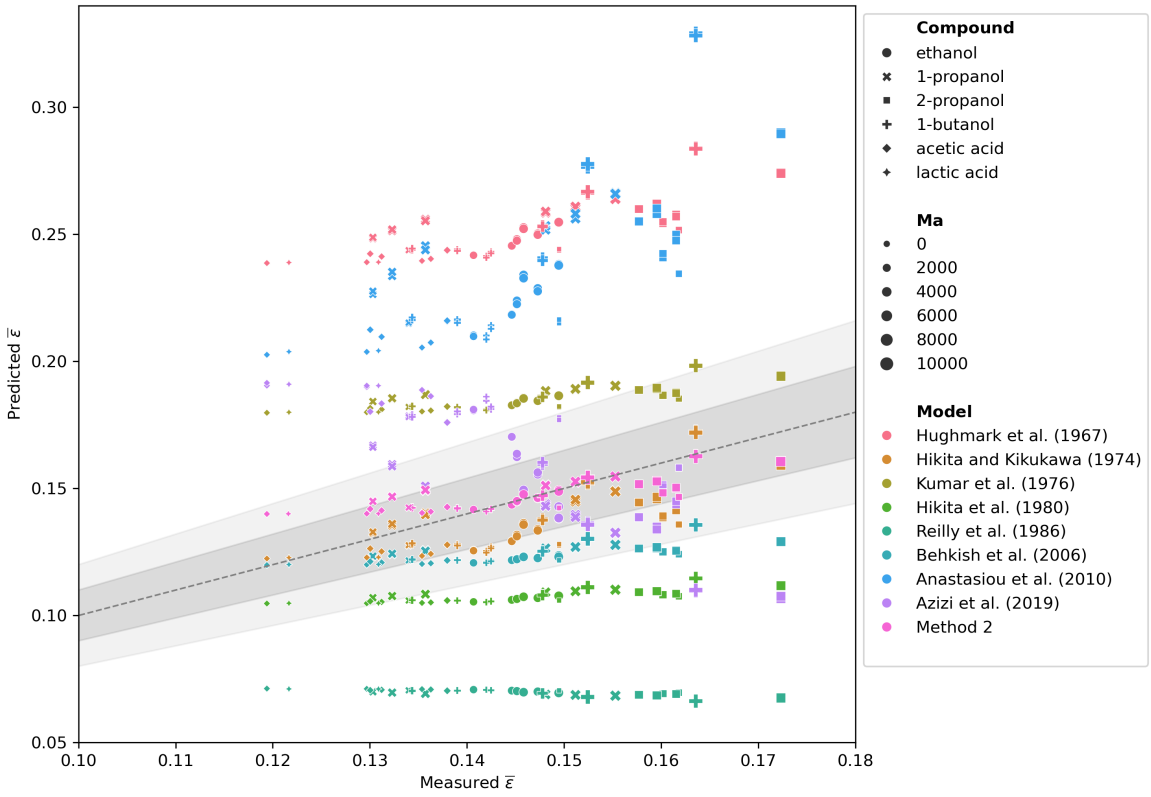

Figure 15: *Parity plot comparing different correlations for global gas holdup. Method 2 refers to the correlation described by Wang et al. [1] (Eq. 33), with the method described in this study (Chapter* **??***).*

They note values between 1.5 and 8 for different systems. The optimal value for n was found to be 5.8 for the current study. A sensitivity analysis shows the impact of this value on the shape of the distribution (see Appendix J, Fig. 40). Better fits can be found if the value n is optimized for every condition. However, general correlations without the need of fitting parameters are desired.

The correlation from Wu et al. (Eq. 25) overestimates the holdup the most close to the walls (Fig. 17). Fig. 18 clarifies that their correlation does not take into account that there are no bubbles at the walls of the column. The same problem appears for the correlation from Azizi et al. (Eq. 27). Both the correlations from Wu et al. and Azizi et al. show better predictions around the middle of the column (r/R close to 0), but underestimate. The correlation from Azizi et al. particularly underestimates the holdup for non-dimensional radius values (r/R) greater than 0.5 (close to the column wall). Since regions closer to the outer wall contribute more significantly to the overall holdup due to the cylindrical geometry, accurate predictions in this range are especially important (see Appendix K). Despite the physical principles captured in the correlations from Wu et al. and Azizi et al., they do not accurately predict the holdup distribution for the current process, making them not general applicable.

The correlation from Schweitzer et al. (Eq. 26) on the other hand, is relatively simple to apply. The only input parameter in this correlation is the mean holdup in the BCR. The mean holdup determined using the pressure probes was used for this. The correlation estimates the holdup distribution better than the other three correlation, despite its simplicity. Overall, the correlation overestimates the holdup, but mostly (89%) within a 20% margin (see Table 6 and Fig. 17). Fig. 18 further clarifies the good prediction ability of Eq. 26.

None of the correlations includes the Ma number. Still the correlation perform well for Marangoni numbers up to 5000 (Fig. 17). Fig. 17 suggests that local holdup of process conditions with Ma above 5000 are over-predicted by the models. However, statistical tests for this claim must be performed to draw

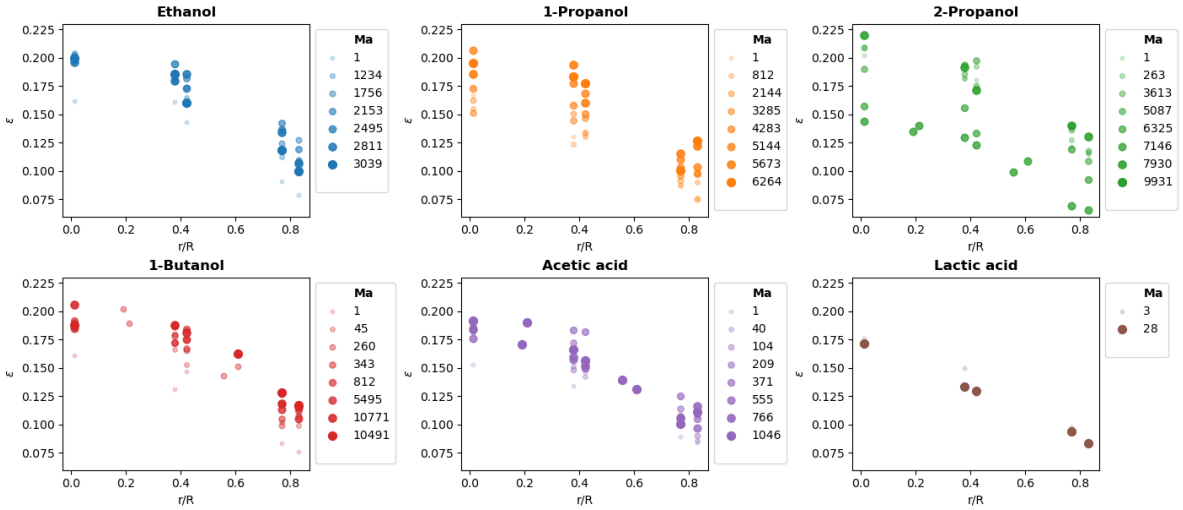

Figure 16: *Local holdup changes for ethanol, n-propanol, iso-proanol, n-butanol, acetic acid and lactic acid. The Ma number of without addition of organic compound is set to 1.*

Table 6: *Statistical comparison between the methods shown in Fig. 17. The table shows the mean absolute error (MAE), the root mean squared error (RMSE), the mean absolute percentage error (MAPE), and the percentage of data points within a 10% and 20% error margin from the experimental data.*

Model	MAE	RMSE	MAPE (%)	% within ±10%	% within ±20%
Wu et al. (2001)	0.021	0.026	17	39	69
Schweitzer et al. (2001)	0.013	0.02	10	70	89
Ueyama and Miyauchi (1979)	0.025	0.031	20	35	61
Azizi et al. (2019)	0.026	0.03	19	26	60

any conclusions.

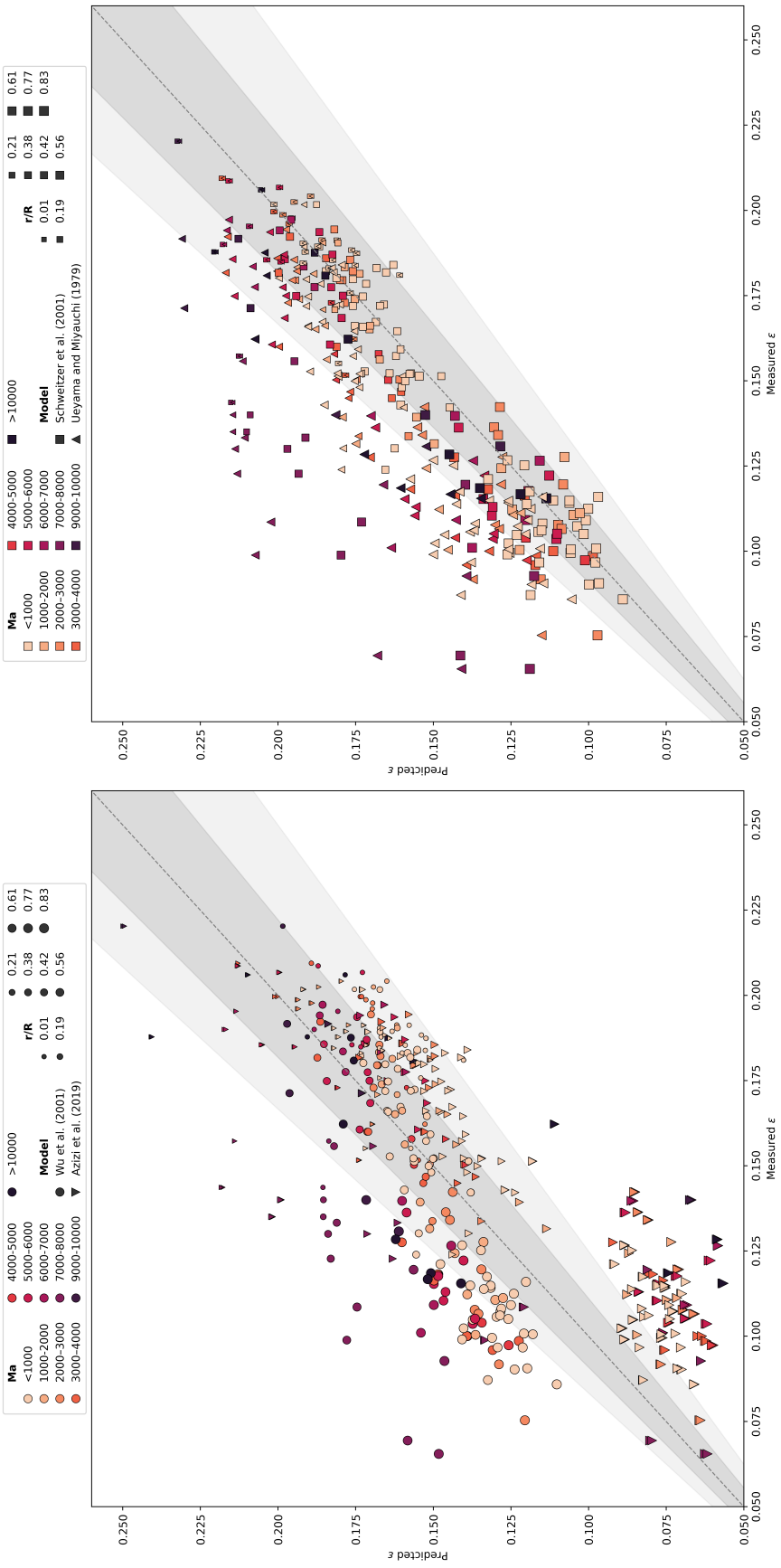

Figure 17: *Parity plot for local gas holdup distribution correlation. The prediction abilities of different models for gas holdup distribution are compared for the different dimensionless radii and Ma numbers. The size of the data points reflect the dimensionless radius. Larger data points are closer to the wall and have more impact on the global holdup due to the circular geometry.*

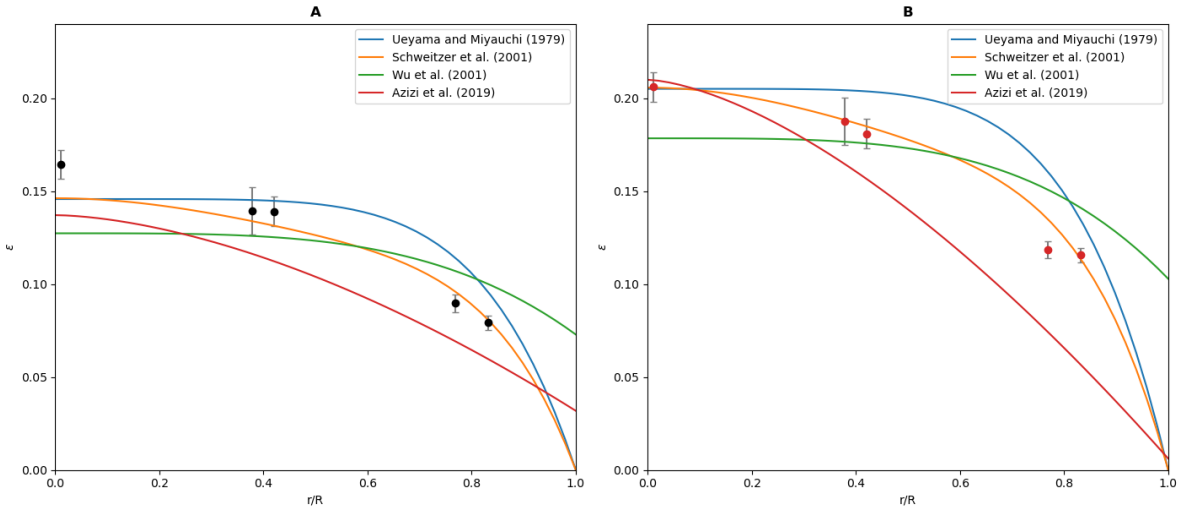

Figure 18: *Holdup distribution fits for water (A) and 1.2 g/l 1-butanol (B) which has the highest Ma number.*

5 Results: Improvement of X-ray Tomographic Techniques for Multiphase Flow Characterization

Scattering and beam hardening remain challenges for X-ray tomography in academia. This part of the current study will focus on the improvement of the methodology of X-ray tomography, challenging the hurdles of scattering and beam hardening. The distance through the BCR is calculated using data obtained from the calibration of the system using the method explained in Chapter 3.4.2. This chapter discussed a correction for cross-scattering and a method for beam hardening is explained.

5.1 Scattering

5.1.1 Dependence of Scatter on Holdup

Attaching the top part to the middle part of the column takes some time. To save time during experimental days. The amount of scattering was determined for the column with and without cap. It was found that the top part did not significantly influence the scattering when it was not placed near a detector or source.

The composition of the liquid can influence the amount of scattering. Therefore, scatter measurements (see Chapter 3.2.1) are conducted for all concentrations of all compounds. It was hypothesized that the gas holdup would not influence the amount of noise caused by scattering up to a certain point. This was tested by measuring scatter for a system with water at different gas flows. It was found that the gas-flow does not significantly impact the amount of scatter detected (Appendix L,Fig. 41).

5.1.2 Cross-Scatter correction

Different parts of the detector detect different amounts of scattering (see Appendix M, Fig. 42). Therefore, time-averaged scattering is subtracted from each pixel for each detector to obtain scatter-corrected 2D-images. This correction is applied to images of the full column and of images of the empty column. Reconstructions before and after scatter correction (SC) are compared by plotting the value $-\ln \frac{I(x)}{I_{empty}}$ against the distance through the column (Fig. 19). It is shown that $-\ln \frac{I(x)}{I_{empty}}$ is higher after SC, since the intensity ($I(x)$) is lower after correcting for cross-scattering.

$$-\ln \frac{I(x)}{I_0} = \mu x \tag{42}$$

5.2 Beam Hardening

The 2D X-ray images of the BCR must be corrected for beam hardening for accurate tomographic reconstruction. Without beam hardening, the logarithmic attenuation, as described by the rewritten Beer-Lambert law in Eq. 42, follows a linear relationship with a slope μ. However, in the presence of beam hardening, the effective attenuation coefficient decreases with increasing material thickness (see Chapter 2.6.4), resulting in a curved attenuation profile rather than a straight line, as seen in Fig. 19.

In the first part of the plot, where beam hardening does not play a significant role, we obtain a linear effective attenuation coefficient (slope) of around 0.2 cm^{-1}. The image data is corrected as if the attenuation coefficient is constant at this value.

To correct the images, we use pixel intensities from measurements of the full liquid-filled column (i.e., without gas) to compute $-\ln \frac{I(x)}{I_0}$ as a function of path length x. A horizontal band of pixels with a height of 100 pixels was used to fit a polynomial. This polynomial approximates the relationship between attenuation and distance through the medium, allowing us to estimate x for any measured attenuation value. A different polynomial is used for the left and right side of every detector.

The correction computes x from the measured intensity using the fitted polynomial, and then recalculates the 'ideal' attenuation using the linear Beer-Lambert relationship with $\mu = 0.2$ cm^{-1} (see Eq. 43). Applying this correction to the full-column data yields a linear attenuation profile, as expected for a system without beam hardening (see Fig. 19).

$$I_{\text{corr}} = I_{\text{empty}} e^{-0.2x} \tag{43}$$

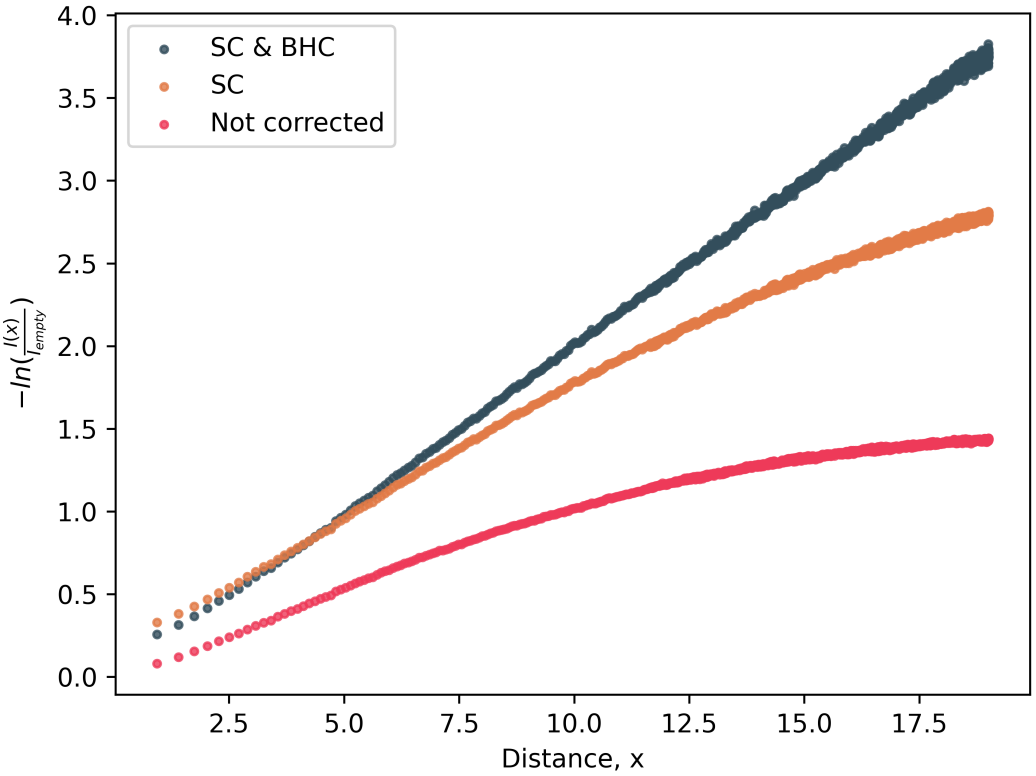

Figure 19: *Comparison between corrected and not corrected images. The data without corrections ('Not corrected') is compared to data corrected for scattering (SC) and with data corrected for both scattering and beam hardening (BHC).*

The same polynomial functions are used to correct the data from experiments with gas flow. The pixel intensity depends on how far the X-rays travel through the liquid. When gas is added to the bubble column, we do not know exactly how many bubbles are between the X-ray source and the detector, so the distance through the liquid is unknown. To find this distance, we use the measured intensity and the earlier polynomial fit. Then the corrected intensity is calculated using the linear equation with a constant $\mu = 0.2$ cm^{-1}. This results in images corrected for beam hardening (see Appendix N, Fig. 43).

If no correction is applied to the 2D images, a holdup profile opposite of what we expect is obtained, with low gas holdup in the middle of the column and relatively high holdup close to the walls of the column (see Fig. 20, "No Correction"). Overall the gas holdup is smaller than expected, ranging up to around 0.09.

Correcting for cross-scatter results in a reconstruction with overall higher holdup values. In the reconstruction, measurements from the BCR with and without gas flow are compared. The intensities of the not corrected pixels are the result of the intensity from scattering plus the intensity directly from the source. The high amount of noise due to scattering results in a relative small difference between the intensities from the measurements with and without gas flow. Therefore, the images of the BCR with gas flow are relatively similar to the images without gas flow. This effect appears in the reconstructions as low holdup values for the not corrected data (Fig. 20, "No Correction") and higher holdup values for scatter corrected data (Fig. 20, "SC").

The effect of beam hardening in BCR is characterized by a bright outer ring resulting in relatively high gas holdups close to the wall compared to the middle of the column. This effect is most clearly seen from the

reconstructions without any correction (Fig. 20, "No Correction"), but is still present in the reconstructions after correcting for cross-scattering (Fig. 20, "SC").

There are still inaccuracies in the reconstruction for the beam hardening corrected data. Since the left and right side of the detector were corrected with a different polynomial, the reconstructions for beam hardening corrected data result in different sections of intensities (Fig. 20). The value for $-\ln \frac{I(x)}{I_0}$ for different values of x should be the comparable for the two sides of the detector. However, often a clear difference between the two sides was visible (see Appendix O). A deviation between the calculated distances though the column (see Chapter 3.4.2) and the actual distance is found that could explain partly the inaccuracies in the reconstructions. Further explanation on this deviation can be found in Appendix O.

5.3 Comparison of Holdup Measurements with Different Techniques

Applying the beam hardening correction as explained earlier in this chapter without scatter correction, results in a reconstruction that is not physically interpretable. However, applying the scatter correction in combination with the beam hardening correction, we obtain a reconstruction with the expected holdup profile (Fig. 20, "SC + BHC"). The profile is similar to the profile found with the optical fiber probe (see Fig. 21).

Reconstructions were performed for all component concentrations after SC and BHC. The resulting profiles were integrated to calculate the cross-sectional holdup (see Appendix K). The total holdup measured using XRT was higher than that obtained with both the optical fiber probe and the pressure probes (Fig. 22). The holdup distribution profiles from the X-ray reconstructions do not show a holdup of 0 at the walls. Here the holdup has a greater impact on the overall holdup due to the cylinder geometry (see Eq. 44 Appendix K). This could explain the over-prediction of overall holdup values for XRT.

A possible reason for the non-zero holdup at the walls comes from the inaccuracy in geometric calculations of the column (see Appendix O). This results in wrong reconstructions with higher errors close to the walls. Another reason for the non-zero holdup at the wall of the column comes from the geometric artifact caused by the low number of X-ray sources. Since only 3 source/detectors pairs are used for the reconstructions, a heptagon-shaped column is reconstructed instead of a circular column. This is another source of error which has greater implications close to the walls.

Determination of global gas holdup with different measurement techniques results in different outcomes. Pressure probe measurements are considered to be most reliable to measure global holdup. The pressure probes are independent of complex flow features, unlike local measurement techniques like the fiber probe and XRT. XRT is sensitive to alignment errors, artifacts (e.g. geometric artifacts, and beam hardening), and to noise (e.g. scatter). Fiber probe measurements results in a lower overall gas holdup. Bubbles under 100 μm are not measured by the fiber probe since they are too small to be perforated by the tip, resulting in a underestimation of the gas holdup. Furthermore, small bubbles with low velocity are rejected from the probe tip due to surface tension [84]. Another source of error could come from the deformation of bubbles when they are pieced by the probe tip [85]. Additionally, the addition of surface active compounds make the bubbles more rigid [86] and possibly harder to penetrate by the tip of the fiber probe. This results in a lower measured gas gas holdup.

In this study the radial average holdup of one cross-sectional slice from the column is considered to be the global gas holdup for XRT and FP measurements. Therefore, the variations in holdup along the axial direction is neglected for these measurement techniques. Pressure differences between the top and bottom of the BCR can affect gas holdup, because the gas expands when pressure decreases as the gas moves to the top [87]. However, the pressure difference between the bottom and top of the BCR is considered too small to significantly alter holdup near the sparger relative to the total holdup measured by the pressure probes. Thus, it is assumed that axial gas holdup differences are relatively small in small bubble column.

Measurements were taken relatively close to the sparger plate. Fiber probe measurements were taken at 57.5 cm above the sparger (Fig. 4) and the holdup determination from XRT is done for a single cross-sectional slice between 37.5 cm and 57.5 cm. Gong et al. found that a dynamic equilibrium region was only established 2.8 m above the bubble generator [88]. The effect of the sparger plate might be present for the measurements conducted in this study. Even though, the holdup is dependent on the location of the measurements, the measurements are still conducted in the same region.

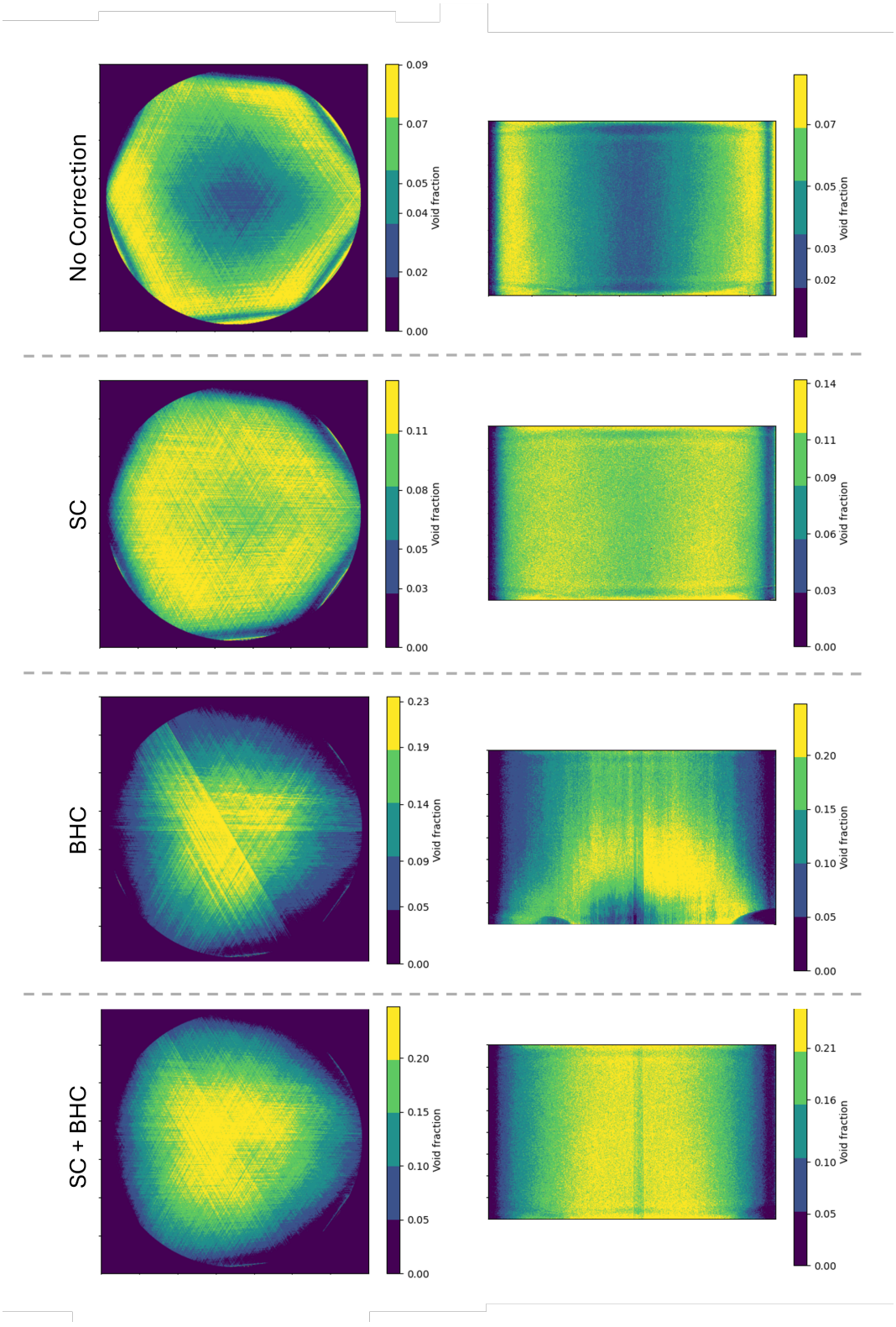

Figure 20: *Reconstructions of the data without correction (No Correction), after cross-scatter correction (SC), after beam hardening correction (BHC), and after cross-scatter correction and beam hardening correction (SC + BHC). The reconstructions are depicted as horizontal slices (left) and vertical slices (right). Note that the color-bars have different values, colors between images are not comparable.*

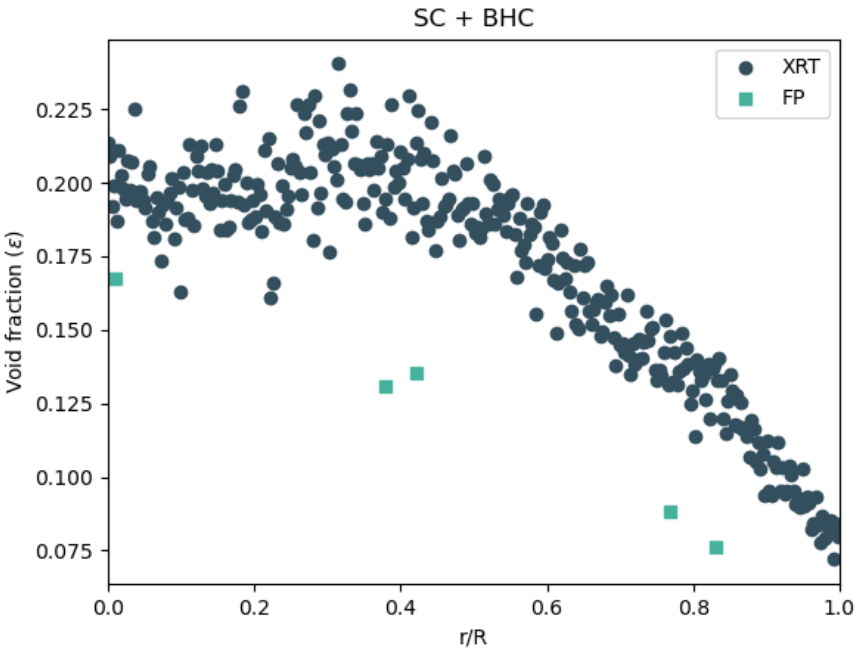

Figure 21: *Comparison of the holdup distribution measurements from the fiber probe (FP) and X-ray tomography (XRT) in a BCR filled with water at* $U_g = 0.05$ *m/s.*

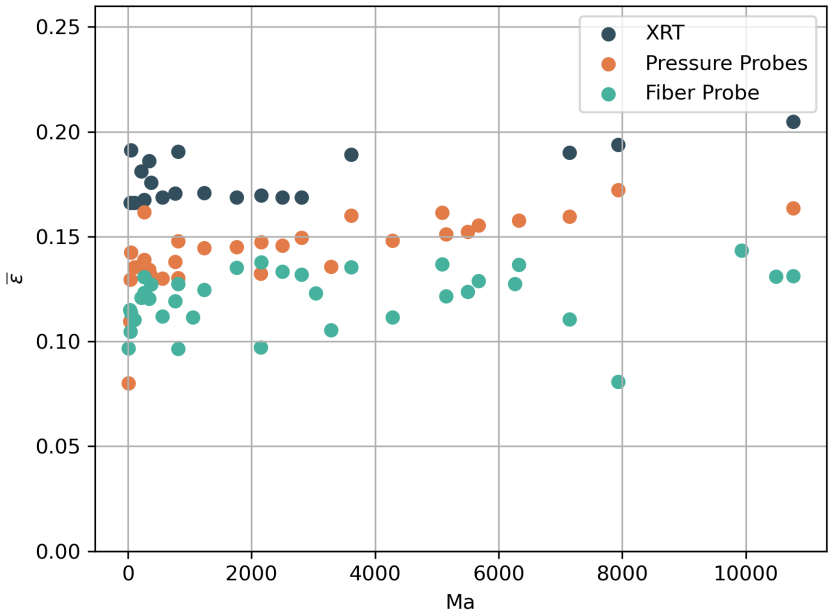

Figure 22: *Comparison of global holdup measurements of pressure probes, a fiber probe and X-ray tomography.*

6 Conclusion

This study investigated the effect of the important fermentation products ethanol, *n*-propanol, *iso*-propanol, *n*-butanol, acetic acid and lactic acid on gas holdup in BCRs. A primary objective was to correlate physical and operational properties with global gas holdup. Analysis compared several existing correlations that do not explicitly incorporate the Marangoni effect. Among these, the correlation by Hikita and Kikukawa (Eq. 15) [70] aligned best with the experimental data (70% within a 10% error margin). The correlation by Behkish et al. (Eq. 18) [73], which accounts for gas, liquid, and solid phases, also demonstrated strong predictive performance, especially under conditions relevant to biotechnological processes. Both models agreed with the measured data within a 20% margin (Fig. 15).

A further goal was to evaluate the influence of the Marangoni effect on gas holdup. While earlier work by Wang et al. [1] addressed this in a water–ethanol system, inconsistent definitions of dimensionless numbers have hindered reproducibility. This study reproduced Wang et al.'s results for water–ethanol and expanded the approach to include additional alcohols and acids. A revised method for calculating the Marangoni number (Method 2, Chapter 3.3.3), combined with the correlation from Wang et al. (Eq. 33), yielded strong agreement with experimental data, with 87% of predictions falling within a 10% error margin (Fig. 14). These results highlight the importance of including Marangoni effects in BCR modeling.

Local gas holdup distribution was also analyzed. Among the compared correlations, the model by Schweitzer et al. (Eq. 26) [2] showed the best performance, accurately predicting 70% of local holdup values within 10% error (Fig. 17, Fig. 18, Table 6). This model requires only the mean gas holdup as an input, making it straightforward to apply. When combined with global gas holdup predictions, it offers a reliable method for estimating local holdup in BCRs.

The second part of this thesis focused on improving X-ray tomography (XRT) methodologies for gas holdup measurements in BCRs. Initial reconstructions from raw X-ray data deviated significantly from reference measurements obtained via optical fiber probes and pressure differences. Two main sources of error, X-ray scattering and beam hardening, were identified and addressed. A method was developed to estimate the X-ray path length through the reactor, enabling corrections.

Cross-scattering was quantified and corrected, but this alone did not yield accurate reconstructions. Subsequent analysis revealed that beam hardening had a substantial impact on image quality. By applying corrections for both scattering and beam hardening, the reconstructed gas holdup profiles closely matched those obtained from optical fiber probes. However, a consistent bias remained: XRT slightly overestimated total holdup, while fiber probes underestimated it, compared to pressure-based measurements.

These findings demonstrate that, with proper correction techniques, XRT can be a powerful non-invasive tool for studying gas holdup in multiphase reactors. The methodology developed here can serve as a guideline for researchers working with similar X-ray imaging systems.

7 Future Recommendations

This research evaluated different correlations for gas holdup in BCRs. Furthermore, this thesis showed a method improving XRT for BCRs by showing a method to correct for scattering and beam hardening. This chapter discusses recommendations for future work.

7.1 Correlations

Many industrial fluids are non-Newtonian or contain cells. Future studies should extend gas holdup measurements to such complex systems, where bubble dynamics and holdup can differ substantially from Newtonian single-phase liquids.

This thesis only grasped the surface of the study on bubble size distributions in bubble columns. Measurements on BSD were only conducted for a small number liquid compositions. However, the change in BSD has great impact on gas-liquid mass transfer. The specific interfacial area (a) in the volumetric mass transfer coefficient ($k_L a$) is directly influenced by the size and distribution of bubbles, with smaller bubbles generally resulting in a larger interfacial area due to their higher surface-to-volume ratio.

Measurements for BSD and $k_L a$ enable the possibility to quantify the therm k_L. It was shown that alcohols reduce this value [89]. The rigid boundary layer decrease effective gas diffusivity and limit turbulence driven mass transfer [86, 90]. The effect of some other fermentation solutes on k_L like biomass and salts is known [10]. The effect of other solutes (e.g. proteins, sugars and acids) on k_L is less well studied [10]. Disentanglement of the two parameters k_L and a facilitate more advanced process performance predictions[10].

The Marangoni effect is for a large part responsible for reduced bubble coalescence. The correlation from Wang et al. [1] shows that global gas holdup and $k_L a$ correlate well with the Ma number. Is this thesis an attempt was made to extend their work for other process conditions and different solutes. Future work should focus on validating the correlation between gas holdup and Ma for more complex fermentation compositions.

Attempts for holdup distribution correlation in BCRs, capturing complex process conditions show not to be reliable for the system of the current study. Future work should focus on correlations that correlate the gas holdup distribution to liquid properties and not only to global gas holdup. The correlation from Schweitzer et al. Eq. 26 is expected not to work for more complex fermentation broths. For example, it was shown in this research that correlations for gas holdup distribution are less reliable for process conditions with high Ma numbers (Fig. 17).

The correlations examined in this study were evaluated only at a superficial gas velocity of 0.05 m/s, which typically represents the minimum velocity at which the heterogeneous flow regime occurs. Future research should aim to validate these correlations across a broader range of gas velocities.

7.2 XRT

XRT shows great potential to quantify local gas holdup in BCRs. This work, however, showed some of the shortcomings. Reliable measurements need the BCR to be placed at exactly the same position as during the calibration. A reliable method to reproduce the same column position is necessary. Calibration of the set-up more regularly between experiments can also reduce the effect of displacement.

This research showed how cross-scatter can be quantified, and how to correct X-ray images for this noise. However, forward-scatter also results in noise (Fig. 3). In the current setup, the cone-shaped beam has a significantly wider angle than necessary, resulting in increased scatter from X-rays outside the actual measurement region. This scattered radiation contributes to image noise and can negatively affect reconstruction quality. By cropping the beam to the relevant angular range with a collimator, the amount of scatter can be reduced, leading to improved signal-to-noise ratio and more accurate reconstructions [60]. Improvements on the set-up regarding a beam cropper are already on going.

Another advantage of the collimator is that beam hardening can be quantified for small sections of the detector. In the current study there is only a distinction between the left and right side of the detector. In this approach beam hardening is quantified for a narrow band of pixels in a horizontal line. The beam hardening effects detected on the entire detector are corrected for the effects measured in this narrow region. Ideally, beam hardening is quantified for every pixel and the signal detected is corrected for every pixel. This might be practically unfeasible, but a collimator enables the possibility to quantify beam hardening for small areas of the detector.

This study showed time-averaged CT reconstructions. The setup used in this study has also shown to be suitable for time-resolved reconstruction in a fluidized-bed reactor [53]. Time-resolved X-ray tomography enables the investigation of bubble interactions. Liquid and gas circulations are very dynamic in BCRs. Therefore, a higher frame rate is required. Since each frame is captured in a shorter time, the number of detected photons is lower. Less detected photons results in lower resolution images and a lower signal to noise ratio. Future studies should aim to overcome these obstacles.

References

[1] Yuelin Wang, Xiankun Shen, Huahai Zhang, and Tiefeng Wang. Marangoni effect on hydrodynamics and mass transfer behavior in an internal loop airlift reactor under elevated pressure. *AIChE Journal*, 70(2), 2024. ISSN 0001-1541. doi: 10.1002/aic.18291. URL https://dx.doi.org/10.1002/aic.18291.

[2] J-M Schweitzer, J Bayle, and T Gauthier. Local gas hold-up measurements in fluidized bed and slurry bubble column. *Chemical Engineering Science*, 56(3):1103–1110, February 2001. ISSN 0009-2509. doi: 10.1016/S0009-2509(00)00327-4. URL https://www.sciencedirect.com/science/article/pii/S0009250900003274.

[3] C. Leonard, J. H. Ferrasse, O. Boutin, S. Lefevre, and A. Viand. Bubble column reactors for high pressures and high temperatures operation. *Chemical Engineering Research and Design*, 100:391–421, 2015. ISSN 0263-8762. doi: 10.1016/j.cherd.2015.05.013. URL https://dx.doi.org/10.1016/j.cherd.2015.05.013.

[4] Milorad P. Dudukovic, Faical Larachi, and Patrick L. Mills. Multiphase reactors – revisited. *Chemical Engineering Science*, 54(13-14):1975–1995, 1999. ISSN 0009-2509. doi: 10.1016/s0009-2509(98)00367-4. URL https://dx.doi.org/10.1016/S0009-2509(98)00367-4.

[5] Hiroshi Kikukawa. Physical and transport properties governing bubble column operations. *International Journal of Multiphase Flow*, 93:115–129, 2017. ISSN 0301-9322. doi: 10.1016/j.ijmultiphaseflow.2017.03.017. URL https://dx.doi.org/10.1016/j.ijmultiphaseflow.2017.03.017.

[6] Katherine Calvin, Dipak Dasgupta, Gerhard Krinner, Aditi Mukherji, Peter W. Thorne, Christopher Trisos, José Romero, Paulina Aldunce, Ko Barrett, Gabriel Blanco, William W.L. Cheung, Sarah Connors, Fatima Denton, Aïda Diongue-Niang, David Dodman, Matthias Garschagen, Oliver Geden, Bronwyn Hayward, Christopher Jones, Frank Jotzo, Thelma Krug, Rodel Lasco, Yune-Yi Lee, Valérie Masson-Delmotte, Malte Meinshausen, Katja Mintenbeck, Abdalah Mokssit, Friederike E.L. Otto, Minal Pathak, Anna Pirani, Elvira Poloczanska, Hans-Otto Pörtner, Aromar Revi, Debra C. Roberts, Joyashree Roy, Alex C. Ruane, Jim Skea, Priyadarshi R. Shukla, Raphael Slade, Aimée Slangen, Youba Sokona, Anna A. Sörensson, Melinda Tignor, Detlef Van Vuuren, Yi-Ming Wei, Harald Winkler, Panmao Zhai, Zinta Zommers, Jean-Charles Hourcade, Francis X. Johnson, Shonali Pachauri, Nicholas P. Simpson, Chandni Singh, Adelle Thomas, Edmond Totin, Paola Arias, Mercedes Bustamante, Ismail Elgizouli, Gregory Flato, Mark Howden, Carlos Méndez-Vallejo, Joy Jacqueline Pereira, Ramón Pichs-Madruga, Steven K. Rose, Yamina Saheb, Roberto Sánchez Rodríguez, Diana Ürge Vorsatz, Cunde Xiao, Noureddine Yassaa, Andrés Alegría, Kyle Armour, Birgit Bednar-Friedl, Kornelis Blok, Guéladio Cissé, Frank Dentener, Siri Eriksen, Erich Fischer, Gregory Garner, Céline Guivarch, Marjolijn Haasnoot, Gerrit Hansen, Mathias Hauser, Ed Hawkins, Tim Hermans, Robert Kopp, Noëmie Leprince-Ringuet, Jared Lewis, Debora Ley, Chloé Ludden, Leila Niamir, Zebedee Nicholls, Shreya Some, Sophie Szopa, Blair Trewin, Kaj-Ivar Van Der Wijst, Gundula Winter, Maximilian Witting, Arlene Birt, Meeyoung Ha, José Romero, Jinmi Kim, Erik F. Haites, Yonghun Jung, Robert Stavins, Arlene Birt, Meeyoung Ha, Dan Jezreel A. Orendain, Lance Ignon, Semin Park, Youngin Park, Andy Reisinger, Diego Cammaramo, Andreas Fischlin, Jan S. Fuglestvedt, Gerrit Hansen, Chloé Ludden, Valérie Masson-Delmotte, J.B. Robin Matthews, Katja Mintenbeck, Anna Pirani, Elvira Poloczanska, Noëmie Leprince-Ringuet, and Clotilde Péan. IPCC, 2023: Climate Change 2023: Synthesis Report. Contribution of Working Groups I, II and III to the Sixth Assessment Report of the Intergovernmental Panel on Climate Change [Core Writing Team, H. Lee and J. Romero (eds.)]. IPCC, Geneva, Switzerland. Technical report, Intergovernmental Panel on Climate Change (IPCC), July 2023. URL https://www.ipcc.ch/report/ar6/syr/. Edition: First.

[7] K. D. González-Gloria, Rosa M. Rodríguez-Jasso, Rohit Saxena, Raveendran Sindhu, Sameh S. Ali, Reeta Rani Singhania, Anil Kumar Patel, Parameswaran Binod, and Héctor A. Ruiz. Bubble column bioreactor design and evaluation for bioethanol production using simultaneous saccharification and fermentation strategy from hydrothermally pretreated lignocellulosic biomass. *Biochemical Engineering*

Journal, 187:108645, 2022. ISSN 1369-703X. doi: 10.1016/j.bej.2022.108645. URL https://dx.doi.org/10.1016/j.bej.2022.108645.

[8] Michael Köpke and Séan D. Simpson. Pollution to products: recycling of 'above ground' carbon by gas fermentation. *Current Opinion in Biotechnology*, 65:180–189, 2020. ISSN 0958-1669. doi: 10.1016/j.copbio.2020.02.017. URL https://dx.doi.org/10.1016/j.copbio.2020.02.017.

[9] Lars Puiman, Marina P. Elisiário, Lilo M. L. Crasborn, Liselot E. C. H. Wagenaar, Adrie J. J. Straathof, and Cees Haringa. Gas mass transfer in syngas fermentation broths is enhanced by ethanol. *Biochemical Engineering Journal*, 185:108505, 2022. ISSN 1369-703X. doi: 10.1016/j.bej.2022.108505. URL https://dx.doi.org/10.1016/j.bej.2022.108505.

[10] R. Volger, L. Puiman, and C. Haringa. Bubbles and Broth: A review on the impact of broth composition on bubble column bioreactor hydrodynamics. *Biochemical Engineering Journal*, 201:109124, 2024. ISSN 1369-703X. doi: 10.1016/j.bej.2023.109124. URL https://dx.doi.org/10.1016/j.bej.2023.109124.

[11] M. Jamialahmadi and H. Müller-Steinhagen. Effect of alcohol, organic acid and potassium chloride concentration on bubble size, bubble rise velocity and gas hold-up in bubble columns. *The Chemical Engineering Journal*, 50(1):47–56, October 1992. ISSN 0300-9467. doi: 10.1016/0300-9467(92)80005-U. URL https://www.sciencedirect.com/science/article/pii/030094679280005U.

[12] Azadeh Bahramian and Siamak Elyasi. A Numerical Model for Bubble Column Reactors: Prediction of the Fractional Gas Holdup by the Implementation of the Drift-Flux Model. *Journal of Chemical Engineering & Process Technology*, 10(2):1–12, August 2019. ISSN 2157-7048. doi: 10.35248/2157-7048.19.10.396. URL https://www.longdom.org/. Publisher: Longdom Publishing S.L.

[13] Shu Takagi and Yoichiro Matsumoto. Surfactant Effects on Bubble Motion and Bubbly Flows. *Annual Review of Fluid Mechanics*, 43(Volume 43, 2011):615–636, January 2011. ISSN 0066-4189, 1545-4479. doi: 10.1146/annurev-fluid-122109-160756. URL https://www.annualreviews.org/content/journals/10.1146/annurev-fluid-122109-160756. Publisher: Annual Reviews.

[14] Jiakai Lu, Carlos M. Corvalan, Y. M. John Chew, and Jen-Yi Huang. Coalescence of small bubbles with surfactants. *Chemical Engineering Science*, 196:493–500, March 2019. ISSN 0009-2509. doi: 10.1016/j.ces.2018.11.002. URL https://www.sciencedirect.com/science/article/pii/S0009250918307802.

[15] Xiangyang Li, Chao Yang, Shifang Yang, and Guozheng Li. Fiber-Optical Sensors: Basics and Applications in Multiphase Reactors. *Sensors (Basel, Switzerland)*, 12(9):12519–12544, September 2012. ISSN 1424-8220. doi: 10.3390/s120912519. URL https://www.ncbi.nlm.nih.gov/pmc/articles/PMC3478856/.

[16] Philip J. Withers, Charles Bouman, Simone Carmignato, Veerle Cnudde, David Grimaldi, Charlotte K. Hagen, Eric Maire, Marena Manley, Anton Du Plessis, and Stuart R. Stock. X-ray computed tomography. *Nature Reviews Methods Primers*, 1(1):1–21, February 2021. ISSN 2662-8449. doi: 10.1038/s43586-021-00015-4. URL https://www.nature.com/articles/s43586-021-00015-4. Publisher: Nature Publishing Group.

[17] Manuel Baur, Norman Uhlmann, Thorsten Pöschel, and Matthias Schröter. Correction of beam hardening in X-ray radiograms. *Review of Scientific Instruments*, 90(2):025108, February 2019. ISSN 0034-6748. doi: 10.1063/1.5080540. URL https://doi.org/10.1063/1.5080540.

[18] Kaiqiao Wu, Rens Kamphorst, Anna Bakker, Jasper Ford, Evert C. Wagner, Olga Ochkin-Koenig, Miika Franck, Dominik Weis, Gabrie M. H. Meesters, and J. Ruud van Ommen. Stirrer design for improving fluidization of cohesive powder: A time-resolved X-ray study. *Chemical Engineering Science*, 294:120069, July 2024. ISSN 0009-2509. doi: 10.1016/j.ces.2024.120069. URL https://www.sciencedirect.com/science/article/pii/S0009250924003695.

[19] Giorgio Besagni and Fabio Inzoli. Influence of electrolyte concentration on holdup, flow regime transition and local flow properties in a large scale bubble column. *Journal of Physics: Conference Series*, 655:012039, 2015. ISSN 1742-6588. doi: 10.1088/1742-6596/655/1/012039. URL https://dx.doi.org/10.1088/1742-6596/655/1/012039.

[20] Giorgio Besagni, Fabio Inzoli, and Thomas Ziegenhein. Two-Phase Bubble Columns: A Comprehensive Review. *ChemEngineering*, 2(2):13, 2018. ISSN 2305-7084. doi: 10.3390/chemengineering2020013. URL https://dx.doi.org/10.3390/chemengineering2020013.

[21] Giorgio Besagni, Fabio Inzoli, Giorgia De Guido, and Laura Annamaria Pellegrini. Experimental investigation on the influence of ethanol on bubble column hydrodynamics. *Chemical Engineering Research and Design*, 112:1–15, 2016. ISSN 0263-8762. doi: 10.1016/j.cherd.2016.06.009. URL https://dx.doi.org/10.1016/j.cherd.2016.06.009.

[22] D. Lucas, H. M. Prasser, and A. Manera. Influence of the lift force on the stability of a bubble column. *Chemical Engineering Science*, 60(13):3609–3619, July 2005. ISSN 0009-2509. doi: 10.1016/j.ces.2005.02.032. URL https://www.sciencedirect.com/science/article/pii/S0009250905001326.

[23] Hanjin Im, Jeil Park, and Jae W. Lee. Prediction of Main Regime Transition with Variations of Gas and Liquid Phases in a Bubble Column. *ACS Omega*, 4(1):1329–1343, January 2019. doi: 10.1021/acsomega.8b02657. URL https://doi.org/10.1021/acsomega.8b02657. Publisher: American Chemical Society.

[24] J. Zahradnik, M. Fialova, M. Ruzicka, J. Drahos, F. Kastanek, and N. H. Thomas. Duality of the gas-liquid flow regimes in bubble column reactors. *Chemical Engineering Science*, 52(21):3811–3826, November 1997. ISSN 0009-2509. doi: 10.1016/S0009-2509(97)00226-1. URL https://www.sciencedirect.com/science/article/pii/S0009250997002261.

[25] M. Gumulya, J. B. Joshi, R. P. Utikar, G. M. Evans, and V. Pareek. Characteristics of energy production and dissipation around a bubble rising in water. *Chemical Engineering Science*, 193:38–52, January 2019. ISSN 0009-2509. doi: 10.1016/j.ces.2018.08.059. URL https://www.sciencedirect.com/science/article/pii/S0009250918306389.

[26] Yuyun Bao, Zhichao Jiang, Shuaifei Tong, Xiongbin Huang, Ziqi Cai, and Zhengming Gao. Reactive mass transfer of single O2 bubbles in a turbulent flow chamber. *Chemical Engineering Science*, 207:829–843, November 2019. ISSN 0009-2509. doi: 10.1016/j.ces.2019.07.006. URL https://www.sciencedirect.com/science/article/pii/S0009250919305706.

[27] Roya Jamshidian, James Scully, and Harry E. A. Van den Akker. A computational fluid dynamics study of mass transfer in a large-scale aerated stirred bioreactor. *Chemical Engineering Journal*, 509:160723, April 2025. ISSN 1385-8947. doi: 10.1016/j.cej.2025.160723. URL https://www.sciencedirect.com/science/article/pii/S138589472501544X.

[28] Caleb S. Brooks, Sidharth S. Paranjape, Basar Ozar, Takashi Hibiki, and Mamoru Ishii. Two-group drift-flux model for closure of the modified two-fluid model. *International Journal of Heat and Fluid Flow*, 37:196–208, 2012. ISSN 0142-727X. doi: 10.1016/j.ijheatfluidflow.2012.04.002. URL https://dx.doi.org/10.1016/j.ijheatfluidflow.2012.04.002.

[29] Y. T. Shah, B. G. Kelkar, S. P. Godbole, and W. -D Deckwer. Design parameters estimations for bubble column reactors. *AIChE Journal*, 28(3):353–379, 1982. ISSN 0001-1541. doi: 10.1002/aic.690280302. URL https://dx.doi.org/10.1002/aic.690280302.

[30] Giorgio Besagni, Lorenzo Gallazzini, and Fabio Inzoli. On the scale-up criteria for bubble columns. *Petroleum*, 5(2):114–122, June 2019. ISSN 2405-6561. doi: 10.1016/j.petlm.2017.12.005. URL https://www.sciencedirect.com/science/article/pii/S2405656117301645.

[31] Peter M. Wilkinson, Arie P. Spek, and Laurent L. van Dierendonck. Design parameters estimation for scale-up of high-pressure bubble columns. *AIChE Journal*, 38(4):544–554, 1992. ISSN 1547-5905. doi: 10.1002/aic.690380408. URL https://onlinelibrary.wiley.com/doi/abs/10.1002/aic.690380408. _eprint: https://onlinelibrary.wiley.com/doi/pdf/10.1002/aic.690380408.

[32] Shohei Sasaki, Kengo Uchida, Kosuke Hayashi, and Akio Tomiyama. Effects of column diameter and liquid height on gas holdup in air-water bubble columns. *Experimental Thermal and Fluid Science*, 82:359–366, April 2017. ISSN 0894-1777. doi: 10.1016/j.expthermflusci.2016.11.032. URL https://www.sciencedirect.com/science/article/pii/S0894177716303478.

[33] Giorgio Besagni, Nicolò Varallo, and Riccardo Mereu. Computational Fluid Dynamics Modelling of Two-Phase Bubble Columns: A Comprehensive Review. *Fluids*, 8(3):91, 2023. ISSN 2311-5521. doi: 10.3390/fluids8030091. URL https://dx.doi.org/10.3390/fluids8030091.

[34] Gunter Keitel and Ulfert Onken. Inhibition of bubble coalescence by solutes in air/water dispersions. *Chemical Engineering Science*, 37(11):1635–1638, 1982. ISSN 0009-2509. doi: 10.1016/0009-2509(82)80033-x. URL https://dx.doi.org/10.1016/0009-2509(82)80033-X.

[35] Ayanavilli Srinivas and Pallab Ghosh. Coalescence of Bubbles in Aqueous Alcohol Solutions. *Industrial & Engineering Chemistry Research*, 51(2):795–806, January 2012. ISSN 0888-5885. doi: 10.1021/ie202148e. URL https://doi.org/10.1021/ie202148e. Publisher: American Chemical Society.

[36] Christine Browne, Rico F. Tabor, Derek Y. C. Chan, Raymond R. Dagastine, Muthupandian Ashokkumar, and Franz Grieser. Bubble Coalescence during Acoustic Cavitation in Aqueous Electrolyte Solutions. *Langmuir*, 27(19):12025–12032, October 2011. ISSN 0743-7463. doi: 10.1021/la202804c. URL https://doi.org/10.1021/la202804c. Publisher: American Chemical Society.

[37] P. Chen, J. Sanyal, and M. P. Duduković. Numerical simulation of bubble columns flows: effect of different breakup and coalescence closures. *Chemical Engineering Science*, 60(4):1085–1101, February 2005. ISSN 0009-2509. doi: 10.1016/j.ces.2004.09.070. URL https://www.sciencedirect.com/science/article/pii/S000925090400733X.

[38] Stefan A. Zieminski, M. M. Caron, and Ruth Benton Blackmore. Behavior of Air Bubbles in Dilute Aqueous Solutions. *Industrial & Engineering Chemistry Fundamentals*, 6:233–242, 1967.

[39] J. ZahradniK, M. Fialova, and V. Linek. The effect of surface-active additives on bubble coalescence in aqueous media. *Chemical Engineering Science*, 54(21):4757–4766, 1999. ISSN 0009-2509. doi: 10.1016/s0009-2509(99)00192-x. URL https://dx.doi.org/10.1016/S0009-2509(99)00192-X.

[40] D. Stegeman, P. A. Knop, A. J. G. Wijnands, and K. R. Westerterp. Interfacial Area and Gas Holdup in a Bubble Column Reactor at Elevated Pressures. *Industrial & Engineering Chemistry Research*, 35 (11):3842–3847, January 1996. ISSN 0888-5885. doi: 10.1021/ie960325h. URL https://doi.org/10.1021/ie960325h. Publisher: American Chemical Society.

[41] R. Krishna, M. I. Urseanu, and A. J. Dreher. Gas hold-up in bubble columns: influence of alcohol addition versus operation at elevated pressures. *Chemical Engineering and Processing: Process Intensification*, 39(4):371–378, 2000. ISSN 0255-2701. doi: 10.1016/s0255-2701(00)00093-3. URL https://dx.doi.org/10.1016/S0255-2701(00)00093-3.

[42] S. A. Shchukarev and T. A. Tolmacheva. Solubility of oxygen in ethanol ? Water mixtures. *Journal of Structural Chemistry*, 9(1):16–21, 1968. ISSN 0022-4766. doi: 10.1007/bf00744018. URL https://dx.doi.org/10.1007/BF00744018.

[43] Giorgio Besagni, Fabio Inzoli, Giorgia De Guido, and Laura Annamaria Pellegrini. The dual effect of viscosity on bubble column hydrodynamics. *Chemical Engineering Science*, 158:509–538, February 2017. ISSN 0009-2509. doi: 10.1016/j.ces.2016.11.003. URL https://www.sciencedirect.com/science/article/pii/S000925091630584X.

[44] Stoyan Nedeltchev, Sara Marchini, Markus Schubert, and Mark W. Hlawitschka. Novel Identifier of Transitions in Bubble Columns Operated with Water and Aqueous Alcohol Solutions - Nedeltchev - 2023 - Chemical Engineering & Technology - Wiley Online Library, 2023. URL https://onlinelibrary.wiley.com/doi/epdf/10.1002/ceat.202300095.

[45] P. Basarova, J. Pislova, J. Mills, and S. Orvalho. Influence of molecular structure of alcohol-water mixtures on bubble behaviour and bubble surface mobility. *Chemical Engineering Science*, 192:74–84, December 2018. ISSN 0009-2509. doi: 10.1016/j.ces.2018.07.008. URL https://www.sciencedirect.com/science/article/pii/S0009250918304731.

[46] M. Zlokarnik. Coalescence phenomena in the gas/liquid system and their influence on oxygen uptake in biological waste water treatment. *Korrespondenz Abwasser*, 27(11):728–736, 1980. ISSN 03411478.

[47] Anthony Lefebvre, Yann Mezui, Martin Obligado, Stéphane Gluck, and Alain Cartellier. A new, optimized Doppler optical probe for phase detection, bubble velocity and size measurements: Investigation of a bubble column operated in the heterogeneous regime. *Chemical Engineering Science*, 250:117359, March 2022. ISSN 0009-2509. doi: 10.1016/j.ces.2021.117359. URL https://www.sciencedirect.com/science/article/pii/S0009250921009246.

[48] International Atomic Energy Agency. Industrial Process Gamma Tomography. Technical Report 978–920–0–104508–9, IAEA, Vienna, Austria, 2008.

[49] F. Fischer and U. Hampel. Ultra fast electron beam X-ray computed tomography for two-phase flow measurement. *Nuclear Engineering and Design*, 240(9):2254–2259, September 2010. ISSN 0029-5493. doi: 10.1016/j.nucengdes.2009.11.016. URL https://www.sciencedirect.com/science/article/pii/S0029549309005755.

[50] Thorsten M. Buzug. *Computed Tomography: From Photon Statistics to Modern Cone-Beam CT*. Springer Berlin Heidelberg, Berlin, Heidelberg, 2008. ISBN 978-3-540-39407-5 978-3-540-39408-2. doi: 10.1007/978-3-540-39408-2.

[51] T. C. Chandrasekera, A. Wang, D. J. Holland, Q. Marashdeh, M. Pore, F. Wang, A. J. Sederman, L. S. Fan, L. F. Gladden, and J. S. Dennis. A comparison of magnetic resonance imaging and electrical capacitance tomography: An air jet through a bed of particles. *Powder Technology*, 227: 86–95, September 2012. ISSN 0032-5910. doi: 10.1016/j.powtec.2012.03.005. URL https://www.sciencedirect.com/science/article/pii/S0032591012001593.

[52] Christian Hansen, Jakob Sauer Jorgensen, and William R.B. Lionheart. *Computed Tomography: Algorithms, Insight and Just Enough Theory*. 2021. URL https://books.google.nl/books?id=Ja5wzgEACAAJ.

[53] Adriaan BM Graas, Evert C Wagner, Tristan van Leeuwen, J Ruud van Ommen, K Joost Batenburg, Felix Lucka, and Luis M Portela. X-ray tomography for fully-3D time-resolved reconstruction of bubbling fluidized beds. *Powder Technology*, 434:119269, 2024. ISSN 0032-5910.

[54] Jens Gregor and Thomas Benson. Computational Analysis and Improvement of SIRT. *IEEE Transactions on Medical Imaging*, 27(7):918–924, July 2008. ISSN 1558-254X. doi: 10.1109/TMI.2008.923696. URL https://ieeexplore.ieee.org/abstract/document/4492754.

[55] Nondestructive Evaluation Physics : X-Ray, . URL https://www.nde-ed.org/Physics/X-Ray/attenuation.xhtml.

[56] Martina Fuss, Antonio Muñoz Roldan, J. Oller, F. Blanco, Paulo Limão-Vieira, Carlos Cabrerizo, Mayerlis Tellez, M. Hubin-Fraskin, Kate Nixon, M. Brunger, and Gustavo Garcia. Modelling low energy electron interactions for biomedical uses of radiation. *Xxvi International Conference on Photonic, Electronic and Atomic Collisions*, 194, November 2009. doi: 10.1088/1742-6596/194/1/012028.

[57] Joseph J. Lifton. *The influence of scatter and beam hardening in X-ray computed tomography for dimensional metrology*. phd, University of Southampton, April 2015. URL https://eprints.soton.ac.uk/378342/.

[58] O.M.H. Ahmed and YuShou Song. A Review of Common Beam Hardening Correction Methods for Industrial X-ray Computed Tomography. *Sains Malaysiana*, 47(8):1883–1890, August 2018. ISSN 01266039. doi: 10.17576/jsm-2018-4708-29.

[59] Shiras Abdurahman, Robert Frysch, Richard Bismark, Steffen Melnik, Oliver Beuing, and Georg Rose. Beam Hardening Correction Using Cone Beam Consistency Conditions. *IEEE transactions on medical imaging*, 37(10):2266–2277, October 2018. ISSN 1558-254X. doi: 10.1109/TMI.2018.2840343.

[60] Jeremy L. Hubers, Alex C. Striegel, Theodore J. Heindel, Joseph N. Gray, and Terrence C. Jensen. X-ray computed tomography in large bubble columns. *Chemical Engineering Science*, 60(22): 6124–6133, November 2005. ISSN 0009-2509. doi: 10.1016/j.ces.2005.03.038. URL https://www.sciencedirect.com/science/article/pii/S0009250905002794.

[61] G. T. Herman. Correction for beam hardening in computed tomography. *Physics in Medicine & Biology*, 24(1):81, January 1979. ISSN 0031-9155. doi: 10.1088/0031-9155/24/1/008. URL https://dx.doi.org/10.1088/0031-9155/24/1/008.

[62] AccuDyne Test. Surface tension, hansen solubility parameters, molar volume, enthalpy of evaporation, and molecular weight of selected liquids (sort by surface tension). URL https://www.accudynetest.com.

[63] Mousarreza Abroodi, Ahmad Bagheri, and Bibi Marzieh Razavizadeh. Surface Tension of Binary and Ternary Systems Containing Monoethanolamine (MEA), Water and Alcohols (Methanol, Ethanol, and Isopropanol) at 303.15 K. *Journal of Chemical & Engineering Data*, 65(6):3173–3182, June 2020. ISSN 0021-9568. doi: 10.1021/acs.jced.0c00192. URL https://doi.org/10.1021/acs.jced.0c00192. Publisher: American Chemical Society.

[64] Maria Grübner. Seamless transfer of a compendial LC method for impurity analysis of chlorhexidine from an UltiMate 3000 Standard HPLC system to a Vanquish Core HPLC system, 2020.

[65] Bubble Pressure Tensiometer-BPT Mobile, . URL https://www.kruss-scientific.com/en/products-services/products/bpt-mobile.

[66] G Besagni, F Inzoli, T Zieghenein, and D Lucas. Experimental study of liquid velocity profiles in large-scale bubble columns with particle tracking velocimetry. *Journal of Physics: Conference Series*, 1224(1):012036, May 2019. ISSN 1742-6596. doi: 10.1088/1742-6596/1224/1/012036. URL https://dx.doi.org/10.1088/1742-6596/1224/1/012036. Publisher: IOP Publishing.

[67] P. Maximiano Raimundo, A. Cloupet, A. Cartellier, D. Beneventi, and F. Augier. Hydrodynamics and scale-up of bubble columns in the heterogeneous regime: Comparison of bubble size, gas holdup and liquid velocity measured in 4 bubble columns from 0.15 m to 3 m in diameter. *Chemical Engineering Science*, 198:52–61, April 2019. ISSN 0009-2509. doi: 10.1016/j.ces.2018.12.043. URL https://www.sciencedirect.com/science/article/pii/S0009250919300612.

[68] G. A. Hughmark. Holdup and Mass Transfer in Bubble Columns. *Industrial & Engineering Chemistry Process Design and Development*, 6(2):218–220, April 1967. ISSN 0196-4305, 1541-5716. doi: 10.1021/i260022a011. URL https://pubs.acs.org/doi/abs/10.1021/i260022a011.

[69] Sailesh B Kumar, Davood Moslemian, and Milorad P Duduković. Gas-holdup measurements in bubble columns using computed tomography. *AIChE Journal*, 43(6):1414–1425, 1997. ISSN 0001-1541.

[70] H. Hikita and H. Kikukawa. Liquid-phase mixing in bubble columns: Effect of liquid properties. *The Chemical Engineering Journal*, 8(3):191–197, January 1974. ISSN 0300-9467. doi: 10.1016/0300-9467(74)85024-0. URL https://www.sciencedirect.com/science/article/pii/0300946774850240.

[71] H. Hikita, S. Asai, K. Tanigawa, K. Segawa, and M. Kitao. Gas hold-up in bubble columns. *The Chemical Engineering Journal*, 20(1):59–67, January 1980. ISSN 0300-9467. doi: 10.1016/0300-9467(80)85006-4. URL https://www.sciencedirect.com/science/article/pii/0300946780850064.

[72] A correlation for gas holdup in turbulent coalescing bubble columns - Reilly - 1986 - The Canadian Journal of Chemical Engineering - Wiley Online Library, . URL https://onlinelibrary.wiley.com/doi/abs/10.1002/cjce.5450640501.

[73] Arsam Behkish, Romain Lemoine, Rachid Oukaci, and Badie I. Morsi. Novel correlations for gas holdup in large-scale slurry bubble column reactors operating under elevated pressures and temperatures. *Chemical Engineering Journal*, 115(3):157–171, January 2006. ISSN 1385-8947. doi: 10.1016/j.cej.2005.10.006. URL https://www.sciencedirect.com/science/article/pii/S1385894705003633.

[74] A. D. Anastasiou, N. A. Kazakis, A. A. Mouza, and S. V. Paras. Effect of organic surfactant additives on gas holdup in the pseudo-homogeneous regime in bubble columns equipped with fine pore sparger. *Chemical Engineering Science*, 65(22):5872–5880, November 2010. ISSN 0009-2509. doi: 10.1016/j.ces.2010.08.011. URL https://www.sciencedirect.com/science/article/pii/S0009250910004781.

[75] S. Azizi, A. Yadav, Y.M. Lau, U. Hampel, S. Roy, and M. Schubert. Hydrodynamic correlations for bubble columns from complementary UXCT and RPT measurements in identical geometries and conditions. *Chemical Engineering Science*, 208:115099, November 2019. ISSN 00092509. doi: 10.1016/j.ces.2019.07.017. URL https://linkinghub.elsevier.com/retrieve/pii/S0009250919305810.

[76] Behnoosh Moshtari, Ensieh Ganji Babakhani, and Jafar Sadegh Moghaddas. Experimental study of gas hold-up and bubble behavior in gas-liquid bubble column. *Petroleum & Coal*, 51(1):27–32, 2009.

[77] Akhilesh Kumar, T. E. Degaleesan, G. S. Laddha, and H. E. Hoelscher. Bubble swarm characteristics in bubble columns. *The Canadian Journal of Chemical Engineering*, 54(5):503–508, 1976. ISSN 1939-019X. doi: 10.1002/cjce.5450540525. URL https://onlinelibrary.wiley.com/doi/abs/10.1002/cjce.5450540525. _eprint: https://onlinelibrary.wiley.com/doi/pdf/10.1002/cjce.5450540525.

[78] Korekazu Ueyama and Terukatsu Miyauchi. Properties of recirculating turbulent two phase flow in gas bubble columns. *AIChE Journal*, 25(2):258–266, 1979. ISSN 1547-5905. doi: 10.1002/aic.690250207. URL https://onlinelibrary.wiley.com/doi/abs/10.1002/aic.690250207. _eprint: https://onlinelibrary.wiley.com/doi/pdf/10.1002/aic.690250207.

[79] Carolin Bokelmann, Jason Bromley, and Ralf Takors. Pros and cons of airlift and bubble column bioreactors: How internals improve performance.

[80] Wiebke Drenckhan and Arnaud Saint-Jalmes. The science of foaming. *Advances in Colloid and Interface Science*, 222:228–259, August 2015. ISSN 0001-8686. doi: 10.1016/j.cis.2015.04.001. URL https://www.sciencedirect.com/science/article/pii/S0001868615000603.

[81] Sven van den Heuvel. Hydrodynamic Forces Acting on Vertically Rising Bubbles. 2023.

[82] U Veera. Effect of superficial gas velocity on gas hold-up profiles in foaming liquids in bubble column reactors. *Chemical Engineering Journal*, 99(1):53–58, May 2004. ISSN 13858947. doi: 10.1016/j.cej.2003.09.003. URL https://linkinghub.elsevier.com/retrieve/pii/S1385894703002547.

[83] Yuanxin Wu, Boon Cheng Ong, and M. H. Al-Dahhan. Predictions of radial gas holdup profiles in bubble column reactors. *Chemical Engineering Science*, 56(3):1207–1210, February 2001. ISSN 0009-2509. doi: 10.1016/S0009-2509(00)00341-9. URL https://www.sciencedirect.com/science/article/pii/S0009250900003419.

[84] B. Hohermuth, M. Kramer, S. Felder, and D. Valero. Velocity bias in intrusive gas-liquid flow measurements. *Nature Communications*, 12(1):4123, July 2021. ISSN 2041-1723. doi: 10.1038/s41467-021-24231-4. URL https://www.nature.com/articles/s41467-021-24231-4. Publisher: Nature Publishing Group.

[85] Yu Ma, Yangrui Zhang, Song Li, Weimin Sun, and Elfed Lewis. Influence of Bubble Deformation on the Signal Characteristics Generated Using an Optical Fiber Gas–liquid Two-Phase Flow Sensor. *Sensors*, 21(21):7338, January 2021. ISSN 1424-8220. doi: 10.3390/s21217338. URL https://www.mdpi.com/1424-8220/21/21/7338. Number: 21 Publisher: Multidisciplinary Digital Publishing Institute.

[86] Diego Rosso, Derry L. Huo, and Michael K. Stenstrom. Effects of interfacial surfactant contamination on bubble gas transfer. *Chemical Engineering Science*, 61(16):5500–5514, August 2006. ISSN 0009-2509. doi: 10.1016/j.ces.2006.04.018. URL https://www.sciencedirect.com/science/article/pii/S0009250906002648.

[87] Haibo Jin, Suohe Yang, Zhiwu Guo, Guangxiang He, and Zemin Tong. The axial distribution of holdups in an industrial-scale bubble column with evaluated pressure using gamma-ray attenuation approach. *Chemical Engineering Journal*, 115(1):45–50, December 2005. ISSN 1385-8947. doi: 10.1016/j.cej.2005.09.003. URL https://www.sciencedirect.com/science/article/pii/S1385894705003037.

[88] Chun-Kai Gong, Xiao Xu, and Qiang Yang. Gas holdup at dynamic equilibrium region of a bubble column: Effect of bubble generator performance. *Chemical Engineering Journal*, 443:136382, September 2022. ISSN 1385-8947. doi: 10.1016/j.cej.2022.136382. URL https://www.sciencedirect.com/science/article/pii/S1385894722018770.

[89] Mass transfer and drag coefficients of bubbles rising in dilute aqueous solutions - Raymond - 1971 - AIChE Journal - Wiley Online Library, . URL https://aiche.onlinelibrary.wiley.com/doi/10.1002/aic.690170114.

[90] Pisut Painmanakul, Karine Loubière, Gilles Hébrard, Martine Mietton-Peuchot, and Michel Roustan. Effect of surfactants on liquid-side mass transfer coefficients. *Chemical Engineering Science*, 60(22):6480–6491, November 2005. ISSN 0009-2509. doi: 10.1016/j.ces.2005.04.053. URL https://www.sciencedirect.com/science/article/pii/S0009250905003180.

[91] Reinhard Strey, Yrjö Viisanen, Makoto Aratono, Josip P. Kratohvil, Qi Yin, and Stig E. Friberg. On the Necessity of Using Activities in the Gibbs Equation. *The Journal of Physical Chemistry B*, 103(43):9112–9116, October 1999. ISSN 1520-6106. doi: 10.1021/jp990306w. URL https://doi.org/10.1021/jp990306w. Publisher: American Chemical Society.

[92] Chi M. Phan, Cuong V. Nguyen, and Thuy T. T. Pham. Molecular Arrangement and Surface Tension of Alcohol Solutions. *The Journal of Physical Chemistry B*, 120(16):3914–3919, April 2016. ISSN 1520-6106. doi: 10.1021/acs.jpcb.6b01209. URL https://doi.org/10.1021/acs.jpcb.6b01209. Publisher: American Chemical Society.

[93] Ahmad Bagheri, Mostafa Fazli, and Malihe Bakhshaei. Surface properties and surface thickness of aqueous solutions of alcohols. *Journal of Molecular Liquids*, 224:442–451, December 2016. ISSN 0167-7322. doi: 10.1016/j.molliq.2016.09.113. URL https://www.sciencedirect.com/science/article/pii/S0167732215311302.

[94] Magdalena Bielawska and Anna Zdziennicka. Ethanol behaviour at the solution-air interface in the presence of Triton X-100 and cetyltrimethylammonium bromide mixture. *Annales UMCS, Chemia*, 70(1), January 2015. ISSN 2083-358X. doi: 10.1515/umcschem-2015-0011. URL http://archive.sciendo.com/UMCSCHEM/umcschem.2015.70.issue-1/umcschem-2015-0011/umcschem-2015-0011.pdf.

A Chemicals Used in Experiments

Table 7: *Properties of pure compounds and stock solutions for various chemicals.*

Property	Ethanol	Iso-propanol	1-Propanol	1-Butanol	Acetic acid	Lactic acid
Pure compound						
Molar weight (g/mol)	46.007	60.096	60.096	74.12	60.052	90.08
Density (g/l)	789	786	803	810	1049	1209
Surface tension (dynes/cm)	22	23.3	20.9	25	27	¿50
Vapor pressure (hPa)	58.5	44.2	19.3	¡10	15.1	-
Henry coefficient (mol/(m^3Pa))	2.52[1]	1.2[2]	1.4[2]	1.2[2]	40[2]	-
MAC (mg/m^3)	260	500	200	310	25	-
Diffusion coefficient (cm^2/s)	1.23e-5[3]	0.87e-5[4]	1.1e-5[4]	0.77e-5[4]	1.19e-5[4]	-
Stock solution						
Purity (w/w%)	99.5	98	99.5	99.9	99	99.9
Density (g/l)	790	790	804	810	1048	1209
Concentration (g/l)	786	774	800	809	1038	1208

B Maximum concentrations

Table 8: *Maximum concentrations.*

Compound name	Ideal max concentration (mol/l)	Max concentration after foam test (mol/l)	Actual max target concentration (mol/l)	Measured concentration (mol/l)
Ethanol	2,2	0,72	0,62	0,597
Propanol	1,1	0,36	0,36	0,343
Iso-propanol	1,1	0,36	0,67	0,672
1-Butanol	0.54	0.18	0.26	0,254
Acetic acid	0,22	0,07	0,22	0,222
Lactic acid	0,11	0,04	0,11	0,008

C Concentration Series

Table 9: *Properties of ethanol samples measured at* $U_g = 0.05$ *m/s*

id	Concentration (g/l)	Gas Holdup	ρ_l (kg/m^3)	η_l (mPa s)	σ (mN/m)	Ma	Fr	Bo	Ga	Pe
EtOH_C1_1	0,0	0,11	997,98	0,955	72,87	n/a	n/a	n/a	n/a	n/a
EtOH_C2_1	5,0	0,14	997,05	0,973	70,29	1245	0,252	2,224	811,6	2381
EtOH_C2_2	4,9	0,14	997,05	0,973	70,46	1223	0,252	2,218	811,6	2381
EtOH_C3_1	9,4	0,14	996,21	0,991	67,26	1749	0,252	2,322	796,5	2381
EtOH_C3_2	9,6	0,14	996,20	0,992	67,34	1763	0,252	2,319	796,1	2381
EtOH_C4_1	14,1	0,15	995,35	1,010	65,33	2163	0,252	2,389	781,0	2381
EtOH_C4_2	14,2	0,15	995,36	1,010	65,33	2171	0,252	2,388	780,8	2381
EtOH_C4_3	13,6	0,15	995,41	1,008	65,78	2123	0,252	2,372	782,1	2381
EtOH_C5_1	18,5	0,15	994,56	1,028	63,66	2503	0,252	2,449	766,6	2381
EtOH_C5_2	18,4	0,15	994,58	1,028	63,99	2487	0,252	2,436	766,8	2381
EtOH_C6_1	23,2	0,15	993,71	1,048	61,91	2816	0,252	2,516	751,5	2381
EtOH_C6_2	23,1	0,15	993,74	1,047	62,28	2806	0,252	2,501	752,1	2381
EtOH_C7_1	27,5	0,15	992,97	1,066	60,58	3077	0,252	2,570	738,2	2381
EtOH_C7_2	27,1	0,15	993,18	1,094	60,43	3002	0,252	2,577	719,0	2381

Table 10: *Properties of n-propanol samples measured at* $U_g = 0.05$ *m/s*

id	Concentration (g/l)	Gas Holdup	ρ_l (kg/m^3)	η_l (mPa s)	σ (mN/m)	Ma	Fr	Bo	Ga	Pe
PrOH_C1_1	0,0	0,11	998,03	0,954	72,78	n/a	n/a	n/a	n/a	n/a
PrOH_C1_2	0,0	0,11	998,03	0,954	72,86	n/a	n/a	n/a	n/a	n/a
PrOH_C2_1	3,1	0,13	997,49	0,967	68,87	802	0,252	2,271	817,1	1818
PrOH_C2_2	3,2	0,13	997,49	0,968	68,70	822	0,252	2,276	816,2	1818
PrOH_C3_1	6,4	0,13	996,94	0,981	65,02	2148	0,252	2,404	804,9	1818
PrOH_C3_2	6,3	0,13	996,95	0,981	64,65	2140	0,252	2,417	805,2	1818
PrOH_C4_1	9,2	0,13	996,46	0,994	62,76	3291	0,252	2,489	794,3	1818
PrOH_C4_2	9,2	0,13	996,47	0,993	62,32	3280	0,252	2,507	795,0	1818
PrOH_C5_1	12,2	0,14	995,96	1,007	59,48	4315	0,252	2,625	783,8	1818
PrOH_C5_2	12,1	0,14	995,98	1,007	59,45	4292	0,252	2,626	784,0	1818
PrOH_C5_3	12,0	0,14	996,01	1,006	59,87	4243	0,252	2,608	784,6	1818
PrOH_C6_1	15,1	0,15	995,48	1,020	57,75	5146	0,252	2,702	773,2	1818
PrOH_C6_2	15,1	0,15	995,50	1,020	57,39	5143	0,252	2,719	773,2	1818
PrOH_C7_1	17,4	0,15	995,11	1,031	56,59	5670	0,252	2,757	764,8	1818
PrOH_C7_2	17,4	0,15	995,11	1,031	56,16	5676	0,252	2,778	765,0	1818
PrOH_C8_1	20,6	0,16	994,60	1,045	54,22	6277	0,252	2,876	753,9	1818
PrOH_C8_2	20,4	0,16	994,62	1,045	54,29	6251	0,252	2,872	754,3	1818

Table 11: *Properties of iso-propanol samples measured at* $U_g = 0.05$ *m/s*

id	Concentration (g/l)	Gas Holdup	ρ_l (kg/m^3)	η_l (mPa s)	σ (mN/m)	Ma	Fr	Bo	Ga	Pe
IPA_C1_1	0,0	0,11	998,032	0,954	73,04	n/a	n/a	n/a	n/a	n/a
IPA_C2_1	3,3	0,15	997,43	0,969	68,72	267	0,252	2,276	816,0	2299
IPA_C2_2	3,2	0,15	997,44	0,969	68,29	260	0,252	2,290	816,0	2299
IPA_C3_1	9,5	0,16	996,27	0,997	62,44	3614	0,252	2,501	791,8	2299
IPA_C3_2	9,5	0,16	996,27	0,997	62,44	3612	0,252	2,501	791,8	2299
IPA_C4_1	12,6	0,16	995,71	1,011	60,56	5099	0,252	2,578	780,1	2299
IPA_C4_2	12,5	0,16	995,72	1,011	60,14	5076	0,252	2,596	780,6	2299
IPA_C5_1	15,6	0,16	995,15	1,026	58,12	6340	0,252	2,684	768,4	2299
IPA_C5_2	15,6	0,16	995,16	1,026	58,69	6310	0,252	2,658	768,5	2299
IPA_C6_1	18,0	0,16	994,69	1,040	56,72	7160	0,252	2,749	758,2	2299
IPA_C6_2	17,9	0,16	994,71	1,039	56,74	7132	0,252	2,748	758,7	2299
IPA_C7_1	21,1	0,16	994,20	1,053	55,92	7958	0,252	2,787	748,3	2299
IPA_C7_2	20,7	0,16	994,22	1,052	55,42	7902	0,252	2,812	748,7	2299
IPA_C8_1	40,4	0,17	990,83	1,159	48,55	9925	0,252	3,199	677,4	2299
IPA_C8_2	39,9	0,17	991,01	1,153	48,68	9938	0,252	3,192	680,8	2299

Table 12: *Properties of n-butanol samples measured at* $U_g = 0.05$ *m/s*

id	Concentration (g/l)	Gas Holdup	ρ_l (kg/m^3)	η_l (mPa s)	σ (mN/m)	Ma	Fr	Bo	Ga	Pe
ButOH_C1_1	0,0	0,11	998,03	0,948	72,94	n/a	n/a	n/a	n/a	n/a
ButOH_C2_1	0,7	0,14	997,91	0,958	70,55	40	0,252	2,217	825,6	2597
ButOH_C2_2	0,7	0,14	997,91	0,957	71,12	50	0,252	2,200	826,6	2597
ButOH_C3_1	1,1	0,14	997,84	0,959	69,18	281	0,252	2,261	824,9	2597
ButOH_C3_2	1,1	0,14	997,85	0,959	69,64	240	0,252	2,246	824,7	2597
ButOH_C4_1	1,2	0,14	997,83	0,959	68,70	324	0,252	2,277	824,5	2597
ButOH_C4_2	1,2	0,14	997,82	0,959	68,42	349	0,252	2,286	824,3	2597
ButOH_C4_3	1,2	0,14	997,83	0,959	68,85	355	0,252	2,272	824,3	2597
ButOH_C5_1	1,6	0,13	997,76	0,961	68,45	819	0,252	2,285	822,6	2597
ButOH_C5_2	1,6	0,13	997,76	0,961	68,12	805	0,252	2,296	822,6	2597
ButOH_C6_1	4,2	0,15	997,34	0,973	61,07	5516	0,252	2,560	812,3	2597
ButOH_C6_2	4,2	0,15	997,34	0,972	61,37	5473	0,252	2,548	812,8	2597
ButOH_C7_1	9,3	0,15	996,54	0,995	52,65	10843	0,252	2,967	793,8	2597
ButOH_C7_2	8,9	0,15	996,54	0,994	52,43	10699	0,252	2,980	794,0	2597
ButOH_C8_1	18,8	0,16	995,08	1,038	43,56	10468	0,252	3,581	759,4	2597
ButOH_C8_2	18,6	0,16	995,08	1,038	43,68	10515	0,252	3,571	759,7	2597

Table 13: *Properties of acetic acid samples measured at* $U_g = 0.05$ *m/s*

id	Concentration (g/l)	Gas Holdup	ρ_l (kg/m^3)	η_l (mPa s)	σ (mN/m)	Ma	Fr	Bo	Ga	Pe
AA_C1_1	0,00	0,11	997,31	0,974	73,21	n/a	n/a	n/a	n/a	n/a
AA_C2_1	0,52	0,12	997,51	0,960	73,25	51	0,252	2,135	823,8	1681
AA_C2_2	0,29	0,12	996,45	0,955	73,25	30	0,252	2,133	827,1	1681
AA_C3_1	1,11	0,13	997,07	0,959	72,91	104	0,252	2,144	824,2	1681
AA_C3_2	1,11	0,13	997,28	0,956	72,88	104	0,252	2,145	826,7	1681
AA_C4_1	2,33	0,14	998,32	0,958	72,37	210	0,252	2,163	825,8	1681
AA_C4_2	2,32	0,14	998,32	0,958	72,32	209	0,252	2,164	825,9	1681
AA_C5_1	4,25	0,14	998,59	0,962	71,54	371	0,252	2,188	822,9	1681
AA_C5_2	4,25	0,14	998,59	0,961	71,59	371	0,252	2,187	823,1	1681
AA_C6_1	6,63	0,13	998,94	0,965	70,76	563	0,252	2,213	819,9	1681
AA_C6_2	6,43	0,13	998,94	0,966	70,76	547	0,252	2,213	819,6	1681
AA_C7_1	9,30	0,13	999,35	0,971	69,81	767	0,252	2,244	815,5	1681
AA_C7_2	9,27	0,13	999,35	0,970	69,77	765	0,252	2,245	816,1	1681
AA_C8_1	13,35	0,14	999,91	0,978	68,64	1052	0,252	2,284	810,5	1681
AA_C8_2	13,15	0,14	999,91	0,978	68,55	1039	0,252	2,287	810,5	1681

Table 14: *Properties of lactic acid samples measured at* $U_g = 0.05$ *m/s.*

id	Concentration (g/l)	Gas Holdup	ρ_l (kg/m^3)	η_l (mPa s)	σ (mN/m)	Ma	Fr	Bo	Ga	Pe
LA_C1_1	0,0	0,11	998,03	0,953	72,99	n/a	n/a	n/a	n/a	n/a
LA_C2_1	0,2	0,12	998,05	0,954	72,95	3	0,252	2,145	829,2	2105
LA_C2_2	0,2	0,12	998,05	0,954	72,94	3	0,252	2,145	828,9	2105
LA_C3_1	0,6	0,13	998,18	0,955	72,79	26	0,252	2,150	828,2	2105
LA_C3_2	0,7	0,13	998,18	0,955	72,80	29	0,252	2,150	828,1	2105

D Measurement Times

D.1 Pressure Measurements

The cumulative average voltage signal was calculated for both pressure probes (see Fig. 23). The figure shows that a measuring time of 2 minutes results in a reliable average voltage.

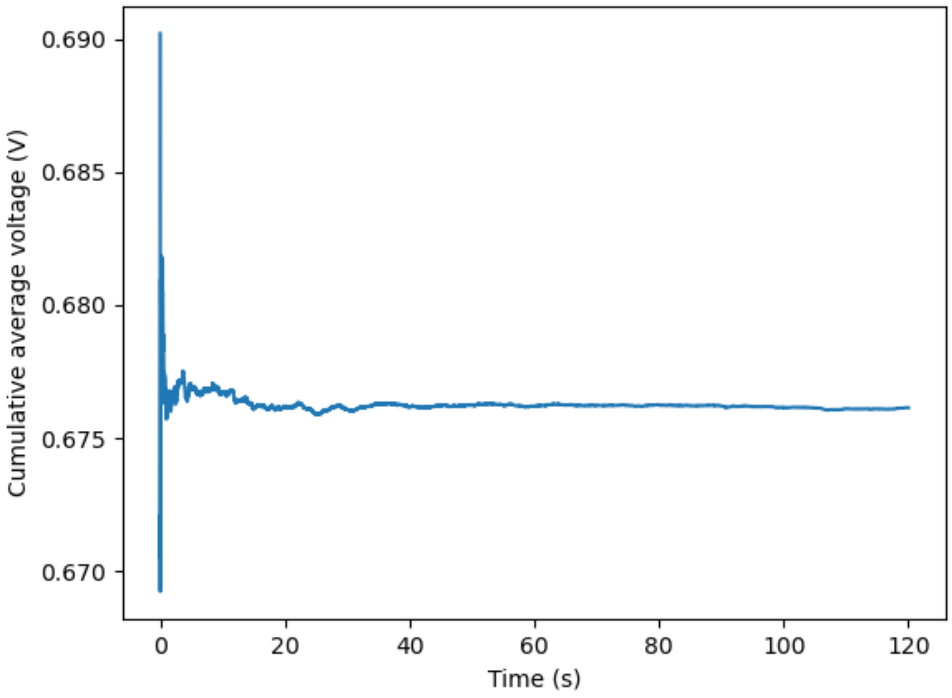

Figure 23: *The cumulative average voltage of the lower pressure probe at a flow-rate of 80 l/min.*

D.2 Scatter Measurements

The average intensity of every pixel on the detector was calculated. After a measurement time of 10 seconds, the cumulative average intensity and the standard error of the mean stabilized (see Fig. 24).

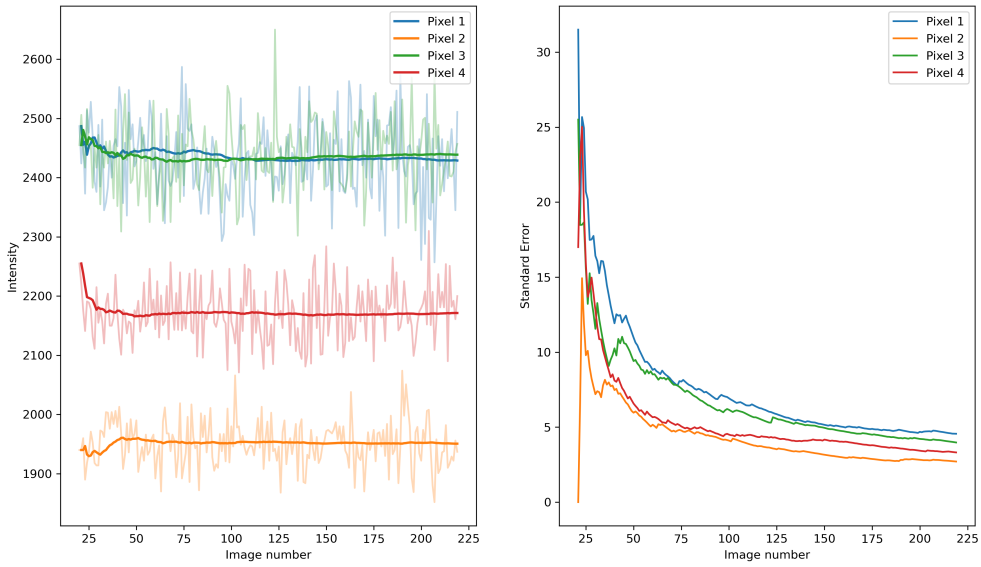

Figure 24: *The pixel intensities of 4 pixels with the corresponding cumulative average (left) and the standard error of the mean (right).*

E Bubble Approach Velocity

The bubble velocities were measured by the optical fiber probe. A matrix was made with all bubbles as column and as rows. The difference in bubble velocity was calulated for every bubble-bubble pair. This resulted in a distribution for the difference in bubble velocity. It can be assumed that the difference in bubble velocity is the approach velocity. However, the velocity of the two bubbles in the direction towards each other is lower than the velocity calculated here. An example of the bubble velocity (Fig. 25) and approach velocity (Fig. 26) are shown below.

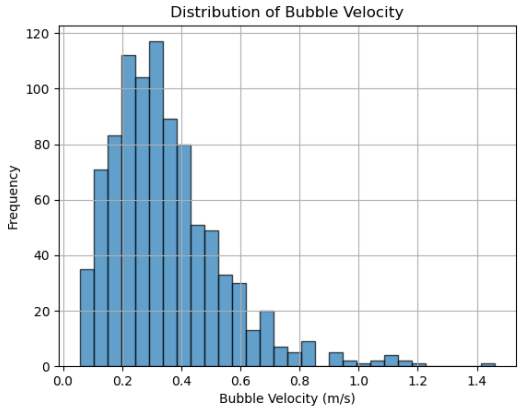

Figure 25: *Bubble velocity distribution in 27 g/l ethanol with a gasflow of 80 l/min.*

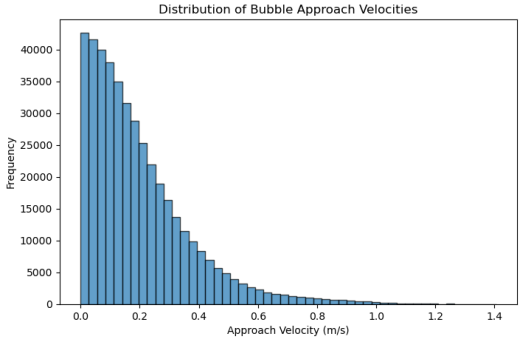

Figure 26: *Bubble approach velocity distribution in 27 g/l ethanol with a gasflow of 80 l/min.*

F Peclet Number

The Peclet number is a constant in the current study. The Peclet number is very sensitive to the choice of the bubble radius. In the current study, a radius of approximately 2 mm is found (see Appendix I). However, a bubble radius of 0.5 mm is mentioned in the paper by Wang et al. [1]. The impact of the bubble radius on 1/Pe is shown in 27. Pe is defined as:

$Pe = \frac{R_{eq}V}{D_l}$

With R_{eq} as the radius of the bubble, V as the approach velocity, and D_l as the diffusion coefficient of the bulk.

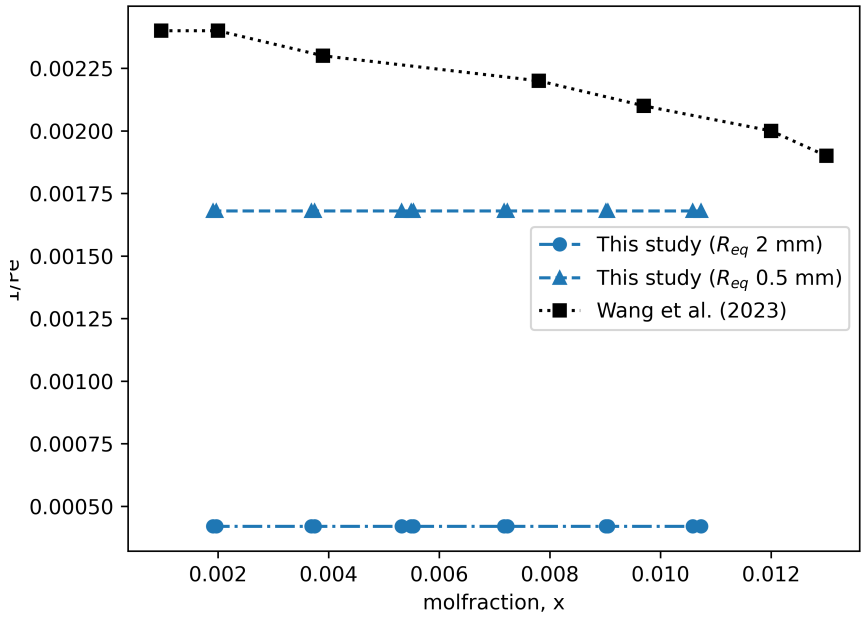

Figure 27: *Comparison between the Pe number from Wang et al. [1] and this study and the effect of bubble radius on the Pe number. A system with with water and ethanol is considered.*

G Surface Tension Measurements

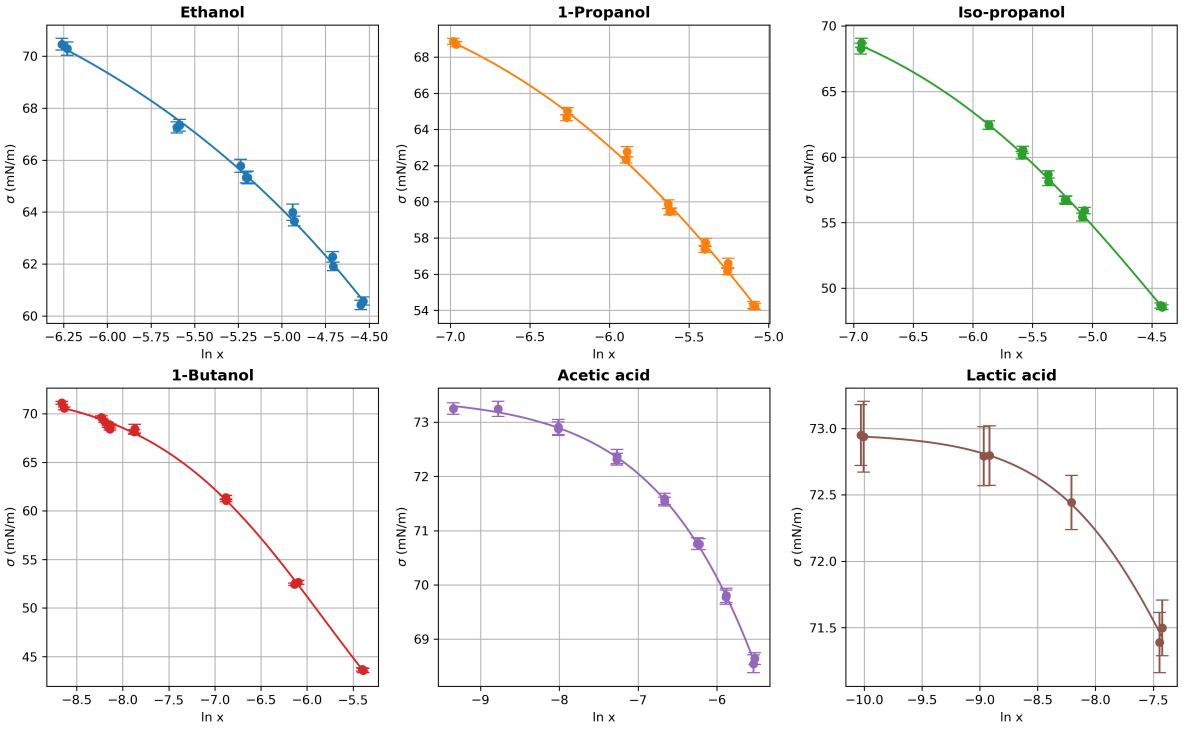

Figure 28: *Surface tension results. The measurements are done for ethanol, n-propanol, iso-proanol, n-butanol, acetic acid and lactic acid.*

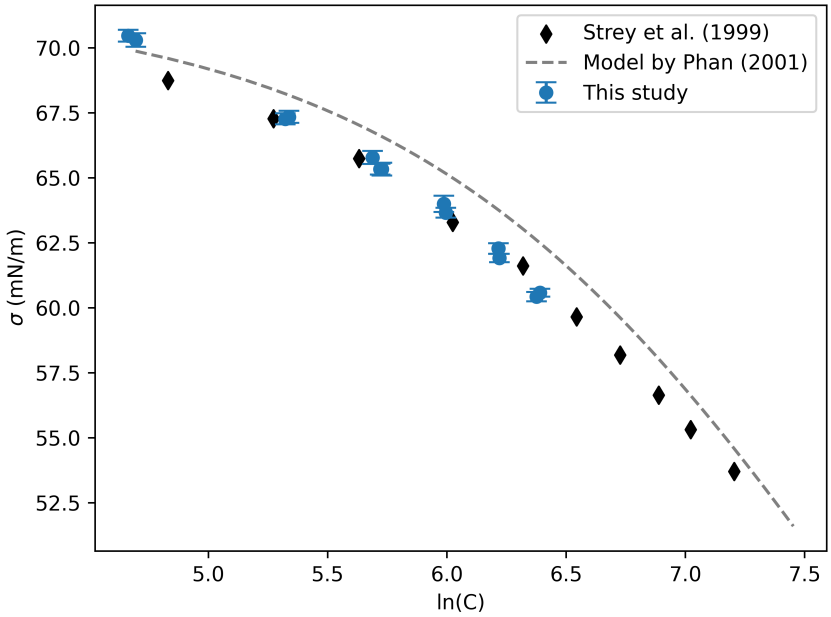

Figure 29: *Surface tension of ethanol compared to literature data from Strey et al. [91] and a surface tension model described by Phan et al. [92].*

H Surface Excess

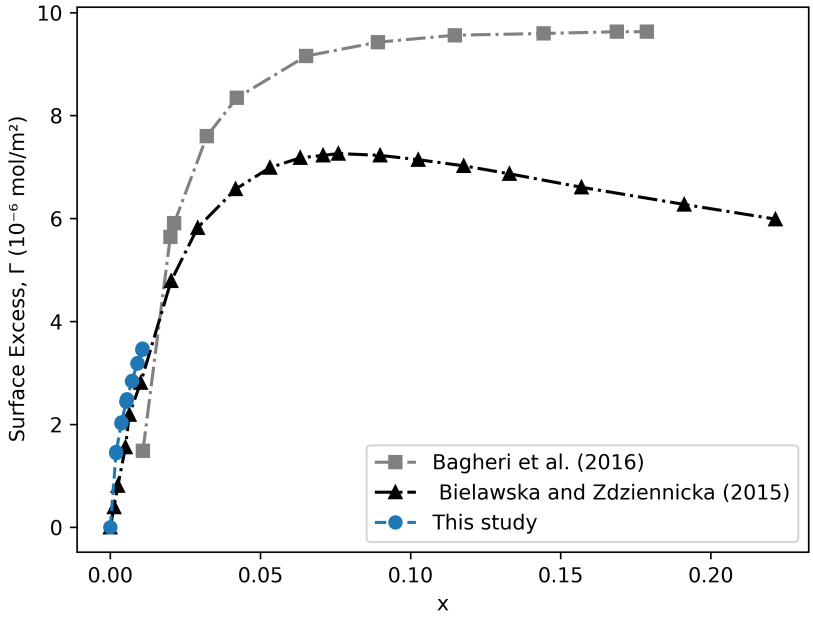

Figure 30: *Comparison of the surface excess of ethanol in water with literature data from Bagheri et al. [93] and Bielawski and Zdziennicka [94].*

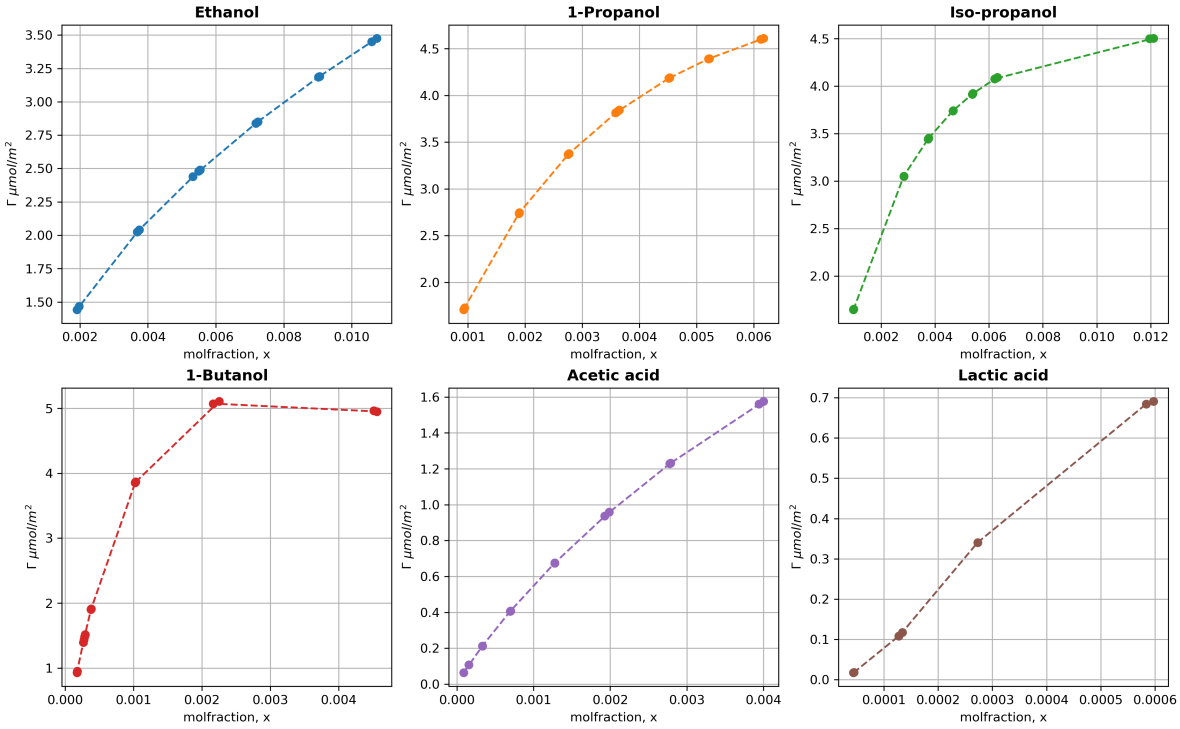

Figure 31: *Surface excess*

I Bubble Size Distribution

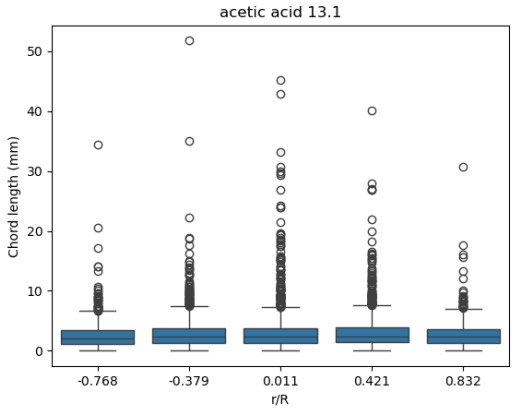

Figure 32: *Bubbles size distribution of 13 g/l acetic acid with gasflow=80 l/min*

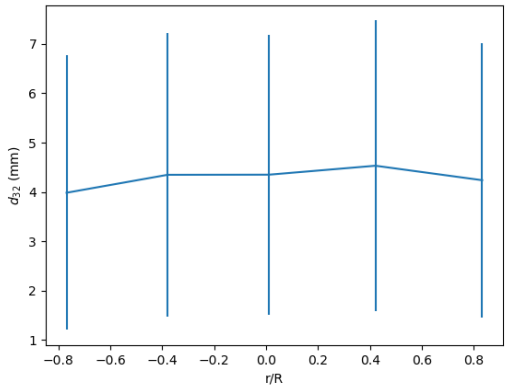

Figure 33: d_{32} *of 13 g/l acetic acid with gasflow=80 l/min*

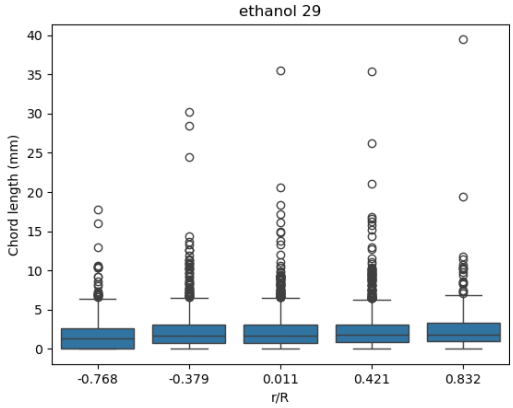

Figure 34: *Bubbles size distribution of 27 g/l ethanol with gasflow=50 l/min*

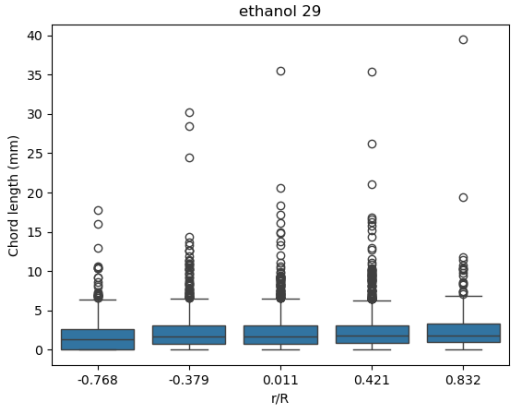

Figure 35: d_{32} *of 27 g/l ethanol with gasflow=80 l/min*

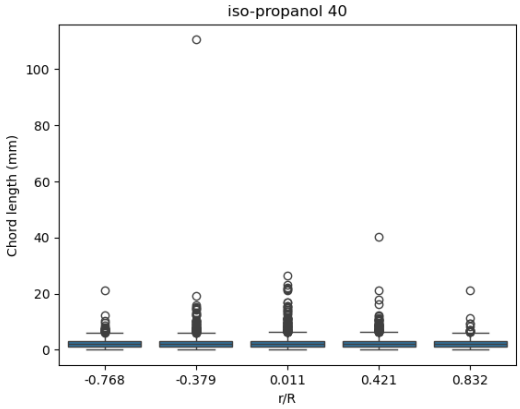

Figure 36: *Bubbles size distribution of 40 g/l iso-propanol with gasflow=80 l/min*

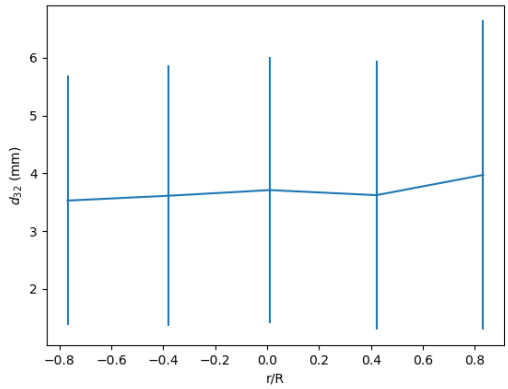

Figure 37: d_{32} *of 40 g/l iso-propanol with gasflow=80 l/min*

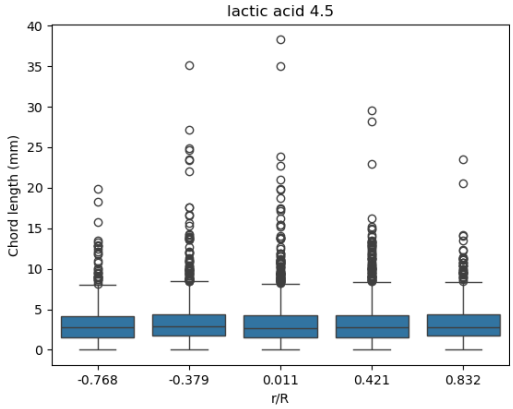

Figure 38: *Bubbles size distribution of 4.5 g/l lactic acid with gasflow=50 l/min*

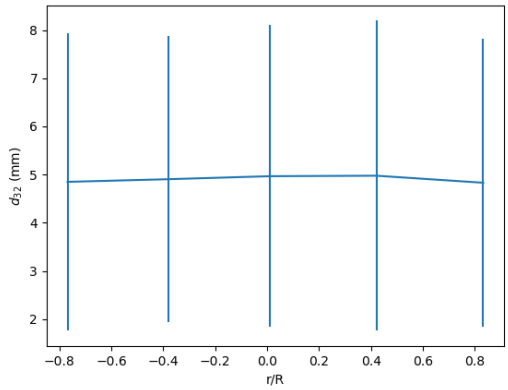

Figure 39: d_{32} *of 4.5 g/l lactic acid with gasflow=50 l/min*

J Sensitivity Analysis Ueyama and Miyauchi

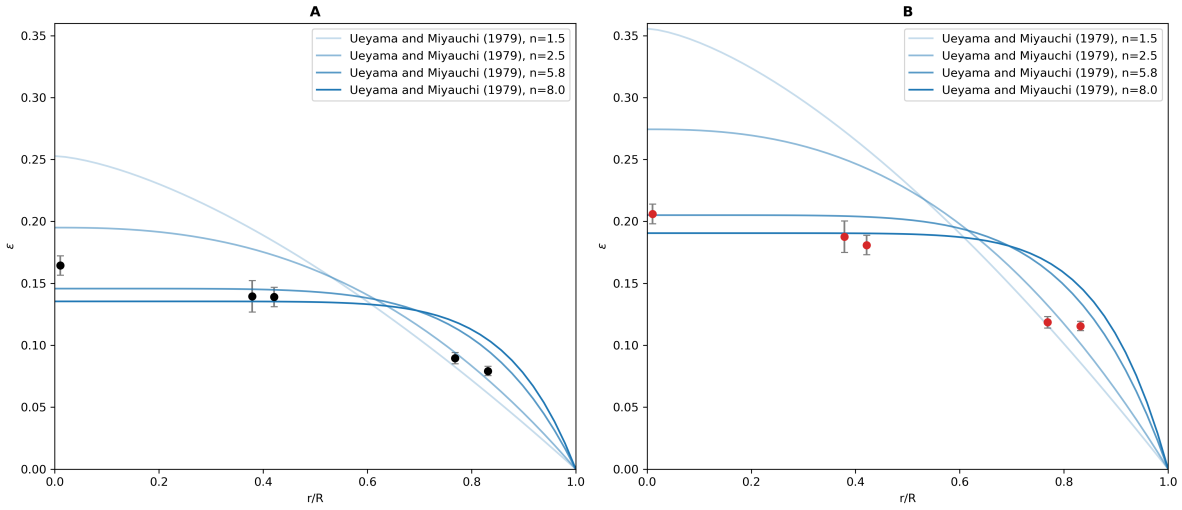

Figure 40: *Sensitivity analysis of changing n in the correlation of Ueyama and Miyauchi (Eq. 24. Error-bars indicate the standard deviation of the measurements on the water-only.) [78].*

K Calculation Mean Holdup

The overall holdup ($\bar{\epsilon}$) is calculated for from a holdup distribution by integrating this profile. The geometry of the column must be taken into account. Therefore, local holdup values close to the wall have a greater impact on the total holdup than holdup values close to the middle of the column. Thus, the global holdup is caluclated according to

$$\bar{\epsilon} = 2 \int_0^1 \epsilon(r) r \, dr \tag{44}$$

It's found by integrating $\epsilon(r)$ over the circular cross-section, weighted by the area element in polar coordinates ($2\pi r \, dr$), and then normalizing by the total area (πR^2).

The radius R is assumed to be 1 (i.e., values are non-dimensionalized):

$$\begin{aligned}
\bar{\epsilon} &= \frac{\int_0^R \epsilon(r) 2\pi \, dr}{\int_0^R 2\pi \, dr} \\
&= \frac{\int_0^1 \epsilon(r) 2\pi \, dr}{2\pi \frac{1}{2}} \\
&= \frac{2\pi \int_0^1 \epsilon(r) \, dr}{\pi} \\
&= 2 \int_0^1 \epsilon(r) r \, dr
\end{aligned}$$

L Dependence of gasflow on Scatter

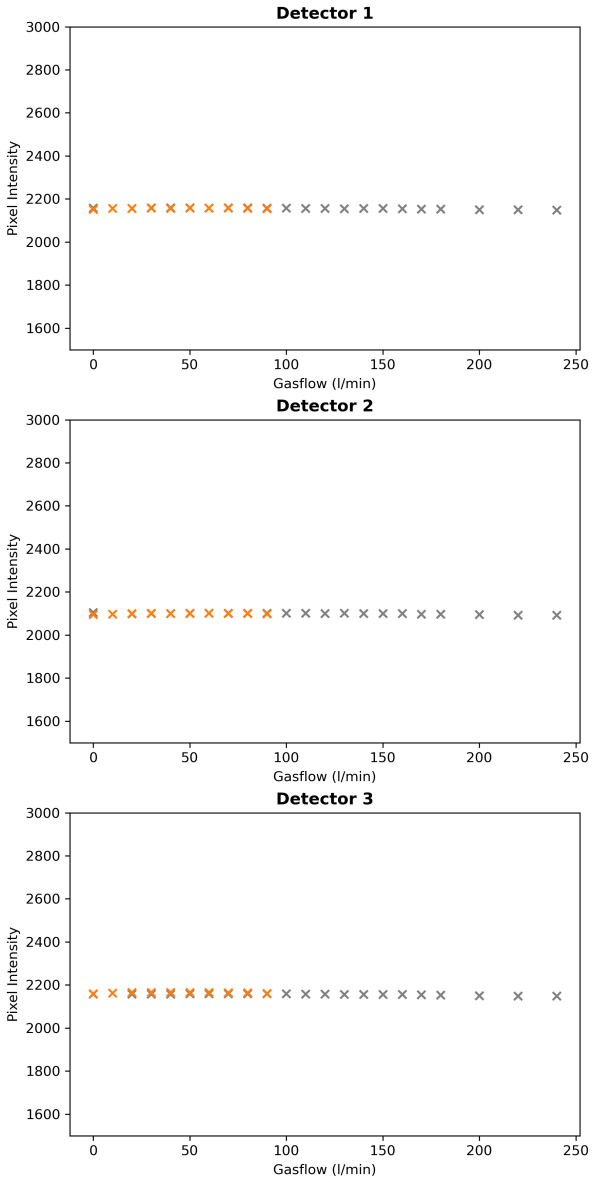

Figure 41: *Dependence of scatter on gasflow for the 3 detectors. The scatter was determined for a column filled with water (gray) and for approximately 20 g/l 1-propanol (orange).*

M Scatter Distribution Detectors

Time averaged intensity values result in a scatter distribution across every detector. Fig. 42 shows that noise from cross-scattering is not equal for the whole detector.

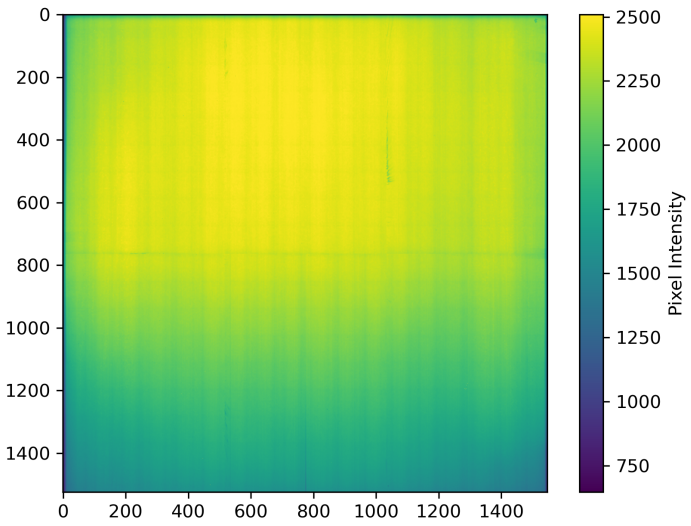

Figure 42: *Pixel intensity for a detector as a result of cross scatter. The figure shows where X-ray from source 1 and 2 hit detector 3.*

N Image Corrections Comparison

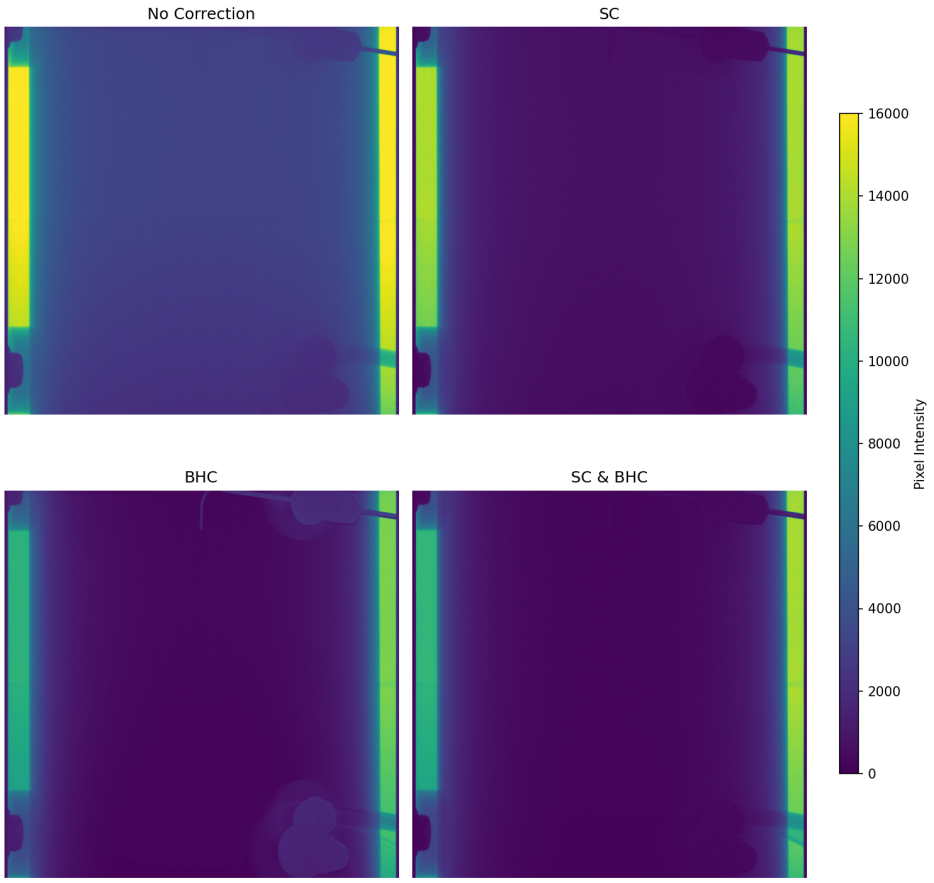

Figure 43: *The effect of the different corrections on the 2D images. An image without correction (No Correction) is compared with an image with scatter correction (SC), with beam hardening correction (BHC) and with both scatter correction and beam hardening correction (SC & BHC).*

O Impact of Inaccurate Geometry

The calibration of the X-ray setup was conducted as explained in Chapter 3.4.1. Since, the column was turned a full 360 degrees, a high resolution reconstruction was made of the empty BCR. The reconstruction of the column during calibration did not show any artifacts. So, it was concluded that the calibration was done correctly.

The distance an X-ray beam travels through the BCR before reaching the detector was calculated using the method described in Chapter 3.4.2. The distance of an X-ray through the column is shown in Fig. 44. The X-ray beams hitting the sides of the detector do not go through the column (Fig. 44, $x = 0$). Photons measured in the middle of the detector traveled a long distance through the column (Fig. 44, high values x).

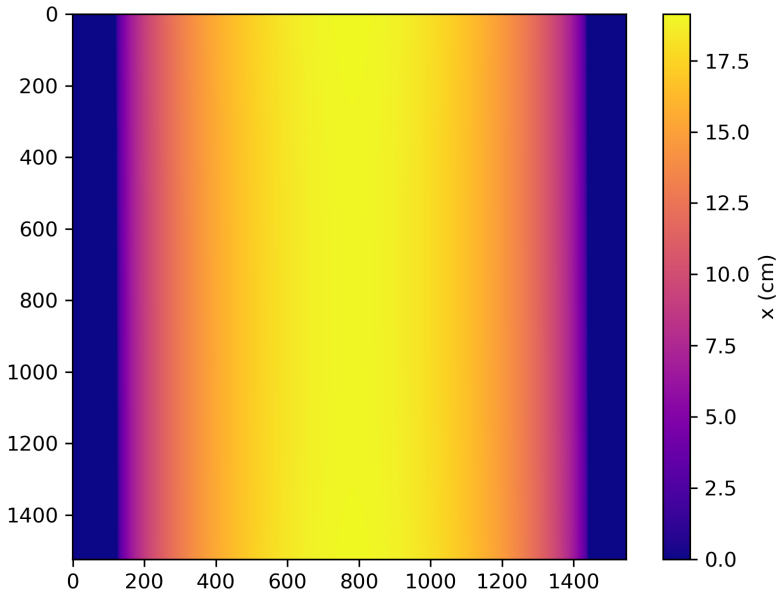

Figure 44: *The calculated distance for each pixel. The distance an X-ray beam travels through the column when it moves in a straight line from the source to the detector. This is an example for detector 1.*

The location of the column walls are calculated using the method described in Chapter 3.4.2 does not align with the actual column walls. Specifically, the distances calculated for the left side of the detectors do not align (see Fig. 45).

The effect of the misalignment is visible in Fig. 46 for all three detectors. When the measured intensity of the full column ($I(x)$) is larger than the intensity of that same pixel in the measurement of the empty column I_{empty}, then $-\ln\left(\frac{I(x)}{I_{empty}}\right)$ becomes negative (Fig. 46, "Not corrected"). The pixel intensity ($I(x)$) is higher for the "not corrected" data when the X-ray beam should not go through the column at all. However, noise from scatter is more abundant in a column filled with water. Therefore, the $I(x)$ is higher for the "not corrected" data resulting a negative $-\ln\left(\frac{I(x)}{I_{empty}}\right)$.

Fig. 46 "Detector 1" shows that the beam hardening correction works for both sides of the detector almost equally well. This is because the calculated path lengths of the X-ray beams through the column are all within the inner diameter of the column (Fig. 45, Detector 1). Detector 3 shows clearly the effect of the misalignment. The difference between $I(x)$ and I_{empty} is equal to zero for X-ray that traveled only through the column wall or did not travel through the column, which is visible as horizontal data point for low values of x. The two distinct graph shapes are the result of the non-symmetry shown in Fig. 45

The hypothesis that the column was dislocated between the different experiments was rejected by

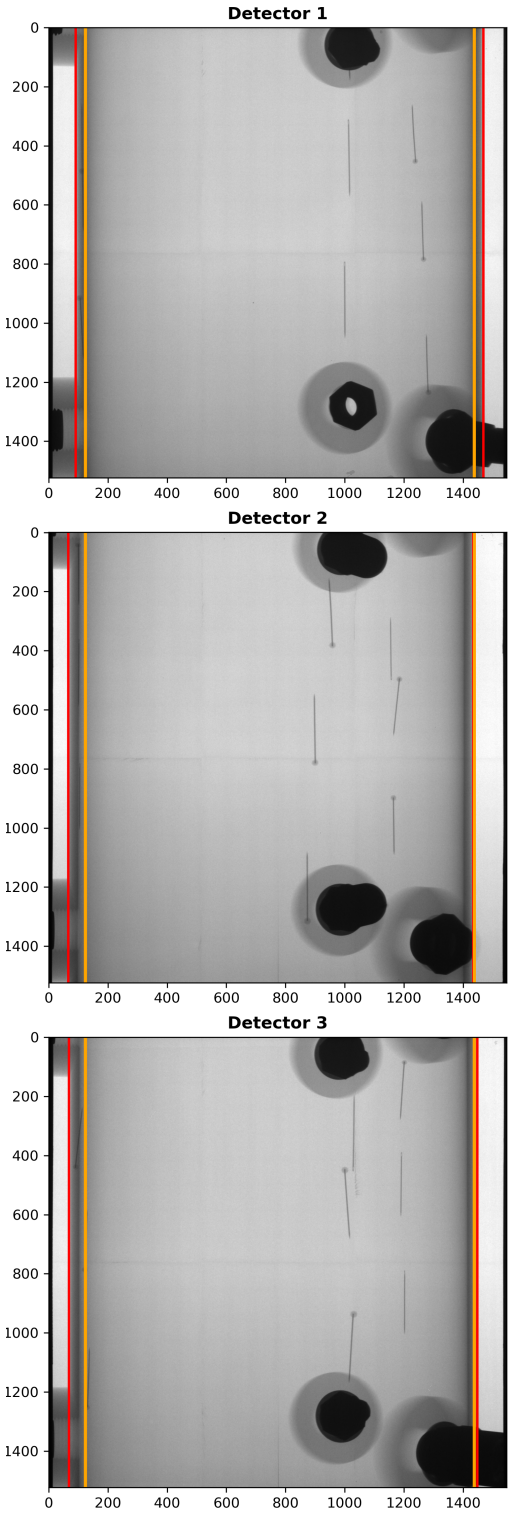

Figure 45: *A comparison between the measured column walls (red) and the calculated walls (orange).*

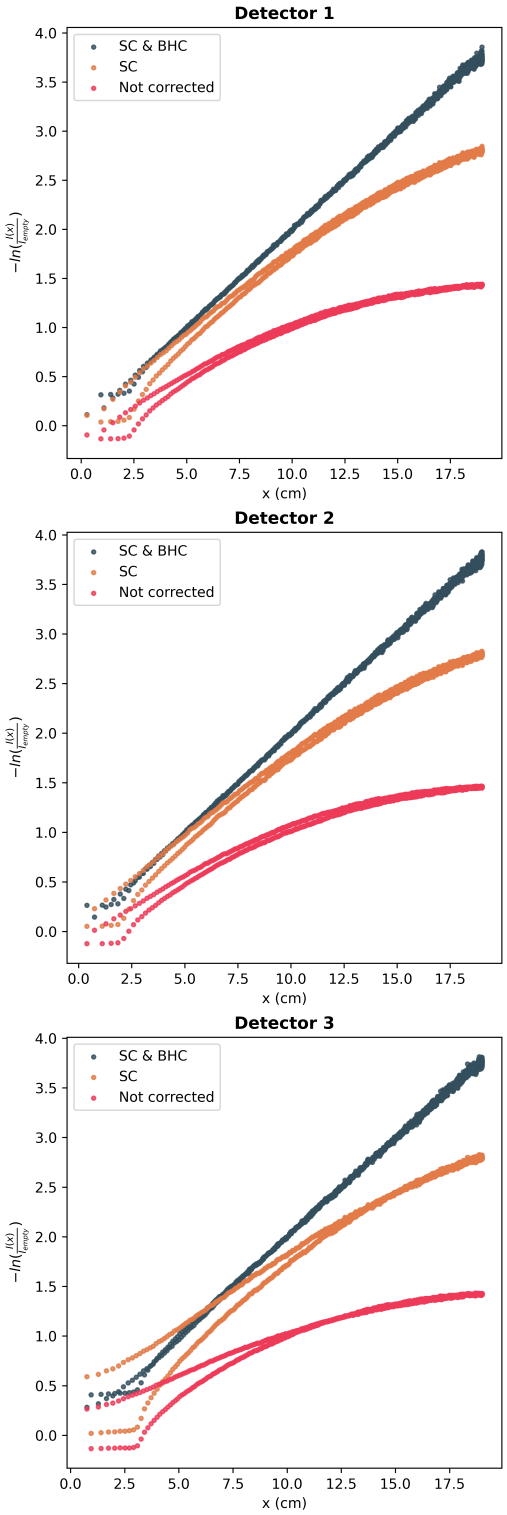

Figure 46: *Effect of misalignment of calculated and measured column walls for all 3 detectors.*

checking the position of the column walls for all the experiments. Fig. 47 and Fig. 48 show a comparison of the location of the detected walls with the calculated walls. The comparison is done for the left and right side of the detector.

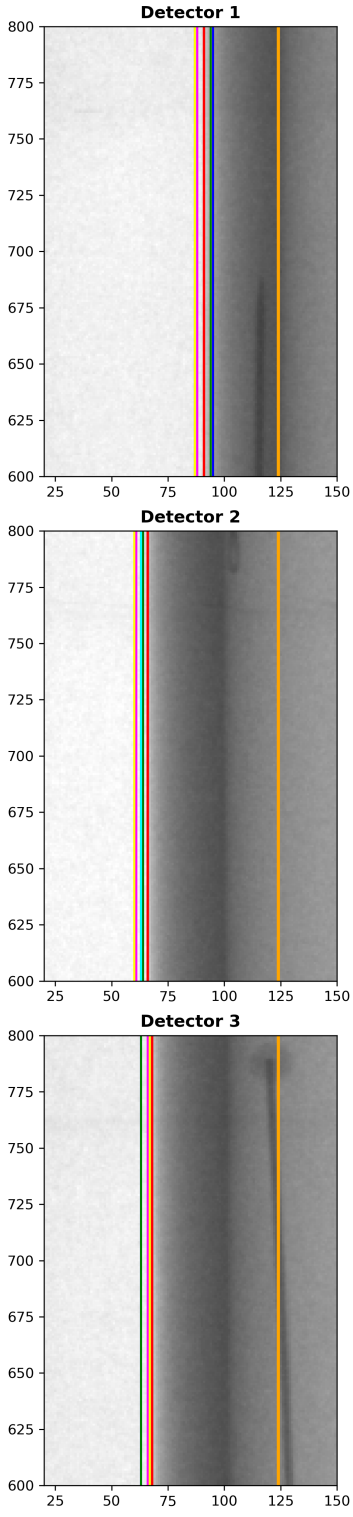

Figure 47: *Comparison of left outer wall detected in the 2D-projections and the outer wall calculated based on the geomtery from the calibration. The multiple colors on the left show the different column walls detected for the different experiments. The orange thicker line shows the calculated wall.*

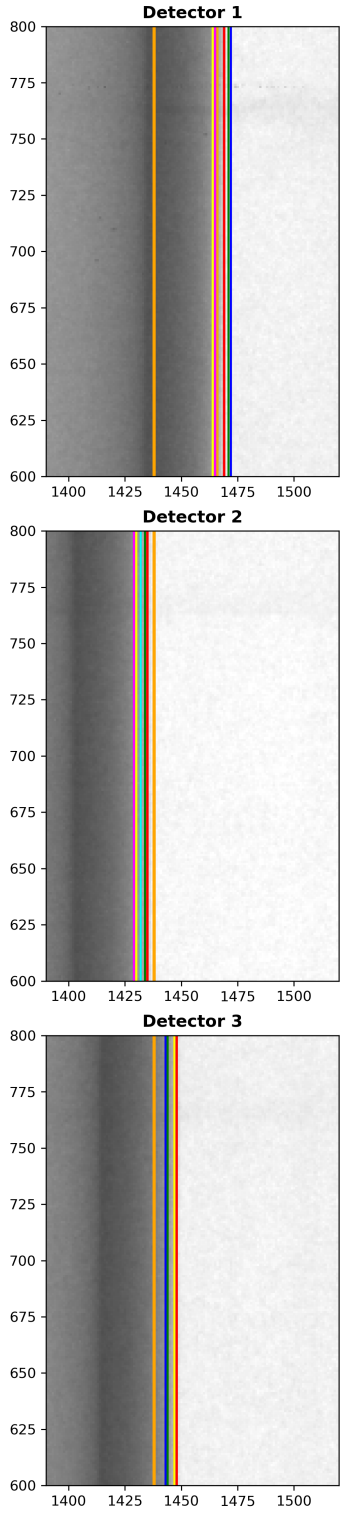

Figure 48: *Comparison of right outer wall detected in the 2D-projections and the outer wall calculated based on the geomtery from the calibration. The multiple colors on the right show the different column walls detected for the different experiments. The orange thicker line shows the calculated wall.*